

MTK 21.

**TUDOMÁNYOS BIZOTTSÁG/LEKTOROK
SCIENTIFIC ADVISORY BOARD/PEER REVIEWERS**

Bagyinszki Gyula (Budapest)
Bitay Enikő (Kolozsvár/Marosvásárhely)
Csavdári Alexandra (Kolozsvár)
Csáky Imre (Debrecen)
Czigány Tibor (Budapest)
Dávid László (Marosvásárhely)
Dezső Gergely (Nyíregyháza)
Diószegi Attila (Jönköping, Sweden)
Dobránszky János (Budapest)
Domokos József (Marosvásárhely)
Dulf Éva Henriett (Kolozsvár)
Dusza János (Kassa)
Egyed-Faluvégi Erzsébet (Marosvásárhely)
Erdei Timotei István (Debrecen)
Forgó Zoltán (Marosvásárhely)
Gobesz Ferdinánd-Zsongor (Kolozsvár)
Horváth Richárd (Budapest)
Kovács Tünde Anna (Budapest)
Máder Patrik Márk (Pécs)
Máté Márton (Marosvásárhely)
Pokorádi László (Budapest)
Popa-Müller Izolda (Marosvásárhely)
Réger Mihály (Budapest)
Réti Tamás (Budapest)
Roósz András (Budapest)
Sikolya László (Nyíregyháza)
Talpas János (Kolozsvár)
Tolvaly-Rosca Ferenc (Marosvásárhely)
Tóth László (Budapest)

ISSN 2393 – 1280

MŰSZAKI TUDOMÁNYOS KÖZLEMÉNYEK

21.

**Szerkesztette / Edited by
BITAY ENIKŐ – MÁTÉ MÁRTON**



**ERDÉLYI MÚZEUM-EGYESÜLET
Kolozsvár
2024**

A kötet megjelenését támogatta a Magyar Tudományos Akadémia,
a Bethlen Gábor Alapkezelő Zrt., és az EME Műszaki Tudományok Szakosztálya.

The publication of this volume was supported by the Hungarian Academy of Sciences,
by the Bethlen Gábor Fund, and by the TMS – Department of Engineering Sciences,



Copyright © a szerzők/the authors, EME/TMS 2024

*Minden jog a kiadvány kivonatos utánnomására, kivonatos vagy teljes másolására
(fotokópia, mikrokópia) és fordítására fenntartva.*

*All rights reserved. No part of this publication may be reproduced or transmitted in
any means, electronic, mechanical, photocopying, recording or otherwise, without the
prior written permission of the publisher.*

Kiadó/Publisher: Erdélyi Múzeum-Egyesület

Felelős kiadó/Responsible Publisher: Biró Annamária

Szerkesztette/Edited by: Bitay Enikő, Máté Márton

Olvasószerkesztő/Proofreader: András Zselyke (magyar), David Speight (English)

Műszaki szerkesztő/DTP: Szilágyi Júlia

Borítóterv/Cover: Könczey Elemér

Nyomdai munkálatok/Printing-work

F&F International Kft. Kiadó és Nyomda, Gyergyószentmiklós

Ügyvezető igazgató/Manager: Ambrus Enikő

Tel./Fax: +40-266-364171

Online elérhető/Online available at:

Magyar/Hungarian

Angol/English

<https://eme.ro/publication-hu/mtk/mtk-main.htm>

<https://eme.ro/publication/mtk/mtk-main.htm>

DOI: 10.33895/mtk-2024.21

DOI: 10.33894/mtk-2024.21

TARTALOM

Aichaoui Nada El Yasmine, Kovács Tünde Anna <i>Hegesztő robotrendszerek optimalizálási és adaptív vezérlési stratégiái</i>	1
Csavidári Alexandra Ana, Bogyor Andrea, Bitay Enikő <i>A összaskorbinsav-tartalom és az antioxidáns-aktivitás költséghatékony meghatározása. Élelmiszer-kémiai esettanulmány</i>	7
Dezső Gergely <i>Robotika-tehetség gondozás a Nyíregyházi Egyetemen</i>	16
Diós Szabolcs Sándor, Masuk Abdullah, Dinya Tamás, Szántó Attila, Pettendi Dávid, Balajti István <i>MPA-antennaforogató rendszer kiépítése interferometrikus in situ mérésekhez</i>	21
Gáti József, Némethy Krisztina, Kuti János <i>Szárasztó-berendezés száz éve</i>	31
Imecs Mária, Ferencz János, Kelemen András <i>Vektoriálisan szabályozott PMSzM-hajtás szimulálása egyszerűsített modellezési struktúrákkal</i>	36
Máté Márton, Szőcs Krisztina <i>Az evolvens fogaskerékpár csúszásának egzakt modellezése</i>	48
Ahmad Buhairi Minhalina Binti, Pinke Péter, Tóth László, Kovács Tünde Anna <i>Titánötvözetek hőkezelése</i>	56
Nagy Balázs Ákos, Gáti József, Kovács Tünde Anna <i>A kézi lézeres hegesztés biztonsági kérdései</i>	61
Nagy Örs, Sánduly Annabella, Gobesz F.-Zsongor <i>Beroppanási tönkremenetel numerikus modllezése realizztikus szélső támasznál</i>	67
Németh Báborka <i>Légsebesség mérése a műszaki kar irodáiban</i>	73
Portik Szilveszter, Gergely Attila <i>Műanyag fogaskerek koptatására alkalmas berendezés</i>	80

Rappert Balázs, Egyed-Faluvégi Erzsébet

Malomcsiszolós módszer hatékonyságának vizsgálata öntött fém alkatrészek esetén 84

Rezes Gábor, Szigeti Ferenc, Dezső Gergely

Liftajtó-fóliázó berendezés tervezése 89

Vásárhelyi József, Batók Roland, Drótos Dániel

Beágyazott rendszerek adaptív alkalmazásának vizsgálata 97

SZERZŐK JEGYZÉKE 107

CONTENT

AICHAOUI Nada El Yasmine, Tünde Anna KOVÁCS <i>Optimisation and Adaptive Control Strategies for Welding Robot Systems</i>	1
Alexandra Ana CSAVDÁRI, Andrea BOGYOR, Enikő BITAY <i>Cost-Effective Determination of Total Ascorbic Acid Content and Antioxidant Activity. A Food Chemistry Case Study</i>	7
Gergely DEZSŐ <i>Robotics Talent Management at University of Nyíregyháza</i>	16
Szabolcs Sándor DIÓS, Abdullah MASUK, Tamás DINYA, Attila SZÁNTÓ, Dávid PETTENDI, István BALAJTI <i>Construction of MPA Antenna Rotation System for Interfero-Metric “In-Situ” Measurements</i>	21
József GÁTI, Krisztina NÉMETHY, János KUTI <i>One Hundred Years of Dry Fire Extinguisher Equipment</i>	31
Mária IMECS, János FERENCZ, András KELEMEN <i>Simulation of the Vector Controlled Pmsym Drive Based on Simplified Modeling Structures</i>	36
Márton MÁTÉ, Krisztina SZŐCS <i>Non Approximative Modelling of Involute Gear Pair Sliding</i>	48
Binti Ahmad Buhairi MINHALINA, Péter PINKE, László TÓTH, Tünde Anna KOVÁCS <i>Heat-Treating Processes of the Titanium Alloys</i>	56
Balázs Ákos NAGY, József GÁTI, Tünde Anna KOVÁCS <i>Safety Questions Concerning Manual Laser Welding</i>	61
Örs NAGY, Annabella SÁNDULY, F.-Zsongor GOBESZ <i>Numerical Modelling of Web Crippling Under Realistic End Support Conditions</i>	67
Bíborka NÉMETH <i>Air Velocity Measurements in the Offices of the Faculty of Engineering</i>	73
Szilveszter PORTIK, Attila GERGELY <i>A Wear Device for Plastic Gears</i>	80

Balázs RAPPERT, Erzsébet EGYED-FALUVÉGI <i>An Examination of the Effectiveness of Tumbling on Sand-Cast Parts</i>	84
Gábor REZES, Ferenc SZIGETI, Gergely DEZSŐ <i>Design of Elevator Door Foiling Machine</i>	89
József VÁSÁRHELYI, Roland BATÓK, Dániel DRÓTOS <i>Examination of Embedded System Adaptive Configurability</i>	97
LIST OF AUTHORS	107



OPTIMISATION AND ADAPTIVE CONTROL STRATEGIES FOR WELDING ROBOT SYSTEMS

Aichaoui Nada El Yasmine,¹ Tünde Anna Kovács²

¹ Obuda University, Doctoral School on Safety and Security Sciences, Budapest, Hungary, jasminnada77@gmail.com

² Obuda University, Banki Donat Faculty of Mechanical and Safety Engineering, Hungary, kovacs.tunde@bgk.uni-obuda.hu

Abstract

This paper delves into the evolving landscape of welding robotics, particularly the integration of adaptive control strategies for optimising human-robot interaction. Collaborative robotics (cobotics) underscores the significance of adaptive control for secure effective and safe cooperation between humans and robots in welding tasks. Past research highlights optimisation techniques such as model-based optimization and genetic algorithms, alongside adaptive control strategies that dynamically adjust parameters based on real-time feedback. These advancements promise enhanced safety, efficiency, and competitiveness in industrial welding automation.

Keywords: *welding robotics, adaptive control, human-robot interaction, optimization techniques.*

1. Introduction

Robotics is a relatively nascent discipline compared to its counterparts in the scientific realm. At its core, a robot encompasses an amalgamation of technologies such as motors, sensors, and computing systems. The inception of robotics occurred when these individual technologies reached a level of maturity that could be integrated harmoniously. A distinguishing aspect of robotics lies in its dependence on technological advancements to conceive and explore novel applications. This inherent reliance injects an element of excitement into the field, as it continually evolves in tandem with technological progress [1]. Undoubtedly, robotics has achieved a level of maturity for specific tasks within various environments, a facet that the industry extensively leverages to bolster productivity.

One of the foremost challenges confronting robotics lies in scenarios where robots interact physically with humans, a realm ripe with promise. While robots are commonly employed in industrial settings, their utilization often involves isolating them within cells to ensure the safety of human workers. Nonetheless, numerous tasks remain ripe for automation, necessitating human

operators who possess the adaptability to navigate complex situations that robots may not fully address [1]. As a response to this, cobotics, which facilitates collaboration between humans and robotic counterparts, has emerged. Despite its considerable potential, cobotics is still in its infancy, with safety concerns surrounding human-robot interactions at the forefront [2].

Interestingly, the foundational issue inherent in such human-robot interaction predates the inception of robotics itself and stems from the realm of cybernetics. Originating during World War II, cybernetics sought to devise systems capable of predicting and accommodating human responses to robotic actions. Notably, Norbert Wiener pioneered this field with the creation of an automatic pilot system named the "predictor," designed to anticipate a pilot's evasion trajectory against anti-aircraft projectiles. Wiener's seminal work, "Cybernetics or Control and Communication in Animals and the Machine," laid the groundwork for this research domain by presenting a theory of control and communication applicable to both biological organisms and machines [3]. It is within this framework that research on robotics in interaction with humans finds its roots.

Overall, Industrial robots are distinguished from more traditional production and assembly equipment in particular by their ability to carry out many different tasks. To carry out these various tasks, the industrial robot must often make configuration or tool changes or even make movements while taking into account its current state and the history of the production parts. This is all the more true in a dynamic scheduling environment with the possible need to change a decision or interrupt current tasks. A realistic and precise scheduling model should take into account these state change operations and the specificities of the different tasks carried out (duration, occupied capacity, etc.) [4].

Moving to one of the ultimate robotics fields, the welding robot has control systems that reflect a significant evolution toward advanced automation and precision. Traditional control systems relied heavily on predefined trajectories and fixed parameters, limiting their adaptability to variations in welding conditions and workpiece geometries. However, recent advancements have revolutionized this landscape. Modern welding robot control systems incorporate sophisticated sensor technologies such as vision systems, laser scanners, and force/torque sensors, enabling real-time feedback and adaptive control. These systems utilize advanced algorithms, including machine learning and artificial intelligence, to optimize welding parameters and trajectories dynamically. Furthermore, collaborative robots (cobots) with advanced safety features have emerged as a prominent trend, allowing for human-robot collaboration in welding tasks [5]. Integration with cloud computing and data analytics facilitates remote monitoring, predictive maintenance, and continuous improvement of welding processes. Overall, the current state-of-the-art of welding robot control systems emphasizes flexibility, efficiency, and quality, paving the way for increased productivity and competitiveness in industries reliant on welding technology [6].

Traditional control methods in welding robot systems face several challenges that hinder their effectiveness in meeting the demands of modern manufacturing environments [5]. One significant challenge is their limited adaptability to variations in welding conditions, such as changes in material properties, joint geometries, or environmental factors like temperature and humidity. Traditional controllers often rely on predefined trajectories and fixed parameters, making them

ill-equipped to handle dynamic situations encountered in real-world welding applications. This rigidity can lead to issues such as poor weld quality, inconsistent bead profiles, and increased rework or scrap rates. Moreover, traditional controllers cannot respond in real time to disturbances or anomalies during the welding process, resulting in reduced productivity and efficiency. Additionally, these control methods may struggle to optimize welding parameters for different materials or welding techniques, leading to sub-optimal performance and increased operational costs. In summary, the challenges faced by traditional control methods highlight the need for more adaptive, intelligent, and flexible approaches to welding robot control to address the complexities of modern manufacturing requirements effectively [7].

1.1. State of the art

Past studies and research that focus on optimization and adaptive control within the welding domain have achieved notable progress in enhancing the performance, efficiency, and overall quality of welding operations. Extensive investigations have been conducted into optimization methodologies, targeting diverse facets of welding processes ranging from trajectory planning and parameter adjustment to resource distribution. Utilizing mathematical optimization frameworks such as genetic algorithms, particle swarm optimization, and simulated annealing, researchers have endeavoured to fine-tune welding parameters such as voltage, current, travel speed, and wire feed rate [8]. The primary objective of these optimization endeavours is to mitigate common welding defects including porosity, undercutting, and spatter, while simultaneously maximizing productivity and weld integrity [9].

Adaptive control strategies have also been a focus of research, aiming to dynamically adjust control parameters based on real-time feedback from sensors and environmental conditions [8]. Adaptive control techniques, such as model predictive control, fuzzy logic control, and neural networks, enable welding robots to adapt to changes in workpiece geometry, material properties, and welding conditions. By continuously monitoring key process variables, such as arc voltage, welding current, and torch orientation, adaptive control systems can compensate for disturbances, optimize weld bead geometry, and improve overall process stability and robustness [9].

Furthermore, research efforts have explored the integration of advanced sensing technologies, such as vision systems, laser scanners, and thermal imaging cameras, to provide comprehensive feedback for adaptive control algorithms. These sensing technologies enable welding robots to accurately detect joint misalignments, seam tracking errors, and surface irregularities, facilitating precise control and correction during the welding process [5]. Overall, previous research on optimization and adaptive control in welding has demonstrated the potential to significantly enhance the performance and efficiency of welding processes, paving the way for the development of more advanced and intelligent welding robot systems capable of meeting the demands of modern manufacturing industries [8].

The focus of this research is on the development of intelligent control techniques for welding automation. The research scope encompasses the investigation of how to control the welding path and the weld pool geometry in real time. The objectives of the research are classified into three categories: problem formulation, optimization, and adaptive control. First, a physical process and mathematical model will be investigated and developed to describe the dynamic behavior of the welding process. Then a series of optimization and adaptive control techniques will be studied and developed to effectively and efficiently control the welding process. Once the intelligent control strategies are developed, an experimental validation will be conducted to verify the correctness and effectiveness of the proposed control techniques. It is expected that the outcome of this research will provide a systematic procedure for the development of adaptive control and optimization. This could be utilized in a wide range of welding automation tasks such as developing intelligent control schemes for welding robots, developing a real-time monitoring and control system for the automated welding process, and providing state-of-the-art training facilities in the welding field, etc. Moreover, the scientific findings resulting from this research would also enhance the basic understanding and technical capabilities in the areas of control and automation. More importantly, it would lay the groundwork for promoting various ongoing and future interdisciplinary research activities relating to both education and industrial consultancies, such as the in-company training programs for the local industry on modern welding strategies and automation, the automation of other welding proce-

dures, e.g. TIG and laser welding, and the development of customized research-oriented equipment for related academic and industrial use.

1.2. Background on Optimization Technics in Welding

1.2.1. Model-based optimization

Model-based optimization in welding involves using mathematical models to simulate and refine welding processes, incorporating equations that represent the physical phenomena present during welding, such as heat transfer, fluid flow, and metallurgical changes. These computational models are created to emulate welding behaviour under different conditions, forecasting results for various parameter combinations to pinpoint optimal configurations for desired weld attributes. This method fosters a systematic comprehension of the complex interplay between welding parameters and their impact on weld quality, enabling thorough exploration of different process variables and scenarios without extensive experimentation. Nonetheless, challenges emerge in crafting accurate and computationally efficient models, necessitating a profound understanding of welding physics and intricate numerical algorithms. Furthermore, disparities between simulation outcomes and real-world results may arise due to the inability to fully encapsulate the intricacies of actual welding processes [10].

The primary distinction between model-based and other forms of machine learning lies in the learning process's reliance on interactions between the agent and its environment. Consequently, the agent acquires task-specific knowledge directly from the environment without external instruction. However, delineating between the agent and the environment is not always straightforward and is contingent on the application [11]. For instance, in tasks like bipedal walking and UAV control, the environment is presumed to encompass the robot's motors.

In model-based methods, a model of transition dynamics is employed to derive rewards and optimal actions, with policies optimized within the model and subsequently applied to the physical system. Fig. 1 illustrates the model-based reinforcement learning pipeline.

1.2.2. Genetic Algorithms (GAs)

GAs represent an optimization technique inspired by natural selection and evolution, where a population of potential solutions evolves

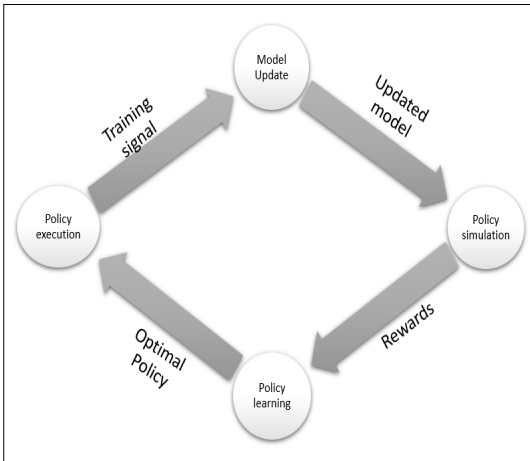


Fig. 1. Model-based reinforcement learning pipeline.

through successive generations via processes like selection, crossover, and mutation, with the fittest individuals selected for further reproduction. In welding, GAs are employed to optimize welding parameters by encoding them as chromosomes within a population. Through iterative generations, the algorithm evaluates the fitness of each solution, based on predefined objective functions such as weld quality metrics, selecting the best-performing individuals for subsequent generations. GAs offer a robust approach capable of handling complex, nonlinear optimization problems with multiple objectives and constraints, efficiently exploring large solution spaces and identifying near-optimal solutions in relatively short timeframes. However, effective utilization of GAs demands careful parameter tuning and selection of appropriate genetic operators to ensure convergence to meaningful solutions, while computational complexity may become prohibitive for highly dimensional optimization problems or computationally intensive welding models [12].

1.2.3. Particle Swarm Optimization (PSO)

The concept of PSO is derived from the collective behaviour observed in organisms like birds flocking or fish schooling, serving as a population-based stochastic optimization technique. In PSO, a group of potential solutions, depicted as particles, continually adjust their positions within the search space based on both individual experiences and shared knowledge within the swarm. Each particle embodies a potential solution encompassing a set of welding parameters, and its movement is guided by its personal best-known

position as well as the collective best-known position uncovered by the swarm. Through this iterative process, the swarm progressively converges towards promising areas within the solution space, rendering PSO particularly advantageous for tasks characterized by continuous solution spaces and smooth objective functions. Despite its relative ease of implementation and computational efficiency, PSO's effectiveness may be influenced by the careful selection of control parameters, and it may encounter difficulties escaping local optima in intricate, multimodal optimization scenarios [13].

1.3. Adaptive control in Welding

Adaptive control strategies in welding represent a dynamic approach to optimizing welding processes by continuously adjusting control parameters in response to real-time feedback from sensors and environmental conditions. These strategies are designed to enable welding robots to adapt swiftly to changes in workpiece geometry, material properties, and other factors affecting the welding process, thereby enhancing overall process stability and robustness. Through the constant monitoring of critical process variables such as arc voltage, welding current, and torch orientation, adaptive control systems can effectively compensate for disturbances and variations encountered during welding operations [9]. This adaptability ensures that the welding parameters remain optimized for the specific conditions at hand, leading to improved weld quality and productivity. Furthermore, the integration of machine learning methods and advanced sensing technologies like vision systems and thermal imaging cameras further enhances the adaptability and precision of adaptive control systems by providing comprehensive feedback on the welding environment. Overall, adaptive control strategies represent a crucial advancement in welding technology, offering the potential to achieve consistently high-quality welds while maximizing efficiency and minimizing defects in diverse operating conditions [8].

Moreover, it is pivotal in optimizing the interaction between humans and welding robots, particularly in collaborative robotics or cobotics scenarios. In such setups, where humans and robots work together in shared spaces, adaptive control strategies are essential for ensuring safe and efficient collaboration. These strategies involve dynamically adjusting the robot's behaviour based on real-time feedback from sensors monitoring

the human operator's movements, intentions, and safety. For instance, adaptive control systems can modulate the robot's speed, trajectory, and force exertion to prevent collisions or accidents, thus ensuring the safety of the human operator. Moreover, adaptive control allows the robot to adapt its behaviour to accommodate variations in the human operator's actions, preferences, and capabilities, enhancing the overall collaboration experience [8]. By continuously monitoring and analyzing the interaction between the human and welding robot, adaptive control systems can optimize task execution, minimize errors, and maximize productivity. Additionally, adaptive control enables seamless switching between autonomous robot operation and collaborative modes, providing flexibility and versatility in various welding applications [9]. Overall, the use of adaptive control in optimizing human-robot interaction in welding environments not only enhances safety and efficiency but also fosters a more intuitive and harmonious working relationship between humans and robots. Fig. 2 illustrates the steps of controlling the welding robot to ensure not only human safety but also the quality of the production.

2. Conclusions

The current state of welding technology lacks extensive integration of advanced algorithms for optimizing parameters and identifying defects, which is evident from limited accessible information. However, recent advancements have shown promising progress in utilizing neural networks to automate these processes, albeit in their early stages [5].

The application of machine learning in welding shows significant potential for progress, though further research and development are needed before implementation in industrial settings. In-

tegrating machine learning into welding systems presents a valuable opportunity for advancement, offering improved parameter optimization and defect detection with greater precision and efficiency through the use of neural networks and other sophisticated algorithms. This automation potential could enhance productivity, and weld quality, and reduce reliance on manual adjustments and human inspection. Nevertheless, incorporating advanced algorithms into industrial welding will require considerable time and resources, with challenges such as data availability, algorithm robustness, and computational requirements needing to be addressed for reliable implementation.

Looking ahead, the future of intelligent welding systems depends on the continued exploration and advancement of machine-learning approaches. With further research, more tailored algorithms specifically designed for welding processes can be developed, enabling not only automated parameter optimization and defect detection but also real-time decision-making, adaptive control, and seamless integration into existing welding infrastructure.

References

- [1] Bibby L., Dehe B.: *Defining and Assessing Industry 4.0 Maturity Levels-Case of the Defence Sector*. Production Planning & Control, 29/12. (2018) 1030–1043.
- [2] Barcellini F., Béarée R., Benchekroun T. H., Bounouar M., Buchmann W., Dubey G., Siadat A.: *Promises of Industry 4.0 under the Magnifying Glass of Interdisciplinarity: Revealing Operators and Managers Work and Challenging Collaborative Robot Design*. Cognition, Technology & Work, (2023) 1–21.
- [3] Wiener N.: *Cybernetics or Control and Communication in the Animal and the Machine*. MIT Press. (2019).

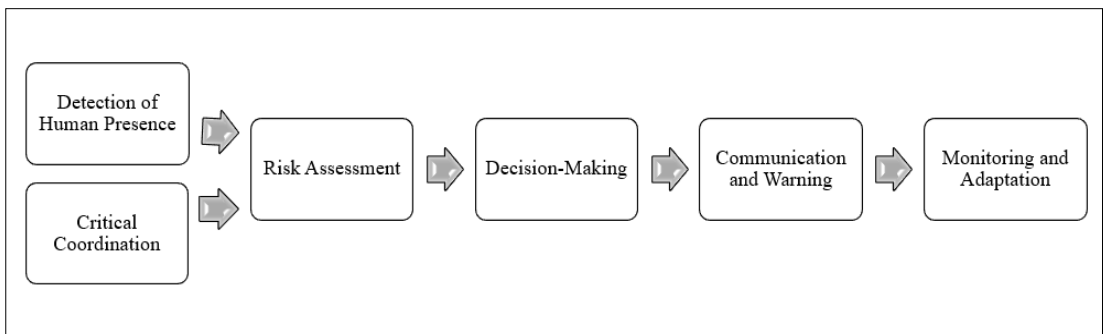


Fig. 2. Safety and quality maintaining steps in welding robot controlling.

- [4] Hajji A., Pellerin R.: *Ordonnancement dynamique et contrôle intelligent d'un robot industriel*, (2023).
- [5] Wang B., Hu S. J., Sun L., Freiheit T.: *Intelligent Welding System Technologies: State-of-the-Art Review and Perspectives*. Journal of Manufacturing Systems, 56. (2020) 373–391.
- [6] Rout A., Deepak B. B. V. L., Biswal B. B.: *Advances in Weld Seam Tracking Techniques for Robotic Welding: A Review*. Robotics and Computer-Integrated Manufacturing, 56. (2019) 12–37.
- [7] Pires J. N., Loureiro A., Böllmsjo G.: *Welding Robots: Technology, System Issues and Application*. Springer Science & Business Media (2006).
- [8] Doumanidis C. C., Hardt D. E.: *Multivariable Adaptive Control of Thermal Properties during Welding* (1991).
- [9] Aldalur E., Suárez A., Curiel D., Veiga F., Villanueva P.: *Intelligent and Adaptive System for Welding Process Automation in T-Shaped Joints*. Metals, 13/9. (2023) 1532.
- [10] Chen F. F., Xiang J., Thomas D. G., Murphy A. B.: *Model-Based Parameter Optimization for Arc Welding Process Simulation*. Applied Mathematical Modelling, 81. (2020) 386–400.
- [11] Tabar R. S., Wärmefjord K., Söderberg R.: *A New Surrogate Model-Based Method for Individualized Spot Welding Sequence Optimization Concerning Geometrical Quality*. The International Journal of Advanced Manufacturing Technology, 106. (2020) 2333–2346.
- [12] Nagesh D. S., Datta G. L.: *Genetic Algorithm for Optimization of Welding Variables for Height to Width Ratio and Application of ANN for Prediction of Bead Geometry for TIG Welding Process*. Applied Soft Computing, 10/3. (2010) 897–907.
- [13] Tafarroj M. M., Moghaddam M. A., Dalir H., Kollahan F.: *Using Hybrid Artificial Neural Network and Particle Swarm Optimization Algorithm for Modeling and Optimization of Welding Process*. Journal of Advanced Manufacturing Systems, 20/04. (2021) 783–799.



COST-EFFECTIVE DETERMINATION OF TOTAL ASCORBIC ACID CONTENT AND ANTIOXIDANT ACTIVITY. A FOOD CHEMISTRY CASE STUDY

Alexandra Ana CSAVDÁRI,^{1,2} Andrea BOGYOR,^{1,2} Enikő BITAY^{3,4}

¹ Babes-Bolyai University, Faculty of Chemistry and Chemical Engineering, Cluj-Napoca, Romania, alexandra.csavdari@ubbcluj.ro

² EME Transylvanian Museum Society, Cluj-Napoca, Romania

³ Sapientia Hungarian University of Transylvania, Faculty of Technical and Human Sciences, Târgu-Mureş, Romania

⁴ Óbuda University, Bánki Donát Faculty of Mechanical and Safety Engineering, Budapest, Hungary

Abstract

This study investigates the cost-effective and reliable determination of total ascorbic acid (AA) content, as well as antioxidant activity, from a range of 32 alcoholic and non-alcoholic beverages. 5 cold-pressed oil samples and 2 types of honey were also considered. Among the iodometric methods, the back-titration of unreacted iodine with thiosulfate yielded the best results for AA content. The method proved simple, fast, reliable, and accurate, with a recovery rate of ascorbic acid exceeding 99% in 2 standardized commercial pharmaceutical products. Total antioxidant activity determination was based on the reaction of antioxidant species with ABTS, followed by a photometric assessment of the reaction's extent. Results, expressed in terms of AA content, were good and reliable, yet in some cases less precise and accurate. Most beverages exhibited higher antioxidant activity than their respective AA content, likely influenced by other antioxidant compounds such as flavonoids and anthocyanins present in fruit-based drinks. Both methods proved useful in demonstrating the nutritional value of various easy to consume beverages, oils and honey.

Keywords: *total ascorbic acid content, antioxidant activity, food samples, iodometry, photometry.*

1. Introduction

1.1. The importance of vitamin C for the human body

Vitamin C (L-ascorbic acid) is an essential nutrient for the human body. Its importance was first recognized by the Hungarian scientist Albert Szent-Györgyi. Widely known under the generic name of ascorbic acid (AA), it has been the subject of continuous research due to its key role for the healthy physiological functioning of the human body [1, 2].

Vitamin C is crucial for the immune system (in-nate or adaptive), preventing and treating many respiratory and systemic infections [3]. It helps maintain blood pressure levels and has been linked to the prevention of cancer and cardiovascular diseases [1, 4]. It also has a positive effect

on diabetes, common cold, stroke and anaemia recovery [5]. Recent research has revealed its role in the regulation of gene transcription and cell signalling pathways [3].

The human body is not able to produce the minimum necessary daily amounts of 110 mg for men and 78 mg vitamin C for women [1]. Thus, its intake must be ensured by means of external sources, such as suitable food or dietary supplements. Otherwise, its lack can lead to scurvy or other serious, even fatal diseases [3]. Vitamin C deficiency is a common problem in certain areas of the world, especially in low- and middle-income countries, but it is not uncommon among high-income regions either [6]. Since the absorption of vitamin C in the digestive system is of about 80% from a daily intake of 100 mg, a vitamin C rich diet is of utmost importance, even though the

human body cannot absorb/store more than 2.5g (due to its partial oxidation to two metabolites: the active dehydroascorbic acid and the inactive oxalic acid) [4, 7].

The main natural sources of vitamin C are fruits (such as berries, papaya, kiwi, citrus fruits, peaches, apples or pears), vegetables (such as Brussels sprouts, cauliflower, cabbage or sweet pepper), some herbs (such as parsley or sorrel), and their respective juices. All can be incorporated into a rapid paced lifestyle [1, 4].

Some environmental factors, such as exposure to air, light or heat, improper storage conditions or various food processing procedures, may reduce the AA content of these products [5, 8]. Therefore, the market nowadays offers numerous vitamin C enriched fruit drinks and/or supplements [9, 10]. Ascorbic acid is identified in food chemistry as additive E300, being also often used either as a preservative and/or an antioxidant.

Hence, correct information about the nutrient and bioactive content of these ascorbic acid sources is essential in understanding their health benefits. As a result, there is abundant scientific literature providing detailed information about the methods to detect and assess the total AA content of both natural and synthetic Vitamin C sources.

1.2. Methods of ascorbic acid determination

The structural chemical formula of Vitamin C - the biologically active L-enantiomer of ascorbic acid - is presented in Figure 1. Its content in various samples is usually expressed as total ascorbic acid concentration. The latter corresponds to the racemic mixture of L and D enantiomers.

Numerous methods have been put forward for the quantitative determination of total AA content. A classical and inexpensive approach is based on titration with oxidizing solutions. Other techniques involve color reactions (for example with 2,6-dichlorophenol-indophenol), UV-VIS spectrophotometry, high performance liquid chromatography, capillary electrophoresis, chemiluminescence, fluorimetry, amperometry and various enzymatic methods, all of which present their respective advantages and disadvantages [1, 11, 12, 13].

Titrimetric methods are advantageous when analyzing a large number of samples, due to their simplicity, cost-effectiveness and speed. However, in the case of colored samples, end-point detection may be difficult. High-performance liquid chromatography is the most accurate method for

the quantification of ascorbic acid, but it requires highly qualified laboratory expertise and expensive equipment. Electrophoresis and chemiluminescence are relatively cheaper alternatives, but their sensitivity is lower. Fluorimetry and voltammetry provide fast results, yet require special instrumentation and precise calibration [1, 14].

Among all the listed procedures, the simplest and most cost-effective is titration. It is also both precise and accurate, since it generates results which are comparable to the more sophisticated spectrophotometric and chromatographic methods. If it is carried out automatically, and/or on fresh samples, air induced oxidation of the ascorbic acid in the samples can be avoided or at least minimized [10].

The AA content is often correlated with the antioxidant capacity of a certain food sample. Since AA is a reducing agent, it can interact with all kinds of oxidizing species or free radicals [15]. In the food industry 2,2'-azino-bis(3-ethylbenzothiazoline-6-sulfonic acid (ABTS) is mostly used to assess the total antioxidant capacity of various products.

One purpose of this work was to determine the total ascorbic acid content of various beverages present in the Romanian market. These belonged to the following categories: cold-pressed and sugar preserved syrups, freshly squeezed fruit juices, carbonated soft drinks, pasteurized juices, and alcoholic beverages. Some honey and oil samples were also considered.

Another goal was to express the total antioxidant content of these products as well as correlate it with their AA concentration.

2. Experiment description

2.1. Reagents, equipment, and samples

Analytical grade purity reagents were used from commercial sources (Merck KgaA, Darmstadt, Germany). Deionized water (HydroPure 300, MultiLab, Bucharest, Romania) was used to prepare

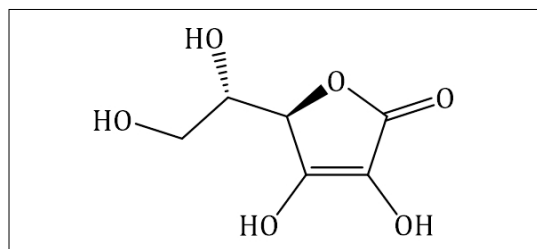


Fig. 1. The structural formula of vitamin C.

the following working solutions: 10^{-3} mol/L ABTS, 10^{-2} mol/L $\text{Na}_2\text{S}_2\text{O}_3$, 10^{-2} mol/L KI, 1.05×10^{-2} mol/L KIO_3 , 0.5 mol/L HCl, 4.73×10^{-3} mol/L I_2/KI , and 2% starch, respectively. Ascorbic acid working solutions of various concentrations, as well as the sodium thiosulfate solutions were freshly prepared before each set of experiments.

Standard laboratory glassware and utensils (Labbox, Labware, Bucharest, Romania) were used during the experiments: beakers, flasks, Schelbach line burettes, and adjustable volume micropipettes, respectively. A KERN laboratory scale (SC. Driatheli Group SRL, official partner of Kern, Győröd, Romania) and a VIS V-1100 single-channel spectrophotometer (DLAB, AMEX-lab, Bucharest, Romania) were also employed. The latter was operated by means of a dedicated software (M.Wave Professional). Photometric measurements were carried out in a glass cuvette with an optical path length of 1 cm. Statistical processing of obtained data was carried out with the dedicated tools of Microsoft Office Excel.

A total of 41 food samples were examined. These can be classified into 5 categories, as illustrated in **Figure 2**. The samples were collected from the Romanian market, from both commercial and individual producers, as follows: 9 cold-pressed fruit syrups (with added sugar for preservation), 6 pasteurized vegetable or fruit juices, 3 carbonated soft drinks, 3 freshly squeezed fruit juices, 11 alcoholic beverages, 5 cold-pressed oils, and 2 types of honey, respectively.

Two commercially available pharmaceutical products with standardized and declared ascorbic acid content were used to validate the employed methods: Aspirin Plus C (240 mg AA

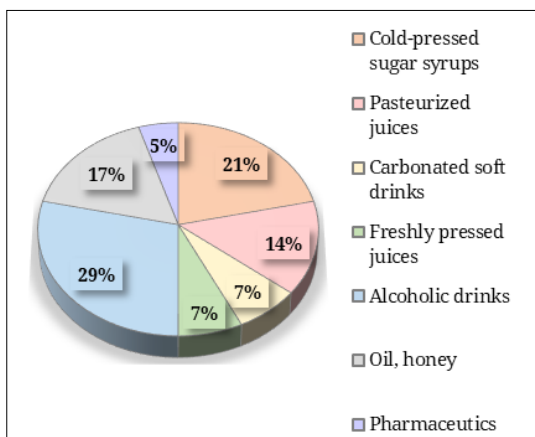


Fig. 2. Categories of tested food samples.

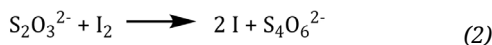
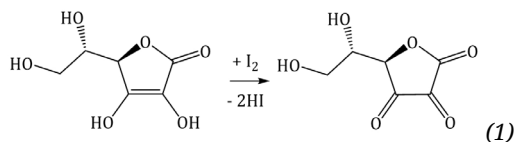
content) and Redoxon (1000 mg AA content) effervescent tablets (both manufactured by Bayer Bitterfeld GmbH, Greppin, Germany).

2.2. Experimental methods

Determination of total ascorbic acid content was carried out by means of titrimetric methods. These are based on the oxidation of ascorbic acid to dehydroascorbic acid by iodine - see reaction (1). The latter (I_2) can be added to the sample directly for „Iodometry 1”, or can be generated in situ by means of the iodide/iodate (I^-/IO_3^-) redox couple in acidic media - see reaction (3), for „Iodometry 2”.

Determination of total antioxidant capacity is based on the ability of the antioxidants in the sample to react with/ discolour the greenish-blue ABTS. The extent of this process is monitored photometrically at 735 nm.

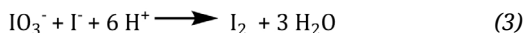
2.2.1. Titrimetric determination of total ascorbic acid content



Iodometry 1: The procedure starts with addition of excess iodine to the liquid sample. Because of the excess I_2 , the sample will preserve/exhibit the characteristic brown/ brownish color of iodine. The ascorbic acid present in the sample reduces iodine to iodide. The remaining iodine is further (back-)titrated with sodium thiosulfate in the presence of starch - see reaction (2) [14, 15]. During titration the sample will turn pale yellow, then blue-indigo when a few drops of starch are added. The end-point is reached when the sample regains its initial color, or turns colorless (in case of synthetic AA colorless solutions). The advantage of this method lies in managing to oxidize the entire ascorbic acid amount of the sample in the desired way (by iodine), not in other reaction paths (such as by the oxygen dissolved from air into the liquid sample). In addition, the method is extremely simple and cost-effective.

Iodometry 2: Another indirect titrimetric method involves in situ iodine generation. Potassium iodide (KI), hydrochloric acid (HCl) and starch are added to the liquid sample. Further, it is titrated with potassium iodate (KIO_3). This will gen-

erate iodine (I_2) according to reaction (3), which instantly reacts with the AA in the sample – see reaction (1). As long as AA is still present, the sample's color remains unchanged. The end-point is reached when all AA is consumed and I_2 starts accumulating, hence changing the color of the sample (for example from colorless to dark blue). Because iodine is generated during the advance of titration, reaction (1) may be competition with the dissolved oxygen oxidation of AA. This may affect the results [7, 14].



Liquid food (including oil) samples were analysed as such, by using aliquotes of 5 to 50 mL volume. For honey, 2g were dissolved in 10 mL of water, and the resulting aqueous solution was subjected to analysis. The pharmaceutical tablets were dissolved in water in 250 mL volumetric flasks, and the resulting solution was titrated. All titrations were performed in triplicate.

Calculus of results considered the sample and titrant volumes, as well as the concentrations of working solutions. Results were expressed in mg/L of ascorbic acid, except for honey, where they were given as mg/100g product.

2.2.2. Photometric determination of total antioxidant capacity

The 2,2'-azino-bis(3-ethylbenzothiazoline-6-sulfonic acid) (ABTS) is a highly water soluble compound [16]. It exhibits a greenish-blue color, with an absorbance maximum at 735 nm (see also Figure 8). When added to a sample, some of it will react with reducing species present in the latter ([17, 18]), hence the absorbance value (color intensity) will drop. The difference in the absorbances is correlated with the total antioxidant activity via a calibration line. In the presented case, this was obtained by means of reacting the same amount of ABTS with various amounts of AA, according to the reaction scheme presented in Figure 3.

The method required freshly prepared/ diluted ascorbic acid solutions, as well as multiple and up to 5000 fold dilution of the employed liquid food samples.

Calibration as well sample measurements were carried out in triplicate. Calculus of results considered the sample volumes, their dilution coefficients, and a calibration line of 735 nm absorbance difference versus ascorbic acid concentration. Results were given in mg/L equivalent of ascorbic acid.

3. Results and discussion

3.1. End-point detection in titrimetric methods

In both employed iodometric methods, end-point detection is based on color changes. If a colorless sample or a synthetic AA solution are used, a switch from indigo-blue to colorless is observed for „Iodometry 1”. Figure 4 illustrates the sequence of color changes during the classical titration of an aqueous iodine solution (A) with thiosulfate. First it turns yellow (B); after adding a few drops of starch, the color changes to deep blue (C); then further turns colorless (D) when titration is complete.

On the other hand, analysis of colored liquid food samples (such as fruit juices) requires for correct end-point detection a color comparison with the initial color of the sample. Figure 5. presents a similar to Figure 4 sequence, but for a red beetroot juice (B). When mixed with iodine (A) and starch it generates intense dark colors as in flasks (C) and (D). The end-point (E) of titration is reached when the initial juice's color (B) is obtained.

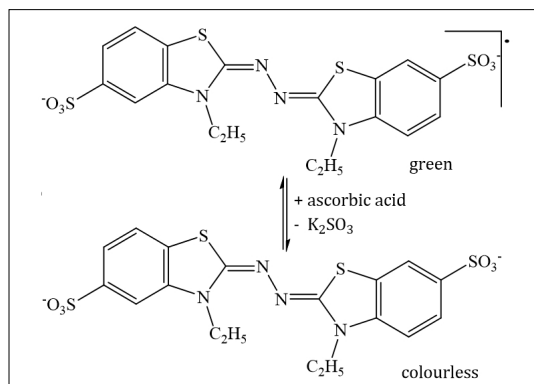


Fig. 3. The reaction scheme between the ABTS radical and ascorbic acid. [19]

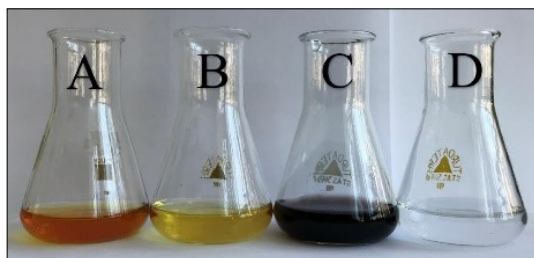


Fig. 4. End-point detection. Color change sequence for the titration of iodine with thiosulfate - „Iodometry 1”.

For „Iodometry 2”, a synthetic AA solution will turn from colorless to deep blue when the end-point of KIO_3 titration is reached. The method works well for colorless or light colored samples. Yet in the case of red, blue or intensely colored food samples, end-point detection proves to be difficult, due to almost no, or just slight, color changes.

Figure 6 illustrates the trials for the titration of a homemade red wine. It is obvious that the sample itself (left) has almost the same color as the one which was considered at titration end-point (right). Another disadvantage of this method is the fact that although these titrations are carried out in acidic media, the corresponding chemical reactions are fairly slow, and hence, color development at room temperature takes sometimes up to 8 minutes.

As a result, „Iodometry 1” has given more reliable and reproducible results. However, both approaches were tested against 2 commercial pharmaceutical products with known AA contents. The results are summarized in **Table 1**.

The small values of deviations prove that both titrimetric methods generate precise data, yet not necessarily accurate in the case of „Iodometry 2” and the Redoxon tablet (probably because of its intense orange color, thus incorrect end-point detection). The Aspirin Plus C tablet generates a colorless aqueous solution, hence end-point detection is not hindered.

On the other hand, recoveries were very good for both analysed products in case of „Iodometry 1”. Hence, the latter proves to be precise, accurate and thus was chosen for the total ascorbic acid content determination in all considered samples.

3.2. Total ascorbic acid content of analysed samples

Total ascorbic acid content was determined for all 41 food samples presented in Section 2.1, by means of „Iodometry 1” described in Section 2.2.1 **Figure 7** illustrates the results expressed as C_{AA} in mg/L. Each color corresponds to a certain class of samples.

The freshly squeezed juices (IV) have the highest ascorbic acid content, of around 500 mg/L. This is in line with literature data reporting that orange juice retains its bioactive compounds during storage. The vitamin C content of fresh orange juice is comparable with that of commercial ones, because of adequate modern industrial processing techniques [8].



Fig. 5. End-point detection. Color change sequence for the back-titration of iodine with thiosulfate in a red color beetroot juice - „Iodometry 1”.



Fig. 6. End-point detection. Illustration of the similar colors of home made red wine sample (left) and its titrated correspondent (right) - „Iodometry 2”.

Table 1. Values returned during validation of employed experimental methods.

Method	Redoxon	Aspirin Plus C
	Recovered (%)	
Iodometry 1	99.99 ± 0.73	99.43 ± 3.53
Iodometry 2	74.71 ± 0.33	99.00 ± 0.00
Photometry	113.97 ± 32.56	96.69 ± 14.11

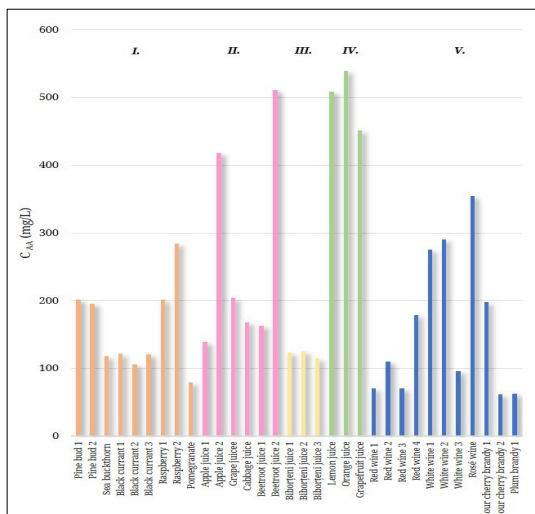


Fig. 7. Total ascorbic acid content for: I. Cold-pressed sugar preserved syrups; II. Pasteurized juices; III. Carbonated soft drinks; IV. Freshly squeezed fruit juices; V. Alcoholic beverages.

Among the cold-pressed sugar preserved syrups (class I), raspberry contains the most AA. It is followed by pine buds, blackcurrant and sea buckthorn, respectively. Within the pasteurized juice category (II), beetroot and apple juice prove best. In contrast, grape and cabbage juice show less AA content, yet still comparable with that of sample category I.

The AA present in carbonated soft drinks (III) is usually added during the manufacturing process. For example the label of the elder-lemon flavored „Biborțeni” beverage indicates 200 mg/L AA. Yet, recoveries are of approximately 65%.

Some alcoholic beverages (V) prove to be richer in AA than juices of class I (for example a few wines, especially the Rosé). One of the cherry brandies also has elevated AA content, probably because it was prepared by cold maceration of very ripe fruits. In contrast, preparation of the plum brandy requires distillation; hence, the ascorbic acid in the fruits breaks down when exposed to elevated temperatures.

It ought to be emphasized that data in **Figure 7** characterize this particular set of samples. Hence, fluctuations of C_{AA} values, as well as reversed orders are also possible, depending on the species, season and place of harvest of the fruits and vegetables. However, the data prove that besides freshly squeezed juices, pasteurized products and cold-pressed syrups are also a valuable source of vitamin C for the modern human diet.

Among the liquid food samples subjected to AA content determination, were 5 oils obtained by cold-pressing. For these, the „Iodometry 1” method was employed as usual. Therefore, the results should be interpreted differently. The oils do not mix with the aqueous reagent solutions. Yet, because ascorbic acid is water soluble, it is extracted to some extent from the oily into the aqueous phase (mixtures were ultrasonicated for 10 minutes). Hence, results in **Table 2** represent only partial values of each oil sample's AA content, yet still prove these to be good dietary sources of vita-

Table 2. Partial ascorbic acid content of cold-pressed oils.

Sample	C_{AA} (mg/L)
Walnut oil	535.6
Poppy seed oil	667.7
Grape seed oil	858.5
Sesame oil	271.5
Pumpkin seed oil	584.2

min C (values are comparable or higher than the best ones in **Figure 7**).

Table 3 shows the results for two types of honey: one already crystallized because of prolonged storage, the other fresh and liquid. Their aqueous solutions were subjected to „Iodometry 1” and the obtained values of C_{AA} showed no significant difference. Hence, even during a year long storage, honey still retains its vitamin C content intact.

Table 3. Ascorbic acid content of honey samples

Sample	C_{AA} (mg/100g)
Honey 1 (solid, crystallized during long storage)	42.9±18.0
Honey 2 (fresh, in liquid form)	65.3±11.8

Data above are in agreement with other findings for the local market: AA in acacia honey from Romania ranges between 77-99 mg/100g [20], and the mixed flower honey from Transylvania contains about 61 mg/100g AA [21]. Another study [22] mentions that honey usually has an ascorbic acid content between 0.34±0.00 and 75.8±0.41 mg/100g. Thus, results presented in **Table 3** are realistic, consistent with other reported data, and prove once more that the selected method is effective in ascorbic acid content determination of various food samples, as long as they can be brought in a liquid aqueous form.

3.3. Total antioxidant activity of analysed samples

Figure 8 illustrates the molecular absorption spectrum of ABTS in aqueous solution – see curve 1. It exhibits a maximum at 735 nm. At this wavelength its molar absorptivity coefficient, of 7484±753 L/mol.cm, was determined from the slope of an experimentally obtained Lambert-Beer line (triplicate measurements of 5 ABTS concentrations; correlation coefficient of 0.9945).

$$\Delta A_{735} = (1.57 \pm 1.48) \cdot 10^{-2} + (29642 \pm 2754.18) \cdot [AA] \quad (4)$$

Curve 1 was registered for a 5×10^{-5} mol/L ABTS concentration, whereas curve 2 corresponds to the same, but also contains 3×10^{-6} mol/L AA. Because of the reaction presented in **Figure 3** a stoichiometric amount of ABTS is consumed, and the absorbance of the mixture drops. Hence, by using various AA contents (up to 7.5×10^{-6} mol/L), calibration line (4) was obtained from differences such as that between curves 1 and 2. This expresses antioxidant activity in terms of ascorbic

acid concentrations, and as such, these ought to have higher values than the corresponding total AA contents of the respective samples.

Calibration line (4) has a correlation coefficient of 0.9834, and is based on triplicates of 7 measurement series, each at a different AA molar concentration, yet constant 5×10^{-5} mol/L ABTS.

In the case of a liquid food sample, the same amount of ABTS is added, and the 735 nm absorbance value is compared to that of curve 1. The samples have to be diluted so that their spectra lies under that of curve 1. **Figure 8** shows an example in curve 3, for a 500 fold diluted blackcurrant syrup. The antioxidant capacity is then expressed from the absorbance differences (ΔA_{735}) between curves 1 and 3, by means of equation (4). The same dilution of blackcurrant syrup is proven to have negligible absorbance values – see curve 4. Hence curve 3 is due, similarly to curve 2, only to the remanent ABTS content.

This method was applied to the aqueous solutions of Redoxon and Aspirin Plus C tablets. Results are presented in the last row of **Table 1**. The good recovery value of AA for Aspirin Plus C is in agreement with the fact that its only antioxidant species is ascorbic acid. On the other hand, in the case of the Redoxon tablet, recoveries exceeded 100%. This finding is in line with literature data [23], and probably due to the presence of other antioxidant species in the formulation.

Figure 9 illustrates in greenish-blue the results of such determinations, expressed as mg/L AA, for 11 randomly chosen beverages from among the considered samples described in Section 2.1.

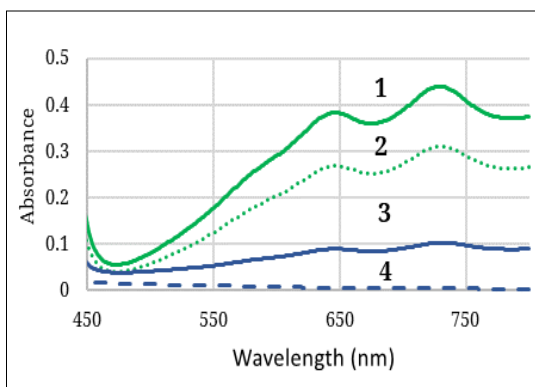


Fig. 8. Molar absorbance spectra recorded for: 1. a 5×10^{-5} mol/L ABTS aqueous solution; 2. solution 1 containing 3×10^{-6} mol/L AA; 3. a 500 fold diluted blackcurrant syrup containing 5×10^{-5} mol/L ABTS; 4. a 500 fold diluted blackcurrant syrup.

It can be observed that, as expected, the total antioxidant activity is usually higher than the ascorbic acid content illustrated by the orange color. Thus, it is not simply due to it, further proving that such beverages might be valuable sources of nutrients. The fruits and vegetables from which they are prepared also contain various flavonoids and anthocyanins with desired antioxidant properties.

Results in **Figure 9** are presented with their respective error bars. It is obvious that the employed titrimetric method is precise, accurate and reproducible, since relative standard deviation (RSD) values based on three distinct measurements range from 0.66% to 9.89%. On the other hand, the antioxidant activity values show poorer RSD values, within 10.51% and 37.88%. This lower precision might be due either to error propagation during the several consecutive but necessary dilution steps, or to the color (meaning non-zero 735 nm absorbance) of some samples.

4. Conclusions

In the context of rapid paced modern life, easy and sufficient Vitamin C uptake is of high importance for the human diet. Hence, its fast, reliable, and cost-effective determination from all kinds of food samples is an ongoing challenge.

Thus, a total of 41 food samples, mainly easy to consume beverages, were subjected to total ascorbic acid content determination. Two simple and cost-effective titrimetric methods were employed, both relying on the oxidation of AA by iodine. Yet only the one using back-titration of excess I_2 from

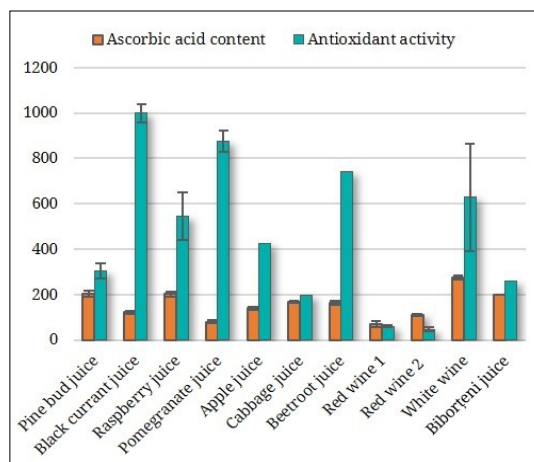


Fig. 9. Comparison between total ascorbic acid content and antioxidant activity. Both are expressed in mg/L AA.

the sample has proved to enable reliable and reproducible end-point detection. Results agreed with other reports, for example those referring to freshly squeezed orange juice, or to honey. For various cold-pressed oils only partial results could be obtained, but even so the high nutritional value of these has been proven.

For some of the beverages, total antioxidant activity expressed as ascorbic acid content, has been determined by means of a simple photometric method. Even if not as precise as the above-mentioned titrimetric technique, the procedure showed good results and proved once more the nutritional value of some analyzed products.

Both experimental techniques were validated by good recoveries from 2 commercially available pharmaceutical products with known ascorbic acid concentrations.

Acknowledgments

This work was carried out with the financial support of the Transylvanian Museum Association, Cluj-Napoca, Romania, within the framework of the external research project No. 433.6/2021.

References

- [1] López-Pastor J. A., Martínez-Sánchez A., Aznar-Poveda J., García-Sánchez A.-J., García-Haro J., Aguayo E.: *Quick and Cost-Effective Estimation of Vitamin C in Multifruit Juices Using Voltammetric Methods*. *Sensors*, 20. (2020) 676. <https://doi.org/10.3390/nano12040645>.
- [2] Lovander M. D., Lyon J. D., Parr D. L., Wang J., Parke B., Leddy J.: *Review—Electrochemical Properties of 13 Vitamins: A Critical Review and Assessment*. *Journal of The Electrochemical Society*, 165. (2018) (2) G18-G49. <https://doi.org/10.1149/2.1441704jes>
- [3] Carr A. C., Maggini S.: *Vitamin C and Immune Function*. *Nutrients*, 9. (2017) 1211. <https://doi.org/10.3390/nu9111211>
- [4] EFSA NDA Panel (EFSA Panel on Dietetic Products, Nutrition and Allergies): *Scientific Opinion on Dietary Reference Values for vitamin C*. *EFSA Journal*, 11. (2013) 3418. <https://doi.org/10.2903/j.efsa.2013.3418>
- [5] Feszterová M., Mišiakova M., Kowalska M.: *Bioactive Vitamin C Content from Natural Selected Fruit Juices*. *Applied Sciences*, 13. (2023) 3624. <https://doi.org/10.3390/app13063624>
- [6] Rowe S., Car A. C.: *Global Vitamin C Status and Prevalence of Deficiency: A Cause for Concern?* *Nutrients*, 12. (2020) 2008. <https://doi.org/10.3390/nu12072008>
- [7] Trifunski S.; Zugravu C. A.; Munteanu M. F.; Borcan F.; Pogurschi E. N.: *Determination of the Ascorbic Acid Content and the Antioxidant Activity of Different Varieties of Vegetables Consumed in Romania, from Farmers and Supermarkets*. *Sustainability*, 14. (2022) 13749. <https://doi.org/10.3390/su142113749>
- [8] Salara F. J., Sánchez-Bravo P., Menac P., Cámarad M., García-Viguera C.: *Comparison of Vitamin C and Flavanones between Freshly Squeezed Orange Juices and Commercial 100% Orange Juices from Four European Countries*. *International Journal of Food Sciences and Nutrition*, 75. (2024) 255–263. <https://doi.org/10.1080/09637486.2024.2303034>
- [9] Cendrowski A., Królak M., Kalisz S.: *Polyphenols, L-Ascorbic Acid, and Antioxidant Activity in Wines from Rose Fruits (Rosa Rugosa)*. *Molecules*, 26. (2021) 25–61. <https://doi.org/10.3390/molecules26092561>
- [10] Tantray A.K., Dar S.A., Ahmad S., Bhat S.A.: *Spectrophotometric and Titrimetric Analysis of Phytoascorbate*. *Journal of Pharmacognosy and Phytochemistry*, 6. (2017) 27–31.
- [11] Balogh T., Szarka A.: *A Comparative Study: Methods for the Determination of Ascorbic Acid in Small and Middle Sized Food Analytical Laboratories*. *Acta Alimentaria*, 45. (2016) 354–362. <https://doi.org/10.1556/aalim.2015.0017>
- [12] Xu H., Cai Q., Nie Q., Qiao Z., Liu S., Li Z.: *Ultra-sensitive Determination of Ascorbic Acid by Using Cobalt Oxyhydroxide Nanosheets to Enhance the Chemiluminescence of the Luminol–H₂O₂ System*. *Royal Society of Chemistry Advances*, 8. (2018) 23720–23726. <https://doi.org/10.1039/C8RA03528H>
- [13] Skrovankova S., Mlcek J., Sochor J., Baron M., Kynicky J., Jurikova T.: *Determination of Ascorbic Acid by Electrochemical Techniques and Other Methods*. *International Journal of Electrochemical Science*, 10. (2015) 2421–2431. [https://doi.org/10.1016/S1452-3981\(23\)04857-5](https://doi.org/10.1016/S1452-3981(23)04857-5)
- [14] Sharaa I. E., Mussa S. B.: *Determination of Vitamin C (Ascorbic Acid) Contents in Vegetable Samples by UV-Spectrophotometry and Redox Titration Methods and Estimation the Effect of Time, Cooking and Frozen on Ascorbic Acid Contents*. *International Journal of Progressive Sciences and Technologies*, 15. (2019) 281–293. <https://doi.org/10.52155/ijpsat.v15.2.1144>.
- [15] Griffiths H. R.: *Antioxidants: Characterization and Analysis, Encyclopedia of Food and Health*. Elsevier, Amsterdam, 2016. 221–226. <https://doi.org/10.1016/B978-0-12-384947-2.00037-4>
- [16] Alija D., Ziberi E., Xhabiri G., Idrizi X., Durmishii N., Ferati I.: *Control of Vitamin C (Ascorbic Acid) in Non-Alcoholic and Fresh Drinks*. In: UBT International Conference, Lambert Academic Publishing, Mauritius, 2017. 157. <https://doi.org/10.33107/ubt-ic.2017.157>
- [17] Oroian M., Escriche I.: *Antioxidants: Characterization, Natural Sources, Extraction and Analysis*.

- Food Research International, 74. (2015) 10–36.
<https://doi.org/10.1016/j.foodres.2015.04.018>
- [18] Dong J.-W., Cai L., Xing Y., Yu J., Ding Z.-T., *Re-Evaluation of ABTS•+ Assay for Total Antioxidant Capacity of Natural Products*. Natural Product Communications, 10. (2015) 2169–2172.
<https://doi.org/10.1177/1934578X1501001239>
- [19] Kumar S., Krishna Chaitanya R., Preedy V. R.: *Assessment of Antioxidant Potential of Dietary Components*. In: HIV/AIDS: Oxidative Stress and Dietary Antioxidants (Szerk.: Preedy V. R., Watson R. R.). Elsevier, London, 2017. 239–225.
<https://doi.org/10.1016/B978-0-12-809853-0.00020-1>
- [20] Al-Mosa A., Brima E. I., Fawy K. F., Ghrama H. A. A., Mohammed M. E. A.: *Antioxidant Vitamins in Honey Samples from Different Floral Origins and Altitudes in Asir Region at the South-Western Part of Saudi Arabia*. Current Nutrition & Food Science, 15. (2019) 296–304.
<https://doi.org/10.2174/1573401314666180606085841>
- [21] Dobrinás S., Matei N., Soceanu A., Birghila S., Popescu V.: *Estimation of Vitamin C and Cd, Cu, Pb Content in Honey and Propolis*. Scientific Study & Research, 7. (2006) 729–734.
- [22] Combarros-Fuertes P., Estevinho L. M., Dias L. G., Castro J. M., Tomás-Barberán F. A., Tornadijo M. E., Fresno-Baro J. M.: *Bioactive Components and Antioxidant and Antibacterial Activities of Different Varieties of Honey: A Screening Prior to Clinical Application*. Journal of Agricultural and Food Chemistry, 67. (2019) 688–698.
<https://doi.org/10.1021/acs.jafc.8b05436>
- [23] Szoke A., Zsebe Z., Turdean G. L., Muresan L. M.: *Composite Electrode Material Based on Electrochemically Reduced Graphene Oxide and Gold Nanoparticles for Electrocatalytic Detection of Ascorbic Acid*. Electrocatalysis, 10. (2019) 573–583.
<https://doi.org/10.1007/s12678-019-00543-4>



ROBOTICS TALENT MANAGEMENT AT UNIVERSITY OF NYÍREGYHÁZA

Gergely DEZSŐ

University of Nyíregyháza, Institute of Engineering and Agriculture, Department of Physics and Production Engineering, Nyíregyháza, Hungary, dezso.gergely@nye.hu

Abstract

Both in the economy and in research and development, there is worldwide growing demand for a competent workforce in the field of artificial intelligence and robotics applications. The educational system is developing answers to this need, this development, and the collection and evaluation of the experiences of the applications is a lively field of research. The target groups of the developed educational programs and methods range from kindergarten to university.

This paper presents the opportunities offered by the Hungarian competitions qualifying for the robotics competitions of the international RoboCup Community for primary and secondary school students, and how this is realized at the University of Nyíregyháza. The leagues of the competition and the experiences gained so far are demonstrated.

Keywords: *talent management, robotics, RoboCup Junior, STEMIE, A-STEM.*

1. Introduction

In the society and economy of the 21st century, there is an ever-increasing demand for a talented workforce with competencies related to the use of artificial intelligence. At the same time, computer programming and the use of artificial intelligence applications are often associated with robotics. This is also increasingly common in education.

This paper reports on the robotics competitions that have been held at University of Nyíregyháza for 17 years now, which offer participants the opportunity to participate in competitions and exhibitions of the international RoboCup community. Teams of primary and secondary school children can join the RoboCup Junior program.

2. Robotics and education

In a previous work [1] the author gave an overview of the two types of connection between robotics and education. One way to connect is if robotics is the subject or topic of education, i.e. the students learn robotics. The other connection is when robotics becomes a tool for education. This study deals with the first approach.

The scientific literature deals separately with the possibilities, results and challenges of edu-

cating children in early childhood (kindergarten age) and K12 (primary and high school).

E. Pollarolo et al. [2] prepared a summary of the use of programmable games in early childhood development. Based on the processed sources, it was shown that the programmable games used in the kindergarten not only develop computer user skills, but also problem-solving and communication skills. They emphasized that, in addition to the professional knowledge of the teachers, their methodological preparation also plays a very important role in ensuring that the use of programmable games optimally supports the development of the children's personality and abilities. J. Su and Y. Zhong examined curricula prepared for young children [3] in terms of objectives, content, methods and pedagogical evaluation. Among other things, they mention the five major topics proposed by the AI4K12 organization, which are perception, representation and conclusion, learning, natural-like relationships, and social impact. They emphasize that among the educational methods, the project-based method is considered the most suitable for teaching artificial intelligence, for which robots are used in most cases.

F. Martin and his colleagues [4] investigated how artificial intelligence appears in the education of the K12 age group. The applications extend to the most diverse areas, such as the analysis and prediction of student progress, the development of teaching materials for artificial intelligence education and the support of the teaching of certain subjects. The study points out that robotics applications are gaining more and more space in education. According to S.J Lee et al. [5] there is a growing need for computer science education, and robots play a fundamental role in this. Among the methods and tools of education, the theoretical foundation is mentioned, the general process of education is presented, the role of real and virtual tools, activities with and without a computer, educational experiences in the field of graphic and text programming. S. T. Chu et al [6] investigated the use of artificial intelligence-based robots in education. They point out that robots can have a teaching role in the educational process, or they can appear as a tool used by students.

Y. W. Cheng and his co-authors [7] examined the expectations of robots in the field of education using the methods of literature research, interviews with experts and the analysis of reports received from educators. Fourteen areas of applications and related expectations were identified, among which language teaching, educational robots and robot pedagogical assistants were the most popular. The complexity and depth of the solutions based on artificial intelligence were divided into five levels. The first level represents perception, recognition of words and straight line movements. On the second level, problem solving, planning, understanding expressions and plane movements appear. In the case of the third level, navigation, manoeuvring, interpretation of sentences, and movement of body parts are used. The fourth level includes the programming of learning, discovery, dialogue, fine movements. At the fifth level, self-awareness, recognizing the meaning of speech, and micro-movements are realized.

G. Nugent and co-authors [8] investigated the effectiveness of a robotics education program in different settings within the United States, developed by the University of Nebraska-Lincoln for 9-14 year olds. With the involvement of 5,000 students and 400 teachers, they researched what results were achieved with the educational program in camps, clubs and competitions. It turned out that technical knowledge and programming skills were well developed by the program, but mathematical skills were essentially not strengthened.

The students' problem-solving and error-finding skills improved significantly from the level of trying ideas to systematic, planned activities. Not only did the students' knowledge and skills improve, but their interest in technical careers also increased.

The Finnish research group of T. Oksanen presents the experience of a robot competition over a 5-year period [9].

It can be concluded that robotics plays an important role in education from many points of view, the most important of which are the following:

Development of creative thinking and problem-solving, development of technological skills, development of cooperation and teamwork skills, understanding of real-life applications, increasing motivation and interest, development of critical thinking. Robotics is an exciting and interactive activity that arouses students' interest in STEM (Science, Technology, Engineering, Mathematics) fields and motivates them to learn.

All in all, the introduction of robotics into education can help in the broad development of students, preparing them for the challenges and opportunities of the future.

3. The RoboCup Federation

The history of the international RoboCup Federation dates back to 1992, when Professor Alan Mackworth raised the idea of soccer-playing robots in a scientific paper. In the same year, independently of him, Japanese researchers at a workshop discussing the great challenges of artificial intelligence also came to the game of football. More and more leading research and development companies joined the further development of the idea. After the pre-RoboCup held at a conference in 1996, the first official RoboCup competition took place in 1997 with the participation of 40 teams and 5000 spectators in Nagoya, Japan [10]. This event is not just a competition, but an international scientific conference, exhibition and science popularization event in which the world's best development teams from universities and companies participate. It didn't take long for the idea of the RoboCup Junior event for young people to come up, which first took place in 1998 in Paris. The international competition for young people and adults is organized at the same time and place, so students have the opportunity to meet the leading researchers in robotics in person and see the solutions they have prepared.

4. The RoboCup Junior

Amy Eguchi, co-president of the RoboCup Federation, representative of RoboCup Junior, presents [11] the goals of RoboCup Junior and the results of a survey among competitors. We highlight three of the features of RoboCup Junior here. The first is a competition task that is renewed every year but contains the same goals within each league, which helps students to develop their knowledge in a well-structured environment. The second characteristic is the focus on education, which means that the technical committees of the leagues use intensive background work to determine exactly how each competition task should differ from the previous year. The third is lifelikeness, which aims to strengthen students' interest and motivation.

Robocup Junior has three main themes: escape, football and theatre. Within these, several so-called leagues are announced with slightly different and challenging conditions.

5. Robotic competitions at the University of Nyíregyháza

In 2006, we organized the first RoboCup Junior competition at University of Nyíregyháza. That year, the Hungarian teams already represented

Hungary in the international competition, so that they managed to bring home prizes. The initiator of the competitions and the contact person of the Hungarian RoboCup Community is Simon Béláné dr. Ágnes Balogh is a college teacher.

After that, the Hungarian Youth Robot Cup is held every year, which is the qualifying competition for the international RoboCup Junior competitions. The team that successfully qualifies in the domestic competition can apply for the world competition.

Over time, it became necessary to organize the competition in two installments. Currently, the escape leagues take place at a separate event, and the other leagues at another event.

Fig.1 shows the participants of the 2024 Hungarian Youth Robot Cup competition organized at the University of Nyíregyháza.

Fig. 2 shows a snapshot of one of the simulation leagues. Here, you have to write your own program running in a predefined framework software, with the help of which the simulated robot implements tasks.

Fig. 3 shows a match of one of the soccer leagues. The robots of the Rapidly Manufactured Robot Competition (RMRC) (Fig. 4) have to travel along a path imitating a difficult terrain while performing image recognition and manipulation tasks.



Fig. 1. Participants of the Hungarian Youth Robot Cup 2024 competition in Nyíregyháza.



Fig. 2. Rescue simulation league: here you have to write your own program, which runs within a framework software, based on given rules, but you have to complete tasks on an unknown course.

In the on stage leagues (**Fig. 5**) the teams have to present a stage choreography in which the robots are the protagonists, but the value of the presentation increases if they also cooperate with humans. Here, the scenery and the artistic realization are also on point.

One of the two main types of escape leagues is based on the task of following a line (**Fig. 6**), the track of the other type does not have a leading line, but rather resembles a labyrinth (**Fig. 7**).

It applies to all leagues that you have to compete with an autonomous robot. The competition rules are the same as the international rules for the competition in Hungary as well. The teams must



Fig. 3. Robot soccer.

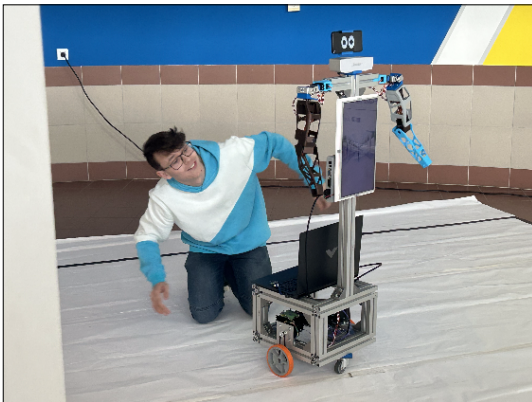


Fig. 5. On stage league.



Fig. 4. RMRC league.

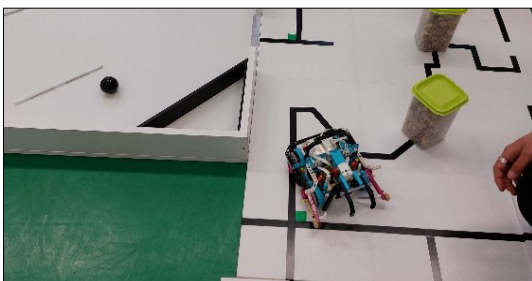


Fig. 6. Rescue league line following.

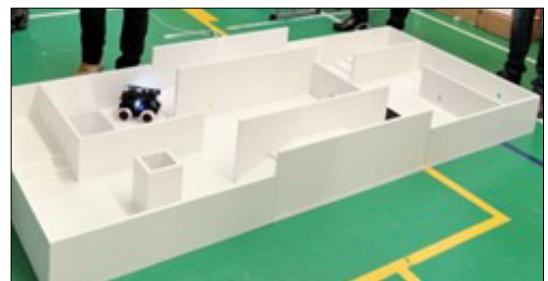


Fig. 7. Rescue league labyrinth.

be able to present the progress and professional content of their preparation with a presentation in English.

Each league's rules include the key phrase: "It's not about where you rank, it's about what you learn."

6. Conclusions

The multifaceted role of robotics and artificial intelligence in education is changing every day and is an area of active research.

The associate organization of the international RoboCup association is RoboCup Junior, which presents well-founded pedagogical challenges to youngsters that systematically change from year to year.

The Hungarian Youth Robot Cup is the qualifying competition of the RoboCup Junior international events, which has been held at the University of Nyíregyháza since 2006. The event is currently held at two locations.

At this event every year, the participants have the opportunity to learn about the challenges of the international RoboCup Junior and qualify for the world competition.

Acknowledgements

This project was supported by the Scientific Council of the University of Nyíregyháza.

References

- [1] Dezső G.: *Integration of Robotics into Education*. Acta Academiae Nyiregyhaziensis, 7. (2022) 250–255.
- [2] Pollarolo E., Papavlasopoulou S., Granone F., Reikerås E.: *Play with Coding Toys in Early Childhood Education and Care Teachers. Pedagogical Strategies, Views and Impact on Children's Development. A Systematic Literature Review*. Entertainment Computing, 50. (04) 100637. <https://doi.org/10.1016/j.entcom.2024.100637>
- [3] Su J., Zhong Y.: *Artificial Intelligence (AI) in Early Childhood Education: Curriculum Design and Future Directions*. Computers and Education: Artificial Intelligence. 3. (2022) 100072 <https://doi.org/10.1016/j.caeai.2022.100072>
- [4] Martin F., Zhuang M., Schaefer D.: *Systematic Review of Research on Artificial Intelligence in K-12 Education (2017–2022)*. Computers and Education: Artificial Intelligence, 6. (2024) 100195. <https://doi.org/10.1016/j.caeai.2023.100195>
- [5] Lee S. J., Francom G. M., Nuatomue J.: *Computer Science Education and K-12 Students' Computational Thinking: A Systematic Review*. International Journal of Educational Research, 114. (2022) 102008. <https://doi.org/10.1016/j.ijer.2022.102008>
- [6] Chu S.-T., Hwang G.-J., TuY.-F.: *Artificial Intelligence-Based Robots in Education: A systematic Review of Selected SSCI publications*. Computers and Education: Artificial Intelligence, 3. (2022) 100091. <https://doi.org/10.1016/j.caeai.2022.100091>
- [7] Cheng Y.-W., Sun P.-C., Chen N.-S.: *The Essential Applications of Educational Robot: Requirement Analysis from the Perspectives of Experts, Researchers and Instructors*. Computers & Education, 126. (2018) 399–416. <https://doi.org/10.1016/j.compedu.2018.07.020>
- [8] Nugent G., Barker B., Grandgenett N., Welch G.: *Robotics Camps, Clubs, and Competitions: Results from a US Robotics project*. Robotics and Autonomous Systems, vol. 75. (2016) 686–691. <https://doi.org/10.1016/j.robot.2015.07.011>
- [9] Oksanen T., Kostamo J., Tamminen P., Tiusanen J.; *Robot Competition as a Teaching and Learning Platform*. IFAC Proceedings Volumes, 44/1. (2011) Art. no. 1. <https://doi.org/10.3182/20110828-6-IT-1002.03324>
- [10] A Brief History of RoboCup. [Online]. Available: https://www.robocup.org/a_brief_history_of_robocup
- [11] Eguchi A.: *RoboCupJunior for Promoting STEM Education, 21st Century Skills, and Technological Advancement through Robotics Competition*. Robotics and Autonomous Systems, 75. (2016) 692–699. <https://doi.org/10.1016/j.robot.2015.05.013>



CONSTRUCTION OF MPA ANTENNA ROTATION SYSTEM FOR INTERFERO-METRIC “IN-SITU” MEASUREMENTS

Szabolcs Sándor DIÓS,¹ Abdullah MASUK,² Tamás DINYA,³ Attila SZÁNTÓ,⁴
Dávid PETTENDI,⁵ István BALAJTI⁶

¹ Debrecen University, Mechatronics Department, Debrecen, Hungary, dios.szabolcs@eng.unideb.hu

² Debrecen University, Vehicles Engineering Department, Debrecen, Hungary, masuk@eng.unideb.hu

³ Debrecen University, Faculty of Engineering, Debrecen, Hungary, tamasdinya@gmail.com

⁴ Debrecen University, Doctoral School of Informatics, Debrecen, Hungary, szanto.attila@eng.unideb.hu

⁵ Debrecen University, Mechanical Department, Debrecen, pettendid4@gmail.com

⁶ Debrecen University, Mechatronics Department, Debrecen, balajti.istvan@eng.unideb.hu

Abstract

The primary objectives of the project are to build a complex antenna rotation facility that will enable the structure to perform in situ interferometric measurements. The objectives include the construction of a stable frame to support and protect the control electronics, the design and fabrication of a 2.4GHz DTMPA (Dual Triangular Microstrip Patch antenna), and the support of the control electronics with the appropriate software background. The finished structure is capable of tracking the orbit of a satellite of your choice, up to NAP orbit depending on the configuration. The implementation can be divided into four steps. First of all, a sufficiently solid frame was designed and built. From the point of view of the use of materials, LEGO construction toys are the right choice, both in terms of weight and strength. The second step is to design and build the DTMPA. This is followed by the selection and implementation of the appropriate control electronics. The stepper motor must have adequate torque to ensure proper rotational motion, and the motor and microcontroller must provide clear instructions to the motors. Finally, the code responsible for controlling the motors must be written and implemented in the microcontroller so that the structure can be controlled by the appropriate external computer.

Keywords: *Interferometry, DTMPA, Antenna performance measurement, Microcontroller.*

1. Introduction

At the Faculty of Engineering, developments in the field of vehicles will be crucial in the coming years and research in this direction has been carried out at the Faculty [1–3]. There have also been advances in the field of artificial intelligence [4, 5]. The design provided by Cyber-Physical Systems has helped other research to progress faster [6, 7]. Taking this into account, the following paper has been prepared on the topic of radar sensors for vehicles.

In order to achieve the objectives set out, complex filming equipment will be designed and manufactured, as well as the DTMPA, which is essential for operation. A number of measurements necessary for antenna performance are carried

out, which are essential for the completion of the task. After the integration of the software and hardware elements responsible for the movement, as well as the assembly of the finished system and the implementation of the software that serves them, the equipment can track the movement of a pre-selected satellite or the sun.

2. Radar Systems Need

This project introduces the concept of mechatronics, which has been used as a concept since the 1960s. This discipline combines mechanics, electronics, and computer technology, making it possible to create complex systems such as robots, engines, and electric vehicles [8, 9]. The topic is based on interferometric In Situ measure-

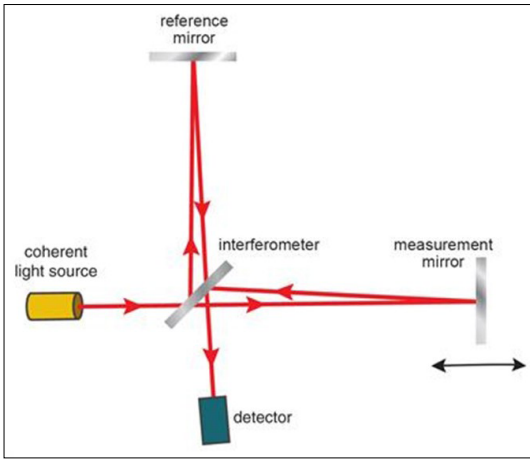


Fig. 1. Basic principle of interferometry [11]

ments. Interferometry is based on the principle of using waves, in a narrower circle, electromagnetic waves and then extracting information based on the phenomenon of interference created by them. Interferometry (Fig. 1) is a technique used to perform tasks that require very high measurement accuracy to measure the properties of various waves, vibrations, sounds, electromagnetism, or gravity. The most common fields of application for interferometry are astronomy, quantum physics, meteorology, and oceanography [10]. In industry, it is mainly used when measuring small displacements and unevenness.

3. Requirement & Consideration

In order to achieve the objectives of the project, several coordinated areas must be created. A frame with a sufficiently stable base that holds the components together and provides them with mechanical protection is essential. It is essential to design and build a DTMPA with appropriate characteristics, as well as a stepper motor that ensures the rotation of this antenna, and the corresponding control electronics and software background.

Designing a DTMPA must be preceded by adequate research. An antenna is a transducer that transforms electromagnetic waves into electrical power and vice versa. It has the ability to operate as a transmitting and receiving antenna. In 1888, German physicist Heinrich Hertz constructed the first antennas [12]. James Clerk Maxwell's electromagnetic theory was confirmed through his experiments [13].

The key invention for manipulating the components of the electromagnetic field, such as (1), (2),

(3) and (4) is crucial in revealing the exponential function of the antenna's far-field pattern [14].

$$E(r, \theta, \varphi) = E_1(r_1, \theta, \varphi) + E_2(r_2, \theta, \varphi) + E_3(r_3, \theta, \varphi) + E_4(r_4, \theta, \varphi) \quad (1)$$

In the far-field, the equation for the normalized scalar field is:

$$E(r, \theta, \varphi) = f(\theta, \varphi) \frac{e^{-jkr_1}}{r_1} - f(\theta, \varphi) \frac{e^{-jkr_2}}{r_2} + f(\theta, \varphi) \frac{e^{-jkr_3}}{r_3} - f(\theta, \varphi) \frac{e^{-jkr_4}}{r_4} \quad (2)$$

$$E(r, \theta, \varphi) = \left[e^{+jk\cos\psi_1} - e^{+jk\cos\psi_2} + e^{+jk\cos\psi_3} - e^{+jk\cos\psi_4} \right] f(\theta, \varphi) \frac{e^{-jkr}}{r} \quad (3)$$

where

$$\frac{E}{E_0} = AF(\theta, \varphi) = 2[\cos(ks \sin\theta \cos\varphi) - \cos(ks \sin\theta \sin\varphi)] \quad (4)$$

The azimuth panel ($\theta = \pi/2$), along with the array factor of the entire reflector system reduce to:

$$\begin{aligned} \frac{E}{E_0} &= AF\left(\theta = \frac{\pi}{2}, \varphi\right) = \\ &= 2[\cos(ks \sin\theta \cos\varphi) - \cos(ks \sin\theta \sin\varphi)] \end{aligned} \quad (5)$$

The term "gain" refers to a parameter that indicates how ostensibly directed the radiation pattern of an antenna is. A low-gain antenna will radiate over a wide area, whereas a high-gain antenna will direct the majority of its power in a particular direction when it emits electromagnetic waves. At a wavenumber of zero ($k = 0$) and an azimuth angle ($\theta = 90^\circ$), the antennas' phased array has a normalized power gain (G):

$$G(\theta) = \left| \frac{\sin\left(\frac{Nkd}{2}\right) \cos\theta}{N \sin\left(\frac{kd}{2}\right) \cos\theta} \right|^2 \quad (6)$$

A high-gain antenna has a longer range and better signal quality, but it must be developed, maintained, and installed in accordance with different antenna systems (Fig. 2).

After choosing the right antenna, it is necessary to determine the appropriate feeding method for the project objectives. The most common types of MPA antennas, due to their technical parameters and production costs, are the "monopole", "dipole" and "loop" antennas [16].

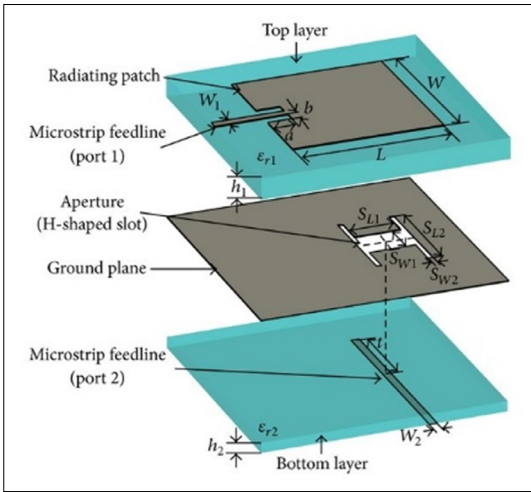


Fig. 2. The microstrip patch antenna. [15]

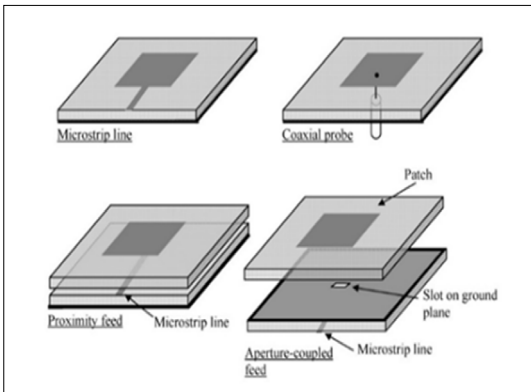


Fig. 3. MPA feeding methods.

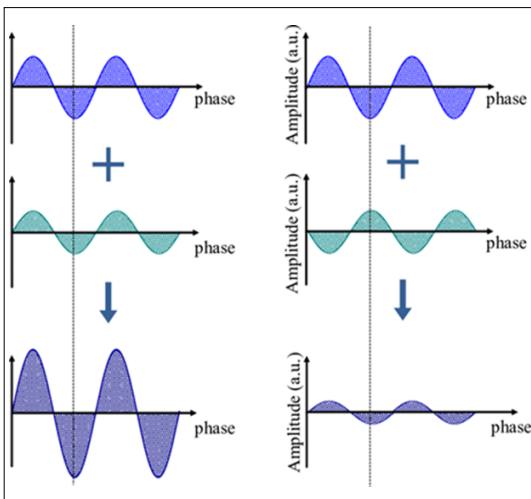


Fig. 4. Constructive and destructive interference.

These antennas must be powered in different ways. The four most common of these feeding methods are "microstrip line", "coaxial probe", "proximity feed" and "aperture-coupled feed". (Fig. 3).

In short, "microstrip feed" is the fastest and simplest, "aperture coupling" is the most difficult to manufacture, and "proximity coupling" has the highest bandwidth.

In the course of the literature review, the phenomenon of interference must be familiarized. We can talk about the phenomenon of interference interfering with measurements when the signal received in the bandwidth given by the antenna is mixed with other interfering signals, e.g. influenced or distorted by noise, modulated or other sources of electromagnetic radiation [17]. Interference can occur in several ways. It can be caused by nearby antennas, metal objects interacting with each other, or the presence of electronic devices. At the same time, naturally occurring lightning and other nearby buildings and rock walls can also cause reflections. A common cause of interference is the presence and proximity of other antennas operating in the same frequency range. Signals reflected back from different signal sources or from objects in our environment interfere with each other as described in Chapter 1. . Consequently, the signal strength we expect is reduced, distorted, and the signal-to-noise interference ratio can lead to complete signal loss. It can often be caused by electronic devices, such as radio-television transmission towers, electronic wires, or other communication equipment and other electronic noise sources (Fig. 4).

In order to move the corresponding components, it is necessary to embed stepper motors [18]. This type of motor is a brushless design, otherwise known as BLDC (brushless DC), which causes the rotating movement with a series of electrical pulses. In terms of operation, they can be divided into two parts, a stationary (stator) and a rotating (rotor) part [19]. In terms of design, it can be permanent magnetic, where the rotating part is a permanent magnet, as well as variable reluctance, where the rotating part is a plated iron core, which is magnetized by an electric current. The hybrid engine is a combination of these two designs [20, 21]. Their operating principle is based on magnetic attraction. Both the stationary and the rotating parts have teeth and grooves on which, if an opposite magnetic polarity develops, the half of the tooth with the opposite polarity closest to it in space moves, if the distance be-

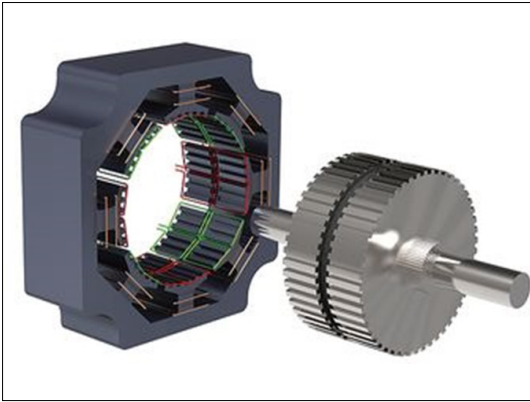


Fig. 5. Hybrid stepping motor [22]

tween them is sufficiently small. We call this a surprise, hence the term stepper motor. This step can be full, up or micro surprise. In the case of a hybrid stepper motor (Fig. 5) the rotating part is the shaft itself, with two reluctance type ferromagnets with a phase shift of half from each other, and a permanent magnet with axial magnetization between them. The rotating part segments represent opposite magnetic poles.

4. Findings

The assembly of the finished, working equipment of the project was preceded by thorough research work. Fig.6 illustrates the structure of the equipment.

The signals received by the antennas controlled by the antenna mast are sent to the 4ChVNA device, amplitude and phase are correctly sampled and then processed. The task of the R&S signal generator in actuator mode is to generate the desired signal structures and sequences and transmit them to the antennas via a 50 Ohm cable.

4.1. The DTMPA Antenna

An important aspect of the project is the DTMPA located on top of the camera. The construction of this antenna was preceded by several design processes. The most important of these is designing the antenna in the MATLAB simulation environment. During the design process, with the help of the "antenna array designer" built into the software, and by specifying the desired 2.4GHz frequency, the software simulated the rough sketch of the future antenna. This sketch (Fig. 7) required many manual corrections in order to function properly. (e.g. material use, substrate thickness).

4.2. The antenna mast and the subsystems required for operation

The construction of the DTMPA presented above has always been among the objectives. Once the design process is completed, the achieved results will be produced at a later date due to financial reasons, with the recognition of the expert opinion of the faculty. The rationale for this was keeping costs and time efficiency in mind. In addition, it is important to point out that the department had several existing antennas at the end of the design, several of which met the objectives of the project. Therefore, in the future, we will use two existing antennas in order to achieve the goal, the documentation and measurement results of which are detailed below.

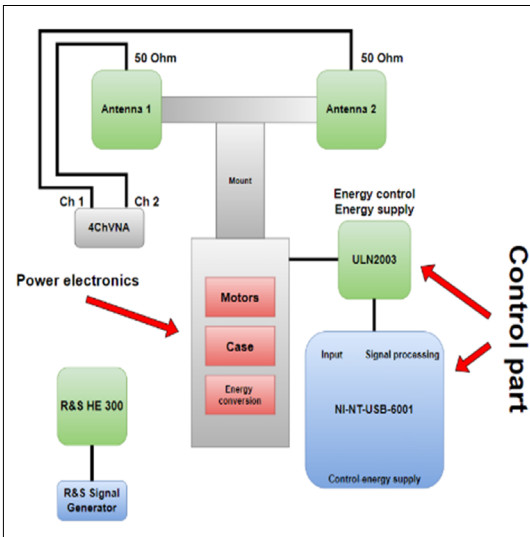


Fig. 6. The antenna mast and the subsystems required for operation

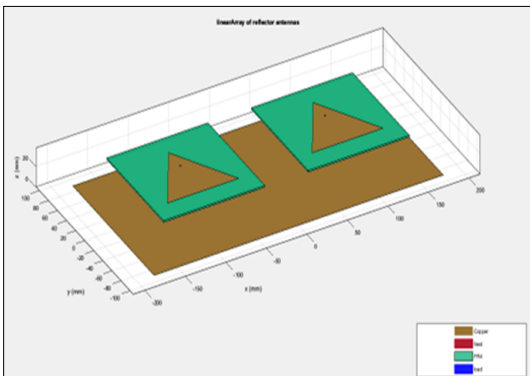


Fig.7. Dual Triangular Microstrip Patch antenna (DTMPA)

The physical parameters of the provided antennas are the same. Both use an FR4 substrate, on which the "slot" itself is located. This is followed by an air substrate layer, and then a copper base plate is placed below this. The distance between the two plates, i.e. the $\lambda/4$ value for both antennas, is 5.4 cm. The double of this, i.e. the $\lambda/2$ value, will be the distance that must be between the feed points of the two antennas in order to be used in an "array" design. Both antennas receive power through a standard coaxial connector located at the bottom of the antenna. Fig. 8. and 9 show some measured values of the "L" band antenna and Table 1. shows "L" band antenna performance measurements with different frequencies.

5. Antenna Performance Measurement

The antenna used in the project had to be subjected to measurements in order to gain certainty that it is suitable for the objectives of the topic. For this purpose, two measurements were performed. A simple antenna performance measurement, as well as a more complex near-field antenna measurement. We determined the characteristics of the existing slot resonator antenna with two independent measurements. The first measurement was taken from several different positions in the case of a fixed antenna. In the assembly according to Fig. 10. Several different measuring devices were used for the measurement. The ROHDE & SCHWARZ SMB 100B signal generator supplying the antenna provided the necessary signals, first at 1.3 and then at 2.4 GHz frequency. For both settings, a "level" value of 4dBm was set.

During the measurement shown in Fig. 11 we used a 360-degree rotatable measuring bench in order to determine the 360-degree characteristic of the antenna. We used an R&S HE 300 antenna connected to a 4ChVNA signal generator as a "transmitting" antenna. The data was evaluated on a computer connected to the signal generator. The distance between the "receiver" and "transmitter" antenna was 2.6m. During the measurement, we slowly turned the rotatable measuring bench around several times, and then performed the same sequence of movements in the opposite direction. Fig. 12 shows the rotatable measuring bench.

5.1. Stepper Motor Subsystem

The frame is moved by two mini stepping motors. In terms of their movement, horizontal and vertical circular movement. The lower motor ensures the rotation of the frame on the axis, while

Table 1. „L” band antenna performance measurements with different frequencies

„L” band antenna		
Frequency	1.3 GHz	2.4 GHz
Back radiation	-46.6dB	-43.6dB
Turned 60° to the right from the main beam	-39.5dB	-37.5dB
Turned 60° to the left from the main beam	-37.6dB	-36.2dB
Main beam maximum (horizontal polarization)	-25.6dB	-24.6dB
Cross polarization value	-58.6dB	-58.2dB
Main beam maximum (vertical polarization)	-25.8dB	-22.6dB

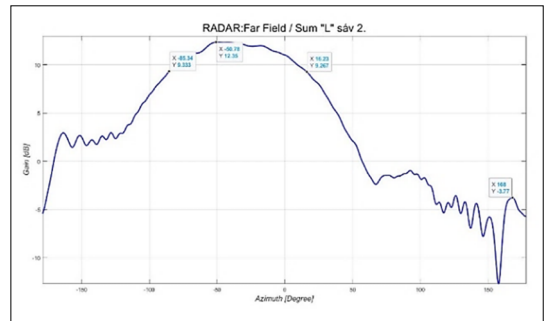


Fig. 8. Measured "L" band antenna radiation pattern.

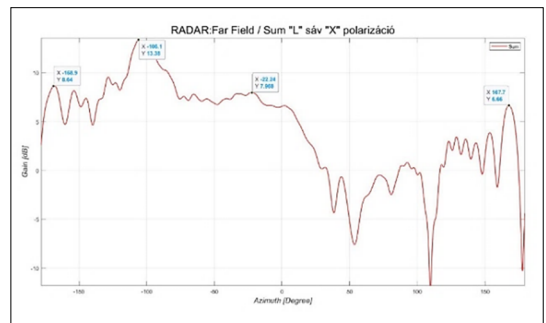


Fig. 9. Measured "L" band antenna radiation pattern with x-polarization.

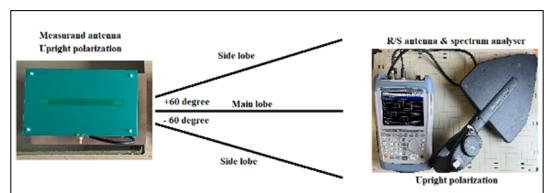


Fig.10. Simplified antenna characteristic measurement arrangement

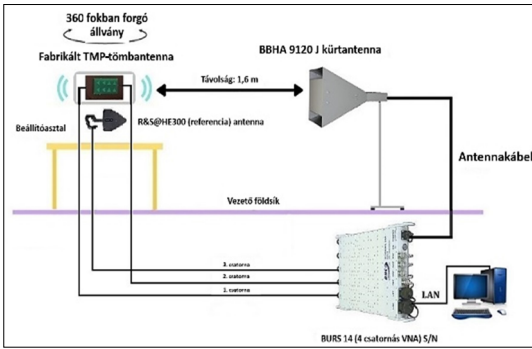


Fig. 11. Description of the measurement environment.

```

azMaxStep = 100
elMaxStep = 100
azMax = 360
elMax = 90

NoHaltMotorsGlobal = True
donePositioning = True
resetMotors = False
calibration = False
doneCalibration = False
currAzPos = 0
currElPos = 0
shutdownThreads = False
    
```

Fig. 13. The maximum number of steps for running the motors.



Fig. 12. „L” band antennas.

```

def set_output_states(states, stepDelay, sel):
    if sel==1:
        for i in range(len(states)):
            task2.write(np.array(states[i], dtype=bool), auto_start=True)
            if stepDelay != 0:
                time.sleep(stepDelay)
    else:
        for i in range(len(states)):
            task1.write(np.array(states[i], dtype=bool), auto_start=True)
            if stepDelay != 0:
                time.sleep(stepDelay)
    return 0
    
```

Fig. 14. The code responsible for the function causes the motors to move.

the upper one rotates the antenna support panel vertically at the desired angle. Fig. 13 shows the maximum number of steps for the specified position angle and lateral angle, as well as the declared variables that the main thread writes to instruct the thread responsible for running the motors.

The two SM-28BYJ-48-5V motors used [23] are four-phase, unipolar. Its torque is adequate, taking into account the above-mentioned weight issue, so it is able to ensure the appropriate rotational movement. The motor located at the top of the structure is directly responsible for the vertical rotation of the antenna, while the lower one is responsible for the horizontal rotation of the entire frame. Fig. 14 shows the code fragment responsible for the function that causes the motors to move clockwise and counterclockwise.

The motor can be controlled with two motor controllers, nominally a ULN2003. Its physical appearance can be seen in Fig. 15.

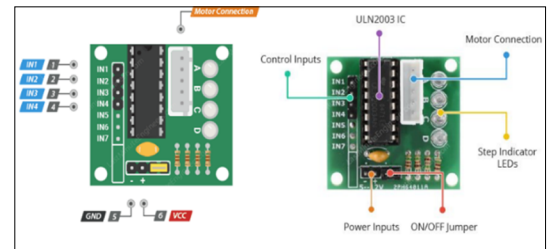


Fig. 15. ULN2003 motor controller.

5.2. Stepper Motor Programming

The project uses a NI USB 6001 data acquisition card connected to a computer that supplied it with the control commands. An application written in the Python programming language is running on this computer. The NI DAQMX library was imported into the mentioned Python code, which contains the functions needed to control the data acquisition card. The communication protocol

used by the hamLib library in the TCP/IP application layer was implemented in the same code.

The gpredict open-source software was chosen as the basis for the engine control.

Gpredict is a real-time satellite tracking and prediction app. It monitors and displays satellite positions and data through lists, tables, maps, and polar plots. It forecasts future satellite passes, and uniquely, you can group satellites into customizable modules for a personalized look and functionality. Plus, Gpredict can track satellites from multiple observer locations concurrently, but its key advantage is that it can handle antenna rotators and radios that support the hamlib protocol.

So gpredict tracks the selected satellite, calculates the azimuth and elevation angles for the rotator according to our own position and transmits via TCP/IP using hamlib protocol at the application layer.

A program written in Python receives commands as a server through the hamlib protocol and controls and monitors the stepping motors via a NI USB 6001 device. In the first step, the program initializes and loads the appropriate libraries to control the NI USB 6001, then loads the configuration file, which specifies how many steps it can take on each of the two axes, and in the final states, the angles at which the steps correspond according to the hamlib.

In calibration mode, the axes can be moved independently; if you reach the end stop on one axis, the counter will be reset; if you move it in the opposite direction, the counter will count each step instruction.

If we think we have reached the maximum possible step on a given axis or the limit stop is pressed again, we can save the maximum possible steps in a configuration file.

In normal running mode, after loading the configuration file, a TCP/IP server is started, which decodes the hamlib commands and gets the positions in angles. These angles are converted into step numbers according to the configuration file. From then on, the control works like a CNC machine; the program knows exactly how many steps the motor is taking in relation to the end position, "governs" it so that the set steps are not exceeded, and knows how many steps to take in one direction or the other in relation to the new position. Fig. 16 shows the software topology.

5.3. Software topology

The stepper motors are controlled by a micro-controller that schedules and supplies the motors

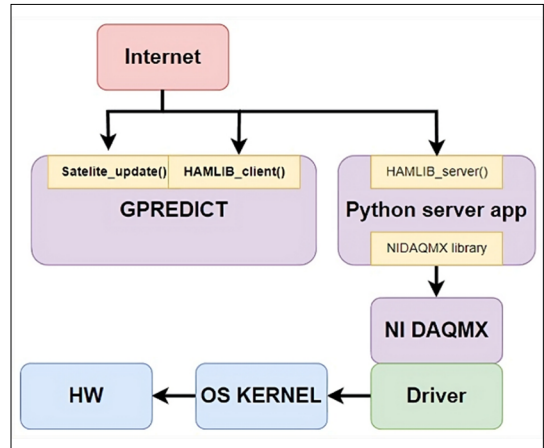


Fig. 16. Software topology.

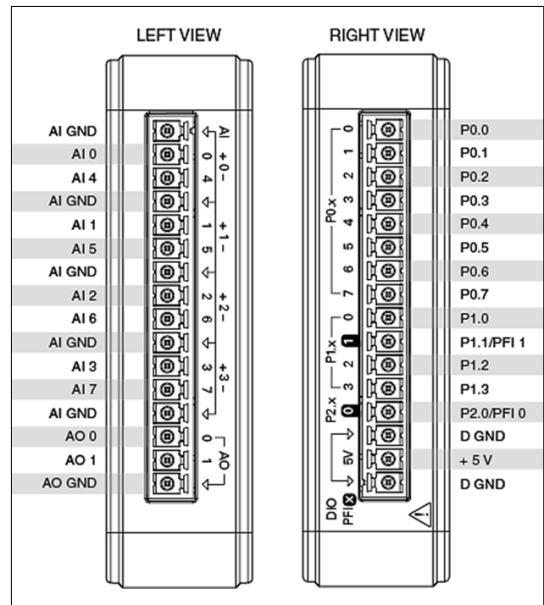


Fig. 17. NI-NT-USB-6001.

with the appropriate instructions. The choice fell on a NI-NT-USB-6001 device. See in Fig. 17, the NI-NT-USB-6001 is a versatile device suitable for many applications including laboratory experiments, research and development, and industrial automation. Due to its small size, portability and easy handling, it offers an ideal solution for many measurement and control tasks, such as for moving the antenna system of the interferometer stand. The NI-NT-USB-6001 is a multifunction data acquisition device designed and manufactured by National Instruments (NI). The device is a small,

portable USB-based data acquisition module that provides analog and digital inputs and outputs, as well as a counter/timer function. NI-NT-USB-6001 has 8 analog input channels with 14-bit resolution and 48 kS/s sampling rate. It has 2 analog output channels with 16-bit resolution and a maximum update rate of 2 kS/s [24].

5.4. The Build Area Unit

To hold the various electronic components together, as well as to fix the antenna, a frame is required that is sufficiently stable. In order for the appropriate elements to be fixed, a complex framework had to be created that meets several aspects. First of all, it was necessary to take care of the understanding of the two stepping motors, since thanks to them the rotating movement is realized. In addition, proper fixing of the micro-controller and the mounting panel is also crucial. One of the most critical features of a frame is its weight. Stepper motors have a maximum load capacity. Exceeding this, the system will not be able to function properly as far as the rotary movement is concerned. Although the metal house is the most durable and stable, due to the weight limit, we decided on the plastic building equipment called LEGO. Sufficiently stable, highly customizable.

However, it is important to note that LEGO is made from ABS, an industrial plastic. Before building the Antenna frame, 3D modelling [26] was carried out. This will make it easier to redesign and to see the frame to be built in a virtual framework. We can also make the necessary parts list. The free BrickLink studio [26] was used for modelling, allowing the design of customized components, import and export of models and the creation of building guides.

Once the design was complete, a list of the elements needed to build it was available. Minimal modification was required to the physical antenna rotator (see Fig. 19).

After building and testing the project, it can be determined that it meets the expected and defined requirements. The motors are able to rotate the frame adequately, the Python application properly handles and transmits the signals, and the measured characteristics of the antenna are also suitable for the objectives.

6. Conclusions

In the course of the project, opportunities for further development arose in several directions. Perhaps the most important of these is the design of

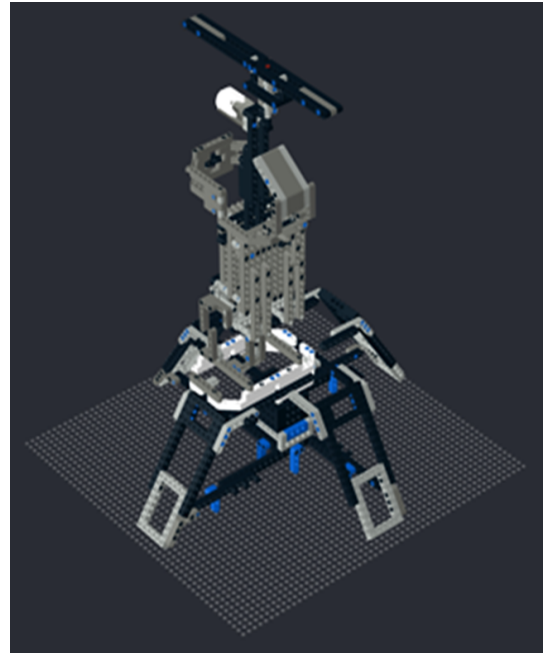


Fig. 18. 3D designed of the antenna frame.

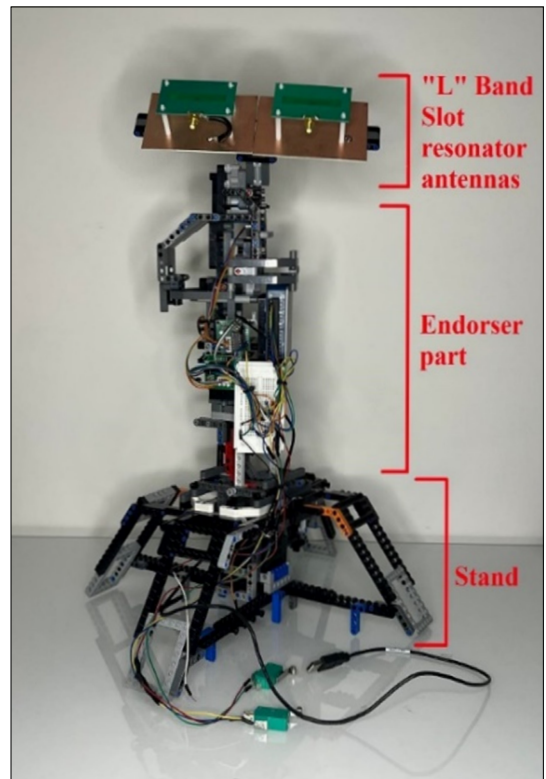


Fig. 19. Designed and assembled antenna rotation system.

an even more durable metal frame, but this significantly increases both the material and, more importantly, the weight factor affecting transportability.

The stepper motor has a specific torque that had to be kept in mind during construction. This problem can be eliminated with more powerful engines, but this also involves increased weight, so it is important to find the right balance. It should be mentioned that if an encoder is built into the system, even more precise motor positioning can be achieved.

A further development option in another direction is a completely waterproof outer covering, thanks to which the construction becomes capable of outdoor operation regardless of the weather. A further development option is a higher-gain, directional phase-controlled antenna system with a preamplifier, which enables more precise measurements.

This research could be of help, in vehicle topics that we have previously researched in the university such as lightweight aircraft and antenna design [27, 28].

Acknowledgement

Special thanks for the support to the University of Debrecen, Faculty of Engineering.

References

- [1] T. I. Erdei, Z. Molnár, N. C. Obinna, G. Husi: *A Novel Design of an Augmented Reality Based Navigation System & Its Industrial Applications*. ACTA IMEKO, 7/1. (2018) 57. https://doi.org/10.21014/acta_imeko.v7i1.528
- [2] T. I. Erdei, N. C. Obinna, Z. Molnar, G. Husi: *Surveillance and Security System in the Building Mechatronics Research Center*. In: 2017 International Conference on Engineering, Technology and Innovation (ICE/ITMC), IEEE, Jun. 2017. 509–512. <https://doi.org/10.1109/ICE.2017.8279928>
- [3] T. I. Erdei, Z. Molnár, G. Husi: *Selecting Equipment and Supplies for Self-Replicating 3D Printer*. ACTA Tech. CORVINIENSIS - Bull. Eng., 2016, [Online]. Available: https://www.researchgate.net/publication/296696614_Selecting_Equipment_and_Supplies_for_Self-Replicating_3D_Printer
- [4] T. P. Kapusi, T. I. Erdei, G. Husi, A. Hajdu: *Application of Deep Learning in the Deployment of an Industrial SCARA Machine for Real-Time Object Detection*. Robotics, 11/4. (2022) 69. <https://doi.org/10.3390/robotics11040069>
- [5] T. I. Erdei, G. Husi: *Singularity Measurement in the Cyber-Physical and Intelligent Robot Systems Laboratory*. Int. Rev. Appl. Sci. Eng., 11/2. (2020) 82–87. <https://doi.org/10.1556/1848.2020.20001>
- [6] T. I. Erdei, R. Krakó, G. Husi: *Design of a Digital Twin Training Centre for an Industrial Robot Arm*. Appl. Sci., 12/17. (2022) 8862. <https://doi.org/10.3390/app12178862>
- [7] A. Masuk, I. Balajti: *Mechatronics Engineering Aspects of VHF Band Antenna Design of Industry 4.0 Applications*. In: 23rd International Radar Symposium (IRS), IEEE, Sep. 2022, 77–82. <https://doi.org/10.23919/IRS54158.2022.9905051>
- [8] D. A. Bradley, N. C. Burd, D. Dawson, A. J. Loader: *Mechatronics Electronics in Products and Processes*. 1st ed. London, Routledge, 2018. <https://doi.org/10.1201/9780203747735>
- [9] U. S. Dixit, M. Hazarika, J. P. Davim: *History of Mechatronics*. In: *A Brief History of Mechanical Engineering*. Springer, 2017. 147–164. https://doi.org/10.1007/978-3-319-42916-8_7
- [10] P. Hariharan, K. Creath: *Basics of Interferometry*. Phys. Today, 46/1. (1993) 75–75. <https://doi.org/10.1063/1.2808787>
- [11] “How Do Interferometric Systems Work,” Renishaw. [Online]. Available: <https://www.renishaw.com/en/how-do-interferometric-systems-work-38612>
- [12] M. M. Wang, J. Zhang: *Machine-Type Communication for Maritime Internet-of-Things*. Springer International Publishing, 2021. <https://doi.org/10.1007/978-3-030-77908-5>
- [13] D. L. Sengupta, T. K. Sarkar: *Maxwell, Hertz, the Maxwellians, and the Early History of Electromagnetic Waves*. IEEE Antennas Propag. Mag., 45/2. (2003) 13–19. <https://doi.org/10.1109/MAP.2003.1203114>
- [14] B. A. Kemp: *Resolution of the Abraham-Minkowski Debate: Implications for the Electromagnetic Wave Theory of Light in Matter*. J. Appl. Phys., 109/11. (2011) 111101. <https://doi.org/10.1063/1.3582151>
- [15] Y. Liu, H. Yang, S. Mao, J. Zhu: *A Multibeam Dual-Band Orthogonal Linearly Polarized Antenna Array for Satellite Communication on the Move*. Int. J. Antennas Propag., 2015. 1–8. <https://doi.org/10.1155/2015/102959>
- [16] D. F. Sievenpiper et al.: *Experimental Validation of Performance Limits and Design Guidelines for Small Antennas*. IEEE Trans. Antennas Propag., 60/1. (2012) 8–19. <https://doi.org/10.1109/TAP.2011.2167938>
- [17] N. I. Miridakis, D. D. Vergados: *A Survey on the Successive Interference Cancellation Performance for Single-Antenna and Multiple-Antenna OFDM Systems*. IEEE Commun. Surv. Tutorials, 15/1. (2013) 312–335. <https://doi.org/10.1109/SURV.2012.030512.00103>
- [18] A. Szántó, S. Hajdu, G. Á. Sziki: *Dynamic Simulation of a Prototype Race Car Driven by Series Wound DC Motor in Matlab-Simulink*. Acta Polytechnica Hungarica, 17/4. (2020) 103–122. <https://doi.org/10.12700/APH.17.4.2020.4.6>

- [19] C. Pollock, J. D. Wale: *Hybrid Stepping Motors and Drives*, Power Eng. J., 5/1. (2001). 5–12. <https://doi.org/10.1049/pe:20010101>.
- [20] G. Á. Sziki, A. Szántó, J. Kiss, G. Juhász, É. Ádámkó: *Measurement System for the Experimental Study and Testing of Electric Motors at the Faculty of Engineering, University of Debrecen*. Appl. Sci., 12/19. (2022) 10095. <https://doi.org/10.3390/app121910095>.
- [21] A. Szántó, É. Ádámkó, G. Juhász, G. Á. Sziki: *Simultaneous measurement of the Moment of Inertia and Braking Torque of Electric Motors Applying Additional Inertia*. Measurement, 204. (2022) 112135. <https://doi.org/10.1016/j.measurement.2022.112135>
- [22] I. Don Labriola P.E. President, QuickSilver Controls, “The Hybrid Servomotor: Stepping up to Closed Loop,” Motion Control Tips. [Online]. <https://www.motioncontroltips.com/the-hybrid-servomotor-stepping-up-to-closed-loop/>
- [23] “28BYJ-48-64 64:1 Stepper Gearmotor,” Solarbotics. [Online]. <https://www.solarbotics.com/product/22310/>
- [24] “NI USB-6002 Low-Cost DAQ USB Device,” NI. [Online]. <https://www.ni.com/docs/en-US/bundle/usb-6002-specs/resource/374371a.pdf>
- [25] T. Istvan Erdei, R. Krako, N. David Peter, G. Husi: *3D CAD Design of KUKA Robot Arm & Integration into AR Environment to Educational Purposes*. In: IEEE 20th International Power Electronics and Motion Control Conference (PEMC), IEEE, Sep. 2022, 590–596. <https://doi.org/10.1109/PEMC51159.2022.9962864>
- [26] “LEGO® Digital Designer,” BrickLink Studio. [Online]. Available: <https://www.bricklink.com/v3/studio/download.page>
- [27] A. Masuk, H. Géza: *Aero Graphene in Modern Aircraft & UAV*. Recent Innovations in Mechatronics, 9/1. (2022). <https://doi.org/10.17667/riim.2022.1/4>.
- [28] A. Masuk, H. Géza: *Uses of Aero Graphene and CNT in Modern Aircraft*. AIP Conference Proceedings, 2941/1. (2023) 020029. <https://doi.org/10.1063/5.0181354>.



ONE HUNDRED YEARS OF DRY FIRE EXTINGUISHER EQUIPMENT

József GÁTI,¹ Krisztina NÉMETHY,² János KUTI³

¹ Obuda University, Banki Donat Faculty of Mechanical and Safety Engineering, Budapest, Hungary, gati@uni-obuda.hu

² IBS, Budapest, Hungary, knemethy@ibs-b.hu

³ Obuda University, Banki Donat Faculty of Mechanical and Safety Engineering, Budapest, Hungary, kuti@uni-obuda.hu

Abstract

In the early 19th century, the level of Hungarian industry lagged behind that of developed states. As a result of rapid development, by the end of the 19th century and the first decades of the 20th century, the domestic technical and natural sciences showcased significant successes through the outstanding activities of the defining industrialists and engineers of the era.

The rapid urbanization posed new challenges in the operation of large cities, ensuring security, and fire protection. Responses to these challenges could only be provided by professionals who were excellently prepared with both technical and firefighting knowledge, such as Kornél Szilvay, who dedicated his entire life to improving the efficiency of firefighting.

Keywords: *Kornél Szilvay, dry extinguishing, water damage-free extinguishing of fire.*

1. The beginning of a firefighter's career

Kornél Szilvay was born on July 25, 1890, in Budapest, as the child of Antal Szilvay and Anna Greff. After completing his four years in elementary school, his interest turned towards the technical field. He continued his studies at the predecessor of the present-day Óbuda University, the Budapest Hungarian Royal State Upper Industrial School. Following the successful completion of the preparatory class, he obtained his certification in the mechanical engineering department after three years.

During his studies, the director of the Upper Industrial School, Károly Hegedűs, initiated the expansion of the students' firefighting knowledge with the school authorities. A "firefighting training course" was organized, and „it was approved by the high decree of the minister, as stated in the document number 105.684./IV. B. from 1908". [1]

By completing the specialized course, Kornél Szilvay committed himself for life to the cause of firefighting and fire protection. After his studies, he began his career at the Schlick Factory in Budapest, where his father also worked. He became

a factory firefighter and joined the Budapest Volunteer Fire Association in the same year. From 2012, he served as a section commander, and from 2013, he performed assistant officer duties and handled storage tasks. Recognizing the significant role of reliable firefighting equipment and procedures alongside the personal preparedness and courage of firefighters, he consciously started modernizing them to increase the efficiency of firefighting. On February 1, 1914, he entered the service of Budapest as a professional firefighter.

2. The Patent of the Dry Fire Extinguishing Apparatus

In the early 1920s, Szilvay shifted his focus to replacing water-based firefighting techniques based on water application, aiming to reduce or avoid water damage. A hundred years ago, on December 29, 1923, as a result of his experiments related to dry firefighting, he patented the principle of gas and powder extinguishing firefighting apparatus. The patent description summarized the essence of the innovation as follows: "The essence of the method according to the invention

lies in first cooling the exhaust gases of an internal combustion engine, then compressing them to the necessary pressure with the help of a compressor, and finally blowing the extinguishing powder, known from the powder container, to the location of the fire with the thus compressed gases." [2]

The operational principle is recorded in the description as follows (Figure 1): „In the attached drawing, a schematic representation of a firefighting device operating according to this method is provided. (1) indicates the powder container from which a (2) conveyor screw transports the extinguishing powder to the (3) nozzle. (4) denotes an internal combustion engine, and its exhaust gases exit through the (5) tube. At (6) on the (5) tube, it converges into a (7) tubular cooler, where the exhaust gases are cooled as they pass through, leaving the cooler through the (8) tube after being cooled. The (8) tube converges into a (9) rotary compressor, which is driven by the (10) shaft of the (4) engine; the same shaft also drives the (2) conveyor screw with the help of the (11) belt drive. The (9) compressor compresses the gases sucked in from the (8) tube to the required pressure and delivers them to the (3) nozzle through the (12) casing, where the pressurized gas blows the supplied extinguishing powder into the (13) hose attachment, to which the hose required for firefighting can be connected in a known manner.” [2]

The production of the experimental apparatus began in 1926. The first dry firefighting vehicle, equipped with a 60 HP internal combustion engine, built on a chassis with a load capacity of 5 tons, and featuring a compressor capable of transmitting 6 m³/min of extinguishing gas, was manufactured at the MÁVAG Locomotive and Machine Factory. It had a 2 m³ wooden powder container initially, but as the wooden container proved ineffective, further experiments continued with a steel storage vessel (Figure 2).

In the preparation of the prototype, the constructor was István Horthy from Nagybánya; he was the former head of one of the design departments at MÁVAG. The first dry firefighting vehicle was presented and handed over during a demonstration on December 27, 1927, at the barracks of the Budapest Fire Department (Figure 3).

On January 22, 1928, Prime Minister Count István Bethlen observed Szilvay's newly employed powder extinguisher in action during firefighting. A few days later, Dr. Ferenc Ripka, the Mayor of Budapest, witnessed the operating equipment during a practical exercise, and on both occasions, it functioned excellently.

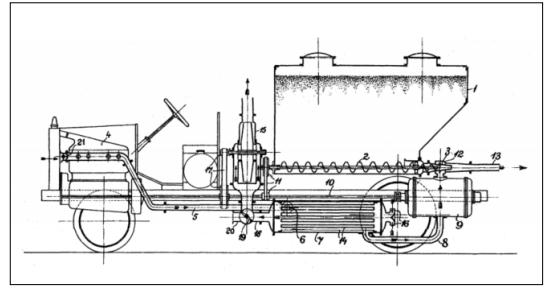


Fig. 1. The conceptual outline of the dry fire extinguishing apparatus from the patent description's accompanying drawings [2]



Fig. 2. The production of the experimental dry firefighting equipment [3]



Fig. 3. Presentation of the horizontal cylindrical dry fire extinguisher at the Kun Street barracks [4]

The first practical deployment of the dry firefighting machine took place on March 1, 1928, in Budapest, during a fire at the art studio of painter Miklós Mihalovits. According to the report in *Esti Kurir*, "...Chief Officer Szilvay decided not to attempt to extinguish the fire with water, which would soak the ceiling and destroy the paintings, but with a new type of firefighting device, his invention. This extinguishing device uses powder and a gas mixture. The chief officer personally put

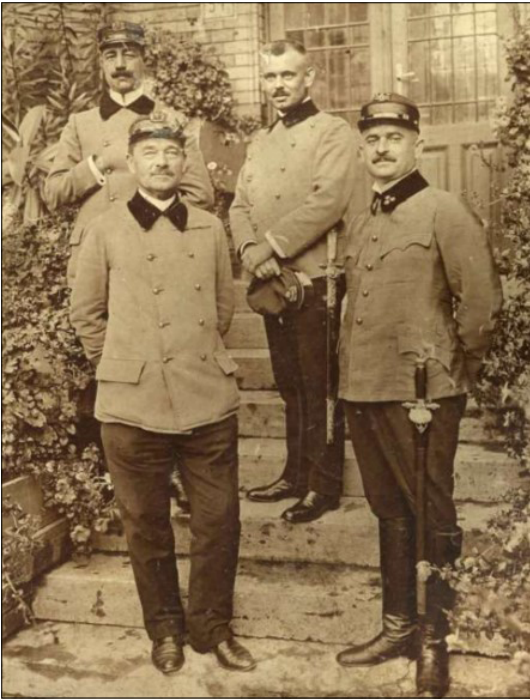


Fig. 4. A group of professional firefighters from the capital, Szilvay second from the right with an uncovered head [5]

this device into operation, marking its first appearance. The result perfectly justifies the hopes placed in the device because within twenty minutes, they managed to localize the extensive fire without any harm to the accumulated artistic objects.” [6]

The highest international recognition came at the Paris International Firefighting Exhibition,

where, according to contemporary reports, “Szilvay Kornél, the chief firefighter from Budapest, attracted great attention with his invention, the dry firefighting machine.” (Figure 5) „At the exhibition opening, the Hungarian invention was presented to the French Minister of the Interior, Tardieu.” [7]

At the exhibition, the dry extinguisher presented on the Mávag-Mercedes-Benz chassis was capable of extinguishing with neutral gas, powder, water, and water mist, carbon dioxide snow and foam, as well being suitable for combined extinguishing with powder, gas, and water mist. The equipment, referred to in professional circles as a “universal extinguisher,” was equipped with a vertical cylinder powder container instead of the previous horizontal one.

In early July, President Paul Doumer of the French Republic also visited the Hungarian section of the Paris Firefighter Exhibition, where a perfected dry extinguisher was showcased. “In response to his inquiries, brave Chief Engineer István Horthy of Nagybánya provided detailed explanations.” At the request of a colonel from the Paris Fire Department, a firefighting demonstration was also held. “In the demonstration house of the exhibition, cables saturated with high and low voltage electricity were laid down and then ignited. Engineer István Horthy and the Parisian firefighters at his disposal began extinguishing the fire... they quickly suppressed the burning telephone cables. The Parisian fire officers, as well as foreign firefighters who witnessed the firefighting work, expressed their utmost admiration...” reported the *Magyarság* newspaper on July 14, 1931. [9] The new equipment aroused the interest of not only

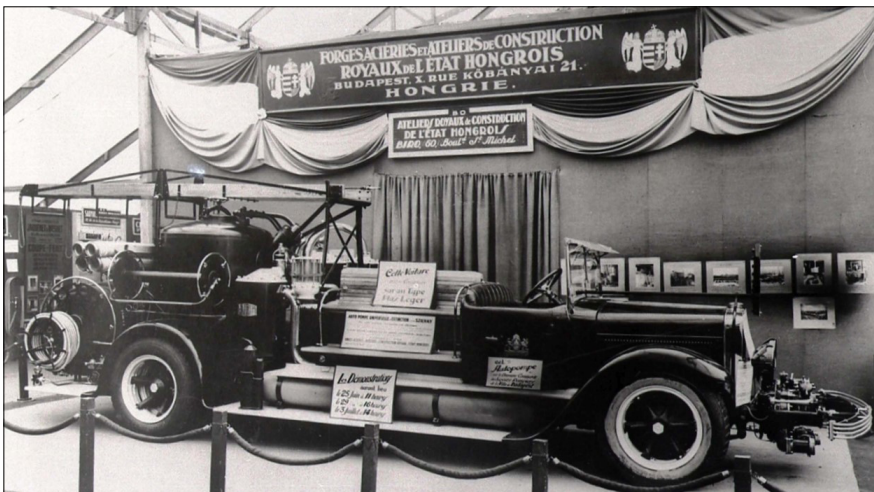


Fig. 5. The Szilvay-designed dry firefighting machine at the Paris International Firefighting Exhibition [8]

French and Austrian experts but also American and Canadian firefighters.

In 1929, the dry extinguisher was used in 20 cases to carry out significant firefighting operations in Budapest without causing substantial water damage. Experience showed that dry extinguishing proved to be most successful in extinguishing fires that occurred in enclosed spaces (out of 20 fire incidents, 14 were business or warehouse fires). It often happened that when entering a closed space, such as breaking through the shutters of a shop, fresh air rushed in, causing the fire to flare up and engulf the surroundings in flames. Recognizing this, Szilvay implemented small openings for introducing the extinguishing agent without breaking the closure, which allowed the introduction of the extinguishing gas without destroying the closure and without the inflow of fresh air.

With the widespread use of electricity, fire incidents involving electrical equipment and distribution units became increasingly common, where traditional water-based firefighting methods were not applicable. On June 16, 1932, at the Kárpát Street site of the Hungarian Transdanubian Electricity Company in Budapest, a 20,000 KVA oil-cooled transformer caught fire. *"The fire of the outdoor transformer was successfully extinguished with a powder jet without the need to power down the two adjacent transformers."* [10]

Szilvay further developed the procedure for extinguishing fires in enclosed-space transformers as well. His patents extensively discussed the introduction openings, which effectively enabled the extinguishing of fires in closed spaces containing transformers and switchgear. The inventor's patents for effectively extinguishing fires in closed spaces included the following:



Fig. 6. The installation of stationary tank dry extinguishers at Mávag between 1939 and 1940 [11]

- Procedure and apparatus for extinguishing fires by dry means (January 24, 1932).
- Apparatus for extinguishing fires occurring in rooms (November 29, 1934).
- Dry extinguishing apparatus (December 4, 1934).
- Dry extinguishing apparatus for fires in large rooms and method for maintaining the dry extinguisher (January 15, 1941).
- Apparatus for extinguishing fires in enclosed spaces (May 9, 1942).

The experiences showed that *"the vehicle engine often does not provide a sufficient quantity and quality of gas without carbon dioxide, because the engine is not sufficiently loaded; moreover, the gas quantity required to extinguish large fires cannot even be produced by the engines in use, even under full load. To overcome these disadvantages, according to the invention, a compressor is driven by the engine, which compresses clean air and pushes it into an oil burner, from which the resulting combustion products can be used for extinguishing..."* - wrote the inventor in his patent registered on December 4, 1934, titled *"Dry extinguishing apparatus"*. [12]

Despite the continuous modernization of the dry extinguishing system, the quantity of exhaust gases from internal combustion engines at the time proved insufficient for extinguishing fires in large-sized spaces.

Szilvay's further developments aimed to increase the amount of gas emitted per minute. The opportunity to design a device capable of producing 100 m³ of extinguishing gas per minute arose at the Ganz és Társa a Villamossági Gép-, Vagon- és Hajógyár Rt. using the Jendrassik-type gas turbine. The mechanical equipment was completed in 1951, followed by the superstructure in 1953, and then the trial operation began. However, due to Szilvay's death on September 8, 1957, the process was interrupted.

3. Reminiscing

Throughout his career, Kornél Szilvay deemed it important to actively participate in firefighting efforts. For 35 years, he responded to fire incidents, with one occurring approximately every 17th hour of his service. With a high level of professionalism and selflessness, he fulfilled his duties as both a firefighter and an innovator.

In his 1982 article, retired Lieutenant Colonel Rezső Tarján, a mechanical engineer and former firefighter, praised Szilvay's role, stating, *"As a firefighter officer, he estimated that he led firefight-*



Fig. 7. The Kornél Szilvay Commemorative Coin by HNB [14]

ing efforts in about sixteen thousand fires. For instance, he directed the extinguishing of the Basilica dome fire on June 20, 1947. He took proactive measures to protect the valuable frescoes, and despite the large quantity of water used during the fire-fighting, there was no flooding or water damage. Using a 400 liters per minute small motor pump, he drained water accumulated in the recesses of the dome pillars and used the streams to protect the Basilica's valuable parts from burning." [13]

On February 1, 1955, he announced his final patent titled "Dry Extinguishing Procedure", making him the holder of 39 patents, the majority of which were directly aimed at improving firefighting efficiency.

In recognition of his life and professional career, President Árpád Göncz posthumously promoted him to the rank of Lieutenant General in 1993. In May 1994, a plaque was unveiled in honor of Kornél Szilvay, the firefighter-inventor, at the headquarters of the Budapest Fire Department. The Central Fire Protection Department of the Mechanical Engineering Scientific Society established the Kornél Szilvay Memorial Medal in 1995.

In 2015, on the occasion of his 125th birthday anniversary, the Hungarian National Bank issued a commemorative coin with a face value of 2000 HUF under the name "Kornél Szilvay." (7. ábra).

In 2022, the Bánki Donát Faculty of Mechanical and Safety Engineering at Óbuda University launched the "Kornél Szilvay Fire Protection Conference" series in honor of the outstanding student of its predecessor institution. This initiative is part of the Hungarian Science Festival event series. [15]

References

- [1] Hegedűs Károly: *Értesítő a Budapesti M. K. Átlami Felső Ipariskola harmincadik tanévérlől, 1908–1909.*, Budapest, PÁTRIA Irodalmi Vállalat és Nyomdai Részvény-Társ. Nyomása, 1909.
- [2] Eljárás és készülék tűz oltására, Szilvay Kornél tűzoltófőtiszt, Budapest, Szabadság, 1923. 12. 29. 88979. szám.
- [3] Katasztrófavédelem Központi Múzeuma archívuma, 063. kép.
- [4] Katasztrófavédelem Központi Múzeuma archívuma, Szilvay_fekvochengeres_oltogep.
- [5] Katasztrófavédelem Központi Múzeuma archívuma, Szilvay Kornél, 3875. kép.
- [6] *Esti Kurir*, 6/50. (1928) 11.
- [7] *Képes Pesti Hírlap*, 50/186. (1928).
- [8] Katasztrófavédelem Központi Múzeuma archívuma, Szilvay_oltogep_Parizs.
- [9] *Magyarság*, 12/157 (1931).
- [10] *Magyar Tűzoltó*, 13/8 (1961).
- [11] Katasztrófavédelem Központi Múzeuma archívuma, 341. kép.
- [12] Szárazoltó-berendezés, Szilvay Kornél tűzoltó főtiszt, Szabadság, Magyar Királyi Szabadalmi Bíróság, Budapest, 11275/1934.
- [13] Tarján Rezső: *A tűzoltás vízkára.* Műszaki Élet, 25. 1982.
- [14] A 2015. évi Szilvay Kornél-émlékerme. <https://penzvero.hu/termek/2015-evi-szilvay-kornel-szinesfem-emlekerme-pp/>
- [15] Szilvay Kornél tűzvédelmi konferencia, Óbudai Egyetem Bánki Donát Gépész és Biztonságtechnikai Mérnöki Kar, 2022. november 15. <https://bgk.uni-obuda.hu/tuzvedelmi-konferencia-2022/q>



SIMULATION OF THE VECTOR CONTROLLED PMSYM DRIVE BASED ON SIMPLIFIED MODELING STRUCTURES

Mária IMECS,¹ János FERENCZ,² András KELEMEN³

¹ Technical University of Cluj-Napoca, Doctoral School, Faculty of Electrical Engineering, Cluj-Napoca, Romania, Maria.Imecs@emd.utcluj.ro

² Technical University of Cluj-Napoca, Doctoral School, Faculty of Electrical Engineering, Cluj-Napoca, Romania, janos.ferencz.phd.project@gmail.com

³ Sapientia EHungarian University of Transylvania, Faculty of Technical and Human Sciences, Department of Electrical Engineering, Târgu Mureş, Romania, kandras@ms.sapientia.ro

Abstract

The paper presents the simulation results of the simplified static (St) and dynamic (Dy) simulation structures (SimS), with voltage (U) and frequency (f) input, all of them based on a simplified mathematical model (MaMo) of the PM synchronous machine (SyM) corresponding to the operation mode with stator current vector perpendicular to the PM flux (CVpPMF). These results are compared with those simulated with vectorial speed controlled (VC) SimS-s where the longitudinal armature reaction is cancelled by means of two-phase current controllers in two different conditions: when the motor is fed by sine-wave voltages, and when it is connected to a PWM-inverter. By means of simulation of the St- and Dy_SimS-s the motor parameter identification calculations are verified, while the compatibility of the MATLAB/Simulink® motor block with the applied MaMo, required for the implementation of the vector control, is also verified using the VC-Sim-s.

Keywords: PM synchronous motor, vector control, mathematical modelling, simulation structures.

1. Introduction

The permanent magnet (PM) synchronous type machines belong to the most commonly used electrical machines besides the asynchronous motors. These can have sinusoidal or trapezoidal flux distribution of the magnetic field (DMF) in the air gap. The classical synchronous machines (SyM) have sinusoidal distribution DMF and those with trapezoidal DMF are considered “synchronous type” motors like the brushless direct current machines (BLDC), the conventional stepper motors and the motors with pole number ratio (4/3, 3/4, 5/2, 5/3, etc) different from 1, where the stator and rotor pole-numbers are not equal. The PMSyM-s are widely used as motors in the domain of electrical drives and as generators for energy production in wind turbine systems. This paper deals with the PMSyM with sinusoidal DMF whose mathematical model (MaMo) is based on the Park-theory.

2. The mathematical model of the PM synchronous machines

In **Figure 1** is presented the schematic structure of a one pole pair ($z_p = 1$) PMSyM, where θ is the rotor position with respect to the d (real) axis of the reference frame fixed to the stator. This coincides with the a_s stator phase magnetizing direction and it is expressed as an electrical angle.

According to the general Park-theory the two-phase MaMo of the SyM-s with sinewave DMF is expressed in the reference frame fixed to the rotor.

The $d\theta$ – $q\theta$ axes of the coordinate system (CooSy) correspond to the symmetry axes of the PM rotor **[1, 2]**, thus the orientation of the reference frame can be named PM-field orientation.

2.1. The general dynamic mathematical model of the PM synchronous machines

The general equations of the PMSyM without damping circuits can be deduced from the

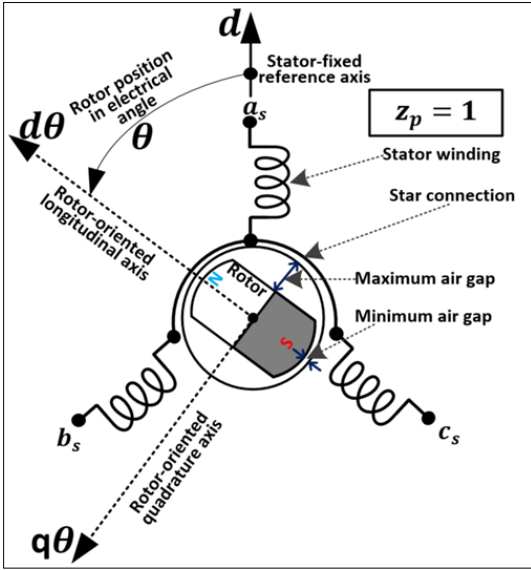


Fig. 1. Structural principle diagram of the PMSyM with $z_p = 1$ pole pair.

original Park-model by neglecting the rotor circuits and by replacing the magnetic flux of the exciting winding with the PM flux [3].

The voltage equation of the armature (stator) written with space phasors is

$$\underline{u}_{s\theta} = R_s \underline{i}_{s\theta} + \frac{d\Psi_{s\theta}}{dt} + j\omega \Psi_{s\theta}, \quad (1)$$

where $\underline{u}_{s\theta}$, $\underline{i}_{s\theta}$, and $\Psi_{s\theta}$ are the space phasors of the armature voltage, current and armature flux, respectively, in rotor-oriented coordinate system, R_s is the stator resistance, ω is the electrical angular speed of the rotor

$$\omega = \frac{d\theta}{dt} \quad (2)$$

and θ is the angular position of the rotor as is shown in **Figure 1**.

The armature resultant flux:

$$\Psi_{s\theta} = \Psi_{PM} + \Psi_{ss\theta}, \quad (3)$$

where Ψ_{PM} is the PM flux, the direction of which coincides with the real axis of the complex plane i.e. with the rotor-oriented $d\theta$ direct axis and $\Psi_{ss\theta}$ is the armature reaction flux (ARF). This one can be written with the two-phase components (2PhCo) of the stator current as follows:

$$\Psi_{ss\theta} = L_{sd} i_{sd\theta} + jL_{sq} i_{sq\theta}, \quad (4)$$

where L_{sd} and L_{sq} are the longitudinal and quadrature three-phase inductances.

The dynamic torque in the motion equation is:

$$J_{Eq} \frac{d\omega_m}{dt} = m_e - m_L, \quad (5)$$

where J_{Eq} is the equivalent moment of inertia, ω_m the mechanical angular speed, m_e the electromagnetic torque (EMT) and m_L load torque.

The mechanical angular speed and the f_s frequency are proportional with the speed n measured in RPM („revolution per minute”). In the identification procedure of the motor parameters the below expressions are useful:

$$\omega_m = \frac{\omega}{z_p} = \frac{\pi n}{30}, \quad (6)$$

$$f_s = z_p \frac{n}{60}, \quad (7)$$

where z_p is the pole-pair number.

The electromagnetic torque expressed with the two-phase components is [1–3]:

$$m_e = K_{M1} z_p (\Psi_{sd\theta} i_{sq\theta} - \Psi_{sq\theta} i_{sd\theta}), \quad (8.1)$$

If the ARF components are substituted in the function of the current components, then there are put in evidence the two synchronous torques of different provenience, attributable to the PM and the variable reluctance:

$$m_e = K_{M1} z_p (\Psi_{PM} i_{sq\theta} + 2\Delta L i_{sd\theta} i_{sq\theta}); \quad (8.2)$$

where the torque coefficient is $K_{M1} = 3/2$, if the variables correspond to amplitude of the instantaneous values.

The difference $2\Delta L = L_{sd} - L_{sq}$ expresses the effect of the variable reluctance. Its value in conventional machines is positive, but on the other hand many of the recently produced motors have negative reluctance torque which diminishes the main torque produced by the PM.

2.2. Steady state mathematical model of the PM synchronous motors

In electromagnetic steady state (StSt), when the current and the flux amplitude are constant, from the voltage equations (1) the derivative of the flux is eliminated, consequently the voltage equations are simplified, but the flux equations are not changed. These equations with two-phase components are:

– the armature voltage

$$\begin{cases} u_{sd\theta} = R_s i_{sd\theta} - \omega \Psi_{sq\theta}; \\ u_{sq\theta} = R_s i_{sq\theta} + \omega \Psi_{sd\theta}; \end{cases} \quad (9)$$

– the armature resultant flux

$$\begin{cases} \Psi_{sd\theta} = \Psi_{ssd\theta} + \Psi_{PM}; \\ \Psi_{sq\theta} = \Psi_{ssq\theta}; \end{cases} \quad (10)$$

– the armature reaction flux

$$\begin{cases} \Psi_{ssd\theta} = L_{sd} i_{sd\theta}; \\ \Psi_{ssq\theta} = L_{sq} i_{sq\theta}. \end{cases} \quad (11)$$

In electromechanic StSt, when the speed is also constant, in the motion equation (5), the derivative of the speed results zero and the torque equation become:

$$m_e = m_L, \quad (12)$$

where the EMT results from (8.1) or (8.2).

In **Figure 2** is presented a version of the general StSt simulation structure created based on the (6) - (12) equations.

This variant is useful for checking the rated data (operation point) of the motor. Depending on the purpose of the modelling, there various simulation structures may be developed by swapping between one or more inputs and outputs.

Usually, the sinusoidal operation is calculated with RMS (*Root Mean Square*) values. In this case in expressions (8.1) and (8.2) the torque coefficient is $K_{MI} = 3$ [1, 3].

3. The rated data of the PMSyM

The type of the motor is SIMOTICS S-1FL6/ Siemens AG (DE-97616 Bad Neustadt) [7].

The motor rated data written on the name plate are:

- shaft torque $M_{tN} = 0.64$ Nm;
- shaft power $P_{tN} = 200$ W;
- revolutions per minute $n_N = 3000$ RPM;
- line current rms value $I_{vN}^{ef} = I_{sN}^{ef} = 1.4$ A (it is equal to the phase current).

Additional data from the motor manual:

- line voltage rms value $U_{vN}^{ef} = \sqrt{3} U_{sN}^{ef} = 111$ V, consequently the phase voltage $U_{sN}^{ef} = 64$ V;
- the rotor moment of inertia $J_r = 0.214 \cdot 10^{-4}$ kg m²;
- the load moment of inertia may be maximum 30 times the J_r [7].

Measured parameters:

- armature resistance $R_s = 5.33$ Ω;
- longitudinal inductance $L_{sd} = 10.19$ mH;
- quadrature inductance $L_{sq} = 11.17$ mH;
- pole-pair number $z_p = 4$.

Calculated rated data:

- $f_{sN} = 200$ Hz, supply frequency;
- $M_{eN} = 0.731$ Nm, electromagnetic torque (EMT);
- $\cos\varphi_N = 0.95$ power factor;
- efficiency $\eta_N = 77.5\%$;
- $\Psi_{PM}^{Max} = 0.0615$ Wb, magnitude of the identified PM flux.

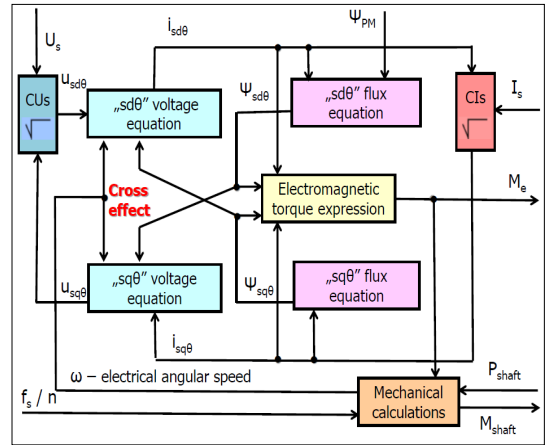


Fig. 2. The general steady state simulation structure of the PMSyM.

The measured parameters and the calculated data can be checked with the St_SimS from **Figure 2** for the rated operation point for the input rated values (voltage, current and frequency).

4. The control principle with the current vector perpendicular to the PM flux (CVpPMF)

The PMSyM-s with sinusoidal DMF have four fundamental control procedures [4–6].

According to the best-known and most applied control principle the space phasor of the armature current is constrained to be perpendicular to the rotor longitudinal (direct) magnetic axis, i.e. to the PM-flux vector. In this case the two-phase components of the current space phasor have particular values: the direct component is zero, and the quadrature one is equal to the module of the current vector:

$$\begin{cases} i_{sd\theta} = 0; \\ i_{sq\theta} = i_s. \end{cases} \quad (13)$$

Based on (13) the longitudinal armature reaction (ArRe) flux $\Psi_{ssd\theta}$ is also zero. In this situation the resultant armature flux cannot be controlled to a constant value because the quadrature ArRe flux $\Psi_{ssq\theta}$ depends on the current and is determined by the mechanical load. Another disadvantage is the inductive character of the current because the motor with CVpPMF cannot operate at unity power factor. However, it has the advantage that the electromagnetic torque is produced with the minimum current value. On the other hand, for some new types of variable reluctance PM motors, with

$L_{sd} < L_{sq}$ (valid also for the above presented Siemens motor), the negative reluctance torque, that diminishes the PM torque, is cancelled due to the absence of the longitudinal ArRe flux.

4.1. Steady state phasor diagram with the CVpPMF

In **Figure 3** is presented the phasor diagram of the motor operating in steady state with the CVpPMF based on equations (9) - (11). This phasor diagram is valid for space phasors and at the same time for time phasors. It is also valid if the speed is variable in electromagnetic steady state, when the rms value of the current and fluxes is constant, because the diagram is independent of the variation of the speed in braking or acceleration operation of the motor.

4.2. Mathematical models with the CVpPMF

Considering the (13) condition, if the current vector ideally can be kept permanently perpendicular to the PM flux, in both dynamic and steady state operation, it leads to the simplified mathematical model of the PMSyM. Thus, the simplified simulation structures of the vector controlled PMSyM can be synthesized.

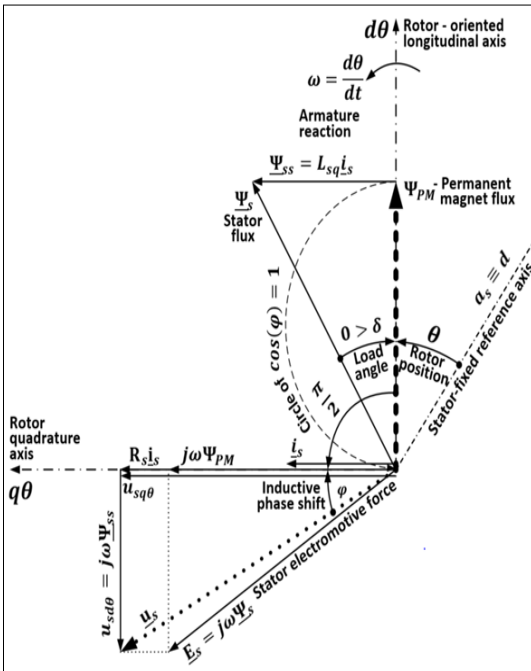


Fig. 3. Electromagnetic steady state phasor diagram with the CVpPMF in $d\theta - q\theta$ rotor-oriented synchronous rotating coordinate system.

4.2.1. Steady state simplified mathematical model with the CVpPMF

Considering (13) and based on the (8) - (11) StSt equations, the simplified voltage, flux and torque expressions are the followings:

$$\begin{cases} \Psi_{ssd\theta} = 0; \\ \Psi_{ssq\theta} = \Psi_{ss} = L_{sq} i_s; \end{cases} \quad (14)$$

$$\begin{cases} \Psi_{sd\theta} = \Psi_{PM}; \\ \Psi_{sq\theta} = \Psi_{ssq\theta}; \end{cases} \quad (15)$$

$$\begin{cases} u_{sd\theta} = -\omega L_{sq} i_s; \\ u_{sq\theta} = R_s i_s + \omega \Psi_{PM}; \end{cases} \quad (16)$$

$$m_e = K_{M1} z_p \Psi_{PM} i_s, \quad (17)$$

and to these above (12) must be added, too.

4.2.2. Dynamic state simplified mathematical model with the CVpPMF

Considering (13) and based on the (1) - (8) general dynamic equations written with two-phase components, the simplified dynamic model results as follows:

$$\begin{cases} u_{sd\theta} = -\omega \Psi_{ss} = -\omega L_{sq} i_s; \\ u_{sq\theta} = R_s i_s + \omega \Psi_{PM} + L_{sq} \frac{di_s}{dt}, \end{cases} \quad (18)$$

and to these above the (5) motion equation, the (17) electromagnetic torque, and the (14) and (15) flux expressions must be added. In (18) the terms containing ω are the rotational electro-motive force (EMF) two-phase components while the term containing the current derivative is the self induction voltage.

5. Vector controlled structures of the PMSyM drive

Based on the above presented MaMo-s there result the simplified simulation structures of the PMSyM drives. According to (5) and (12) the load torque contains the sum of all friction torques between the rotor and the load.

5.1. Simplified simulation structures without controllers

Modelling a simulation structure of the motor together with the whole control system, may result in more errors. In order to avoid that in the first step it is recommended to use simplified simulation structures without controllers considering ideally the perpendicularity of the current vector to the PM flux, based on the MaMo-s in steady state and dynamic operation modes presented in subsection 4.2.

5.1.1. Simplified static simulation structures (St_SimS) in steady state

According to the MaMo presented in paragraph 4.2.1 there is the possibility to create two different St_SimS-s depending on the input variables which beside the load torque may be the voltage or the frequency. The two St_SimS-s are presented in **Figures 4** and **5**, respectively. The structure with frequency (St_SimS_f) input is presented in **Figure 4** where the voltage is the output.

In **Figure 5** the presented simulation structure (St_SimS_U) has voltage and torque inputs and current and frequency outputs, respectively.

The similarity of both St_SimS-s consists in the load torque (equal to the EMT) input and the armature current output, which is proportional with the torque likewise the physical phenomena in the motor. In the structure St_SimS-s in steady state the calculations usually are made with rms values and in this case the torque coefficient $K_M = 3$, as it is written in **Figures 4** and **5**.

5.1.2. Simplified dynamic simulation structures (Dy_SimS)

There are two different Dy_SimS-s similarly to the previous subsection. These are based on the MaMo from paragraph 4.2.2 and differ in input, that is the voltage or the frequency beside the load torque. These St_SimS-s are presented in **Figure 6** and **7**, respectively.

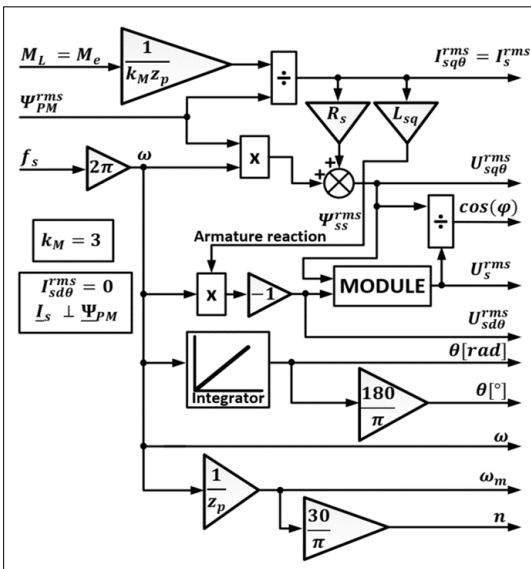


Fig. 4. Static simulation structure (St_SimS_f) block diagram of the PMSyM with the CVpPMF with frequency and torque inputs, and current and voltage outputs, respectively [8].

The Dy_SimS-s contain only two derivatives, of the speed and of the armature current, the last one being equal with the torque producing (active) current component.

Due to the fact that in the Dy_SimS_U structure the voltage is the input, it contains integration blocks, as usually in the motor type MaMo-s. In the Dy_SimS_f structure, where the frequency is the input, instead of integration there appear derivative blocks and the voltage is an output, as in the case of generative type MaMo-s.

In the dynamic simulation structures the calculations usually are made with the amplitude of the variables, as in the classical Park models, consequently the torque coefficient $K_M = 3/2$, as it is written in **Figure 6** and **7**.

5.2. Simulation structures with controllers

The vector control structure which is suitable for implementation is presented in **Figure 8**, where the perpendicularity of the current vector to the PM flux is provided by means of cancelling the longitudinal ArRe, according to (13) controlling the current component i_{sd0} to zero value. Besides that the speed is controlled by a cascade control structure by means of the active quadrature current component i_{sq0} , which in steady state is equal to the modulus of the i_s armature current.

The actuator is a carrier-wave controlled pulse-width modulated (PWM) voltage-source

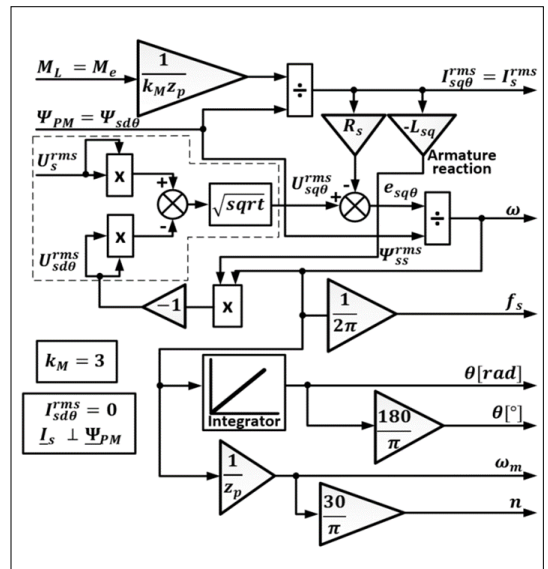


Fig. 5. Static simulation structure (St_SimS_U) block diagram of the PMSyM with the CVpPMF, with voltage and torque inputs and current and frequency outputs, respectively.

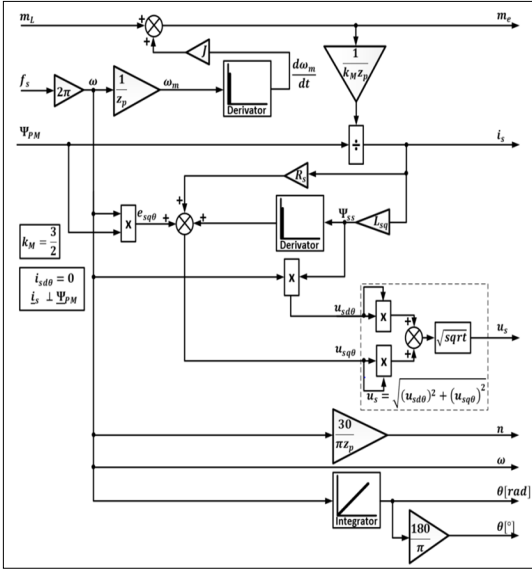


Fig. 6. Dynamic simulation structure (Dy_SimS_f) block diagram of the PMSyM with the CVpPMF with frequency and torque inputs and current and voltage outputs, respectively.

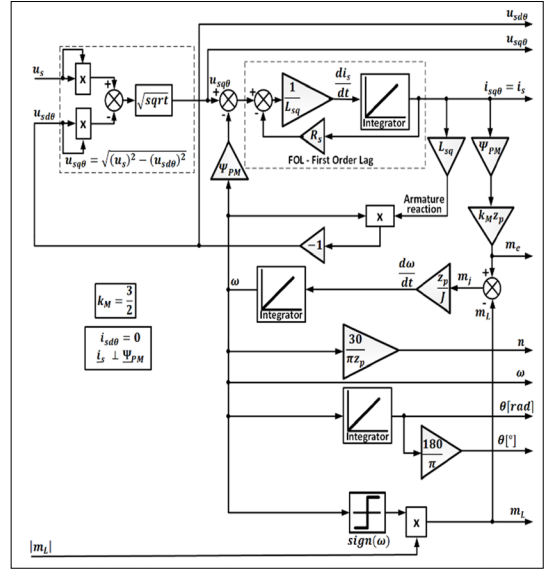


Fig. 7. Dynamic simulation structure (Dy_SimS_U) block diagram of the PMSyM with the CVpPMF with voltage and torque inputs and current and frequency outputs, respectively [8].

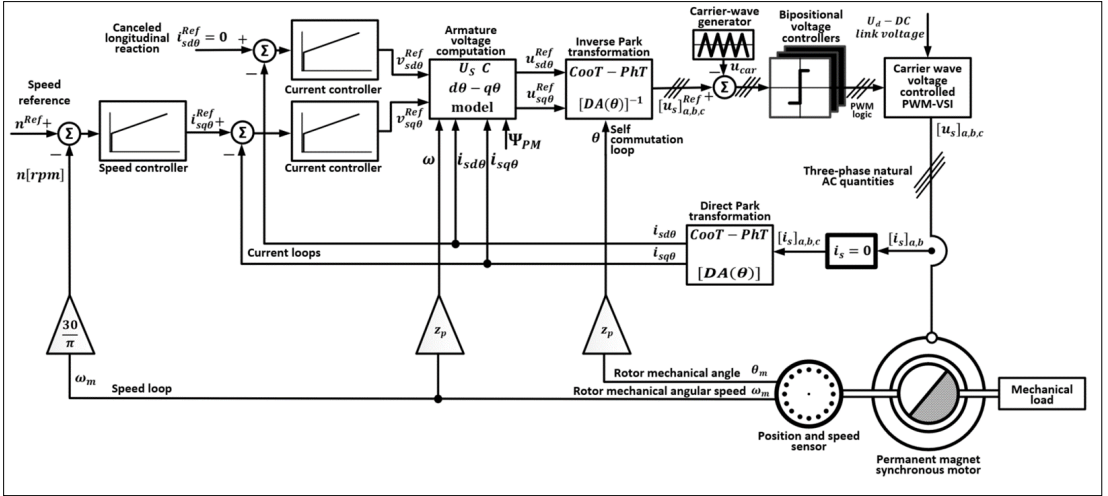


Fig. 8. Vector control structure of the synchronous motor drive fed by carrier wave PWM controlled voltage-source inverter (VSI) with the current vector perpendicular to the PM flux.

inverter (VSI), which practically is a three-phase IGBT bridge DC-AC converter. The two-phase components of the armature current are imposed as reference values. The active component reference value is generated by the speed controller. Because the PWM procedure is of voltage-controlled type, it needs voltage references. That is why the $U_s C$ block is needed, which is compiled upon the PMSyM MaMo, as follows:

$$\begin{cases} u_{sd0}^{ref} = v_{sd0}^{ref} - \omega L_{sq} i_{sq0}^{ref}; \\ u_{sq0}^{ref} = v_{sq0}^{ref} + \omega L_{sd} i_{sd0}^{ref} + \omega \Psi_{PM}, \end{cases} \quad (19)$$

where the speed ω and the current components result as feedback.

The two control variables generated by the current controllers are determined based on the scalar equations derived from (1), as follows:

$$\begin{cases} v_{sd\theta}^{Ref} = R_s i_{sq\theta} + L_{sd} \frac{di_{sd\theta}}{dt}; \\ v_{sq\theta}^{Ref} = R_s i_{sq\theta} + L_{sq} \frac{di_{sq\theta}}{dt}. \end{cases} \quad (20)$$

In this vector control structure, the PMSyM is simulated using the MATLAB-Simulink® library model of the 3-phase motor, with the MaMo presented in **Figure 9**.

The internal PMSM block is based on (1) - (8) general equations written with rotor-oriented, i.e. PM-field-oriented two-phase components. It is connected to the external three-phase system (inverter and PWM control unit) with the direct and reverse Park transformation blocks (CooT-PhT). In fact the Park-transformation is composed of two elementary transformations, the so-called „3/2” Clarke phase transformation (PhT) and the conventional coordinate transformation (CooT).

The matrix operator of the Park-transformation results by combining the two elementary matrix operators and it results:

$$[DA(\theta)] = \frac{2}{3} \begin{bmatrix} \cos(\theta) & \cos\left(\theta - \frac{2\pi}{3}\right) & \cos\left(\theta + \frac{2\pi}{3}\right) \\ -\sin(\theta) & -\sin\left(\theta - \frac{2\pi}{3}\right) & -\sin\left(\theta + \frac{2\pi}{3}\right) \\ \frac{1}{2} & \frac{1}{2} & \frac{1}{2} \end{bmatrix}. \quad (21)$$

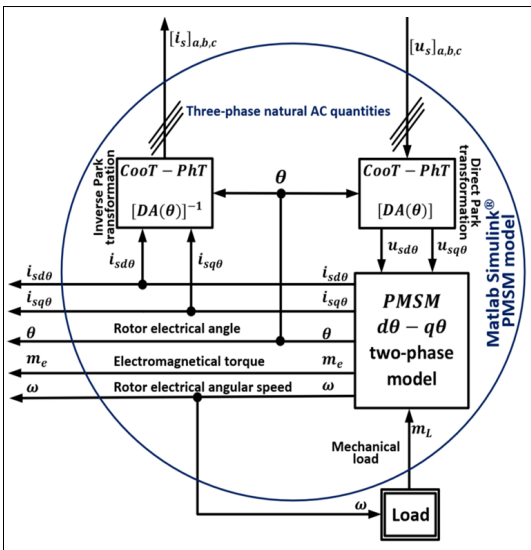


Fig. 9. Block diagram of the three-phase motor model from the MATLAB-Simulink® library.

With the $[DA(\theta)]$ operator the direct Park-transformation can be written as follows:

$$\begin{bmatrix} g_{sd\theta} \\ g_{sq\theta} \\ g_{s0} \end{bmatrix} = [DA(\theta)] \begin{bmatrix} g_{sa} \\ g_{sb} \\ g_{sc} \end{bmatrix}, \quad (22)$$

where the variable g may be current (i), voltage ($u, v, e, \Delta u$), or flux (Ψ), etc [1–3].

The matrix operator of the reverse Park-transformation is:

$$[DA(\theta)]^{-1} = \begin{bmatrix} \cos(\theta) & -\sin(\theta) & 1 \\ \cos\left(\theta - \frac{2\pi}{3}\right) & -\sin\left(\theta - \frac{2\pi}{3}\right) & 1 \\ \cos\left(\theta + \frac{2\pi}{3}\right) & -\sin\left(\theta + \frac{2\pi}{3}\right) & 1 \end{bmatrix}. \quad (23)$$

With this matrix the reverse Park-transformation is written as below:

$$\begin{bmatrix} g_{sa} \\ g_{sb} \\ g_{sc} \end{bmatrix} = [DA(\theta)]^{-1} \begin{bmatrix} g_{sd\theta} \\ g_{sq\theta} \\ g_{s0} \end{bmatrix}. \quad (24)$$

The reverse Park-transformation is applied in **Figure 9** inside the motor block for the output currents and in **Figure 8** in the control structure for the voltage references, corresponding to a three-phase sine-wave vectorial signal generator.

The direct Park-transformation is applied in **Figure 8** in the control structure for the feedback currents and in **Figure 9** inside the motor block for the input voltages.

Because in the MaMo of the motor block the current two-phase components are state variables, these can be directly connected to the input of the UsC voltage computation block, consequently the direct Park-transformation is not needed to provide the current feedback in the simulation of the control structure from **Figure 8**, only for its implementation, however, it is necessary to generate the voltage reference values by means of a reverse Park-transformation.

For the compatibility between the simulation results of the vector control structure from **Figure 8** the motor calculations and the simulation results of the simplified structures, which are applied for sinusoidal operation, the control structure will be simulated with sine-wave variables, without PWM-control of the VSI.

6. Simulation results

The simulations were gradually performed, starting with the simplest static structures, compared with the dynamic ones, in which the per-

pendicularity of the current to the PM flux was realized without controllers. So, we can check the motor measured parameters and the calculated rated data. It was only after these initial steps that we simulated the drive control system with the structure shown in **Figure 8**.

In simulations of the vector control structures the moment of inertia value $J_{Eq} = 5.5 \cdot 10^{-4} \text{ kgm}^2$, was similar to the simulations of the simplified dynamic structures (Dy-SimS). The value of the moment of inertia does not exceed the permissible limit given in the motor manual, which in our case is $J_{Eq}^{Max} = 6.634 \cdot 10^{-4} \text{ kgm}^2$.

6.1. Simplified simulation structures with voltage input

The simulation results of the simplified static (St_SimS_U) and dynamic (Dy_SimS_U) structures with voltage and load torque input are presented in **Figures 10–12**.

In **Figure 10** can be seen that the voltage was linearly increased from the

$$U_{s0} = \Delta u_R = R_s I_{sN}^{ef} = 5.33 \Omega \cdot 1.4 \text{ A} = 7.462 \text{ V}$$

boost value, and the torque from zero to the rated value in 1 s, and held at these values for 1 s, while the system reached the steady state and both the current and the speed (frequency) reached their rated values. Then in 1 s maintaining the torque at rated value, the motor voltage was reduced to the U_{s0} boost value, which corresponds to the steady state at zero speed and rated load torque.

Figure 10 shows the speed as a function of torque, according to the cycle described above for both simplified structures, i.e. the static (St_SimS_U) and dynamic (Dy_SimS_U) ones. The intersection of the two mechanical characteristics (MeCh) is clearly visible during both steady states, at rated load torque and rated or zero speed, respectively.

In the time diagrams from **Figures 11** and **12** in steady state, during the 1–2 s and 3–4 s intervals, the corresponding variables become equal, i.e. the static and dynamic curves are superimposed.

The transients of the current and of the EMT proportional to the current can be attributed to the lack of voltage control, despite of ramping of the voltage and load torque inputs instead of step variation, both during starting and braking.

A completely different result is obtained with the frequency input structures, where the calculation of the voltage would correspond to an ideal voltage control.

6.2. Simplified simulation structures with frequency input

The simulation results of the simplified static (St_SimS_f) and dynamic (Dy_SimS_f) structures with frequency and load torque input are presented in **Figures 13–15**, where the RPM value is represented instead of the frequency ($n = 60 f_s / z_p$).

The acceleration during starting and the deceleration at braking take place under constant dynamic torque, when due to the linearly increasing load the current also increases linearly.

In the simulation results of the frequency input dynamic structure spikes appear caused by the signal derivatives, which in the saved results are detected and filtered with the „ischange” („in_array”, „MaxNumChanges”, „maxChanges” parameter) MATLAB® function.

Compared to the results of the previous subsection obtained in the case of the voltage input structure, where decaying transients appear due to the first order lag (FOL), in case of the frequency input structure the transients disappear instantaneously without any delay.

6.3. Vector control structure with sinewave variables without PWM

The ideal sinusoidal operation of the vector control simulation structure (VC_SimS_Sin) is solved by omitting in **Figure 8** the PWM-VSI and the three-phase supply of the motor MaMo from **Figure 9** is simulated with the three modulation reference signals $[u_s]_{a,b,c}^{Ref}$. The simulation results of the above-described VC_SimS_Sin structure are shown in **Figures 16–18** and **22**.

The simulation was performed under the same conditions as for the simplified structures, according to the same load cycle. The reference signal of the speed was also increased for starting and reduced at braking with a ramp function in the same manner as for the static structure.

By simulating the VC_SimS_Sin, the correctness of the Simulink® motor block parameterization can be checked, by comparing it with the previously simulated simplified structures, because in steady state the same results should be obtained regardless of which structure is involved.

6.4. Vector control structure of the PWM-voltage fed PMSyM

The vector-controlled drive system shown in **Figure 8** was simulated with the three-phase motor model from **Figure 9** (it is called VC_Sim_PWM)

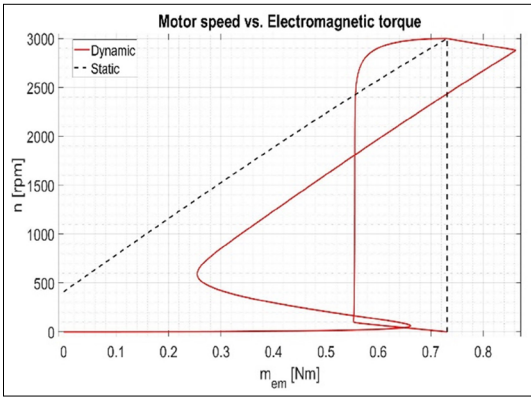


Fig. 10. Static (black dashed) and dynamic (red) mechanical characteristics simulated with the voltage input structures from Fig. 5 (St_SimS_U) and Fig. 7 (Dy_SimS_U).

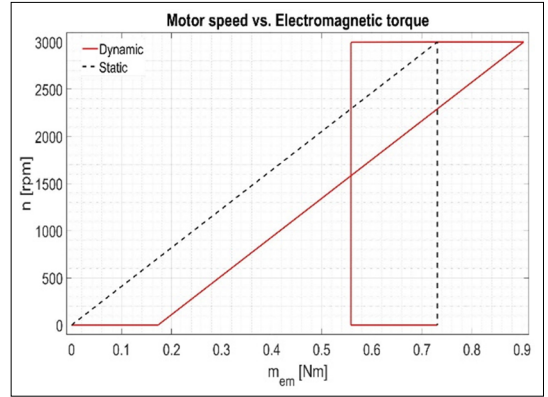


Fig. 13. Static (black dashed) and dynamic (red) mechanical characteristics simulated with the frequency input structures from Fig. 4 (St_SimS_f) and Fig. 6 (Dy_SimS_f).

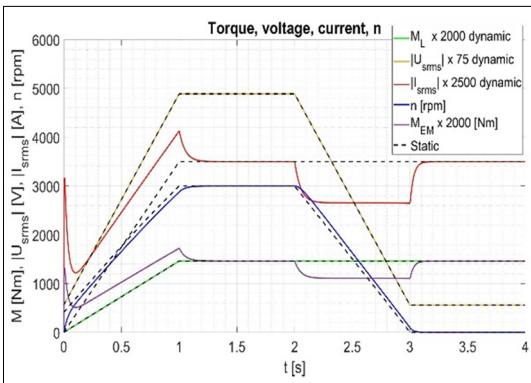


Fig. 11. Static (black dashed) and dynamic (colored lines) time diagrams simulated with the structures from Fig. 5 (St_SimS_U) and Fig. 7 (Dy_SimS_U): input voltage (yellow) and load torque (green), the output current (red), speed (blue) and EM torque (purple).

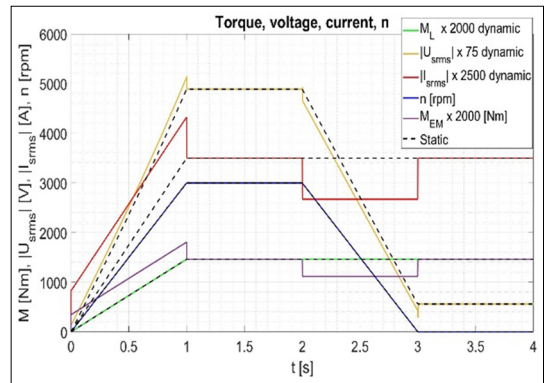


Fig. 14. Static (black dashed) and dynamic (colored lines) time diagrams simulated with the structures from Fig. 4 (St_SimS_f) and Fig. 6 (Dy_SimS_f): input speed (blue) and load torque (green), the output voltage (yellow), current (red) and EMT (purple).

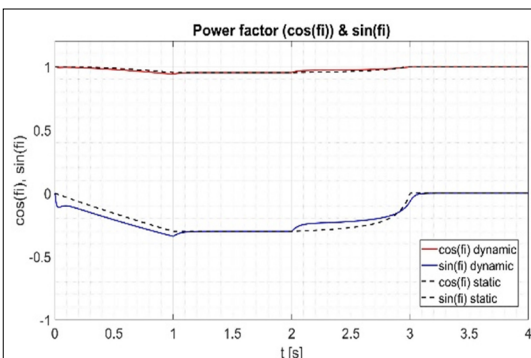


Fig. 12. Static (black dashed) and dynamic (colored lines) time diagrams of the $\cos\varphi$ power factor (red) and $\sin\varphi$ (blue) simulated with voltage input structures.

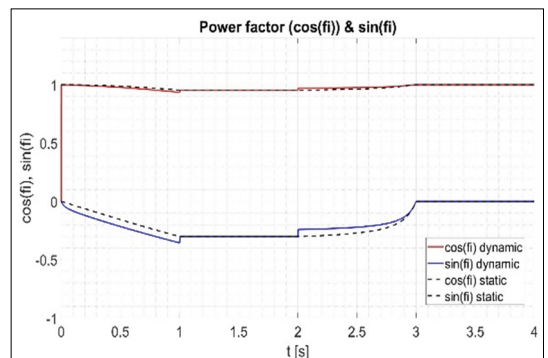


Fig. 15. Static (black dashed) and dynamic (colored lines) time diagrams of the $\cos\varphi$ power factor (red) and $\sin\varphi$ (blue) simulated with frequency input structures.

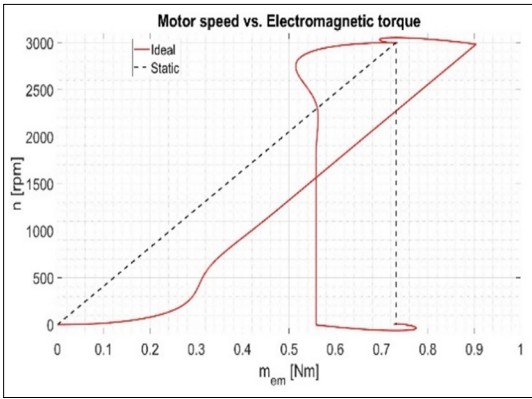


Fig. 16. Static (black dashed) and dynamic (red) mechanical characteristics of the vector control structure (VC_SimS_Sin) simulated with the Simulink® motor block fed by sinusoidal voltages.

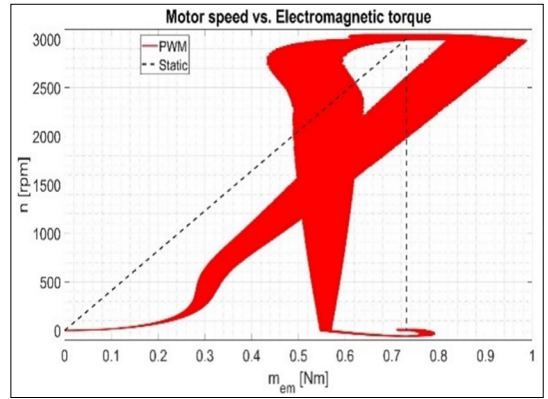


Fig. 19. Static (black dashed) and dynamic (red) mechanical characteristics of the vector control structure (VC_SimS_PWM) simulated with the Simulink® motor block fed by an ideal PWM-inverter.

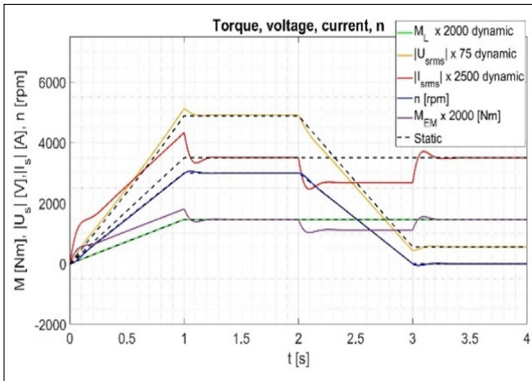


Fig. 17. Static (black dashed) and dynamic (colored lines) time diagrams of the VC_SimS_Sin structure: load torque (green), EMT (purple), speed (blue), current (red) and voltage (yellow).

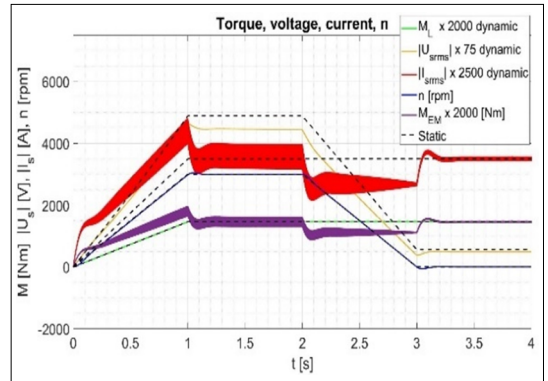


Fig. 20. Static (black dashed) and dynamic (colored lines) time diagrams of the VC_SimS_PWM structure: load torque (green), EMT (purple), speed (blue), current (red) and voltage (yellow).

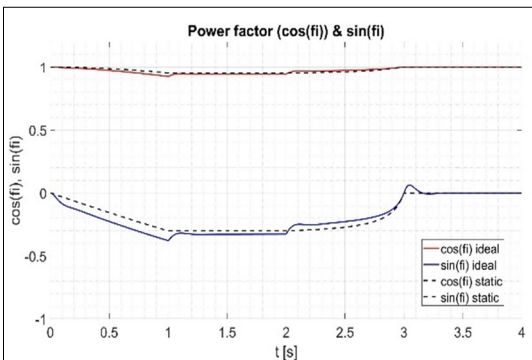


Fig. 18. Static (black dashed) and dynamic (colored lines) time diagrams of the $\cos\phi$ power factor (red) and $\sin\phi$ (blue) simulated with the VC_SimS_Sin structure.

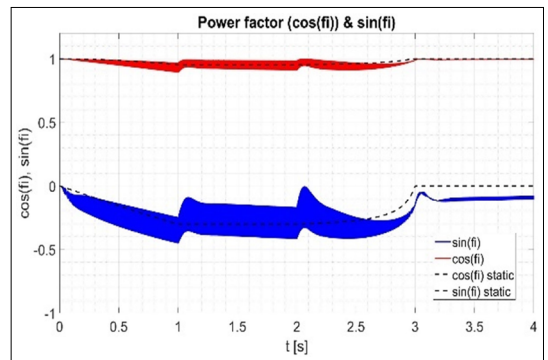


Fig. 21. Static (black dashed) and dynamic (colored lines) time diagrams of the $\cos\phi$ power factor (red) and $\sin\phi$ (blue) simulated with the VC_SimS_PWM structure.

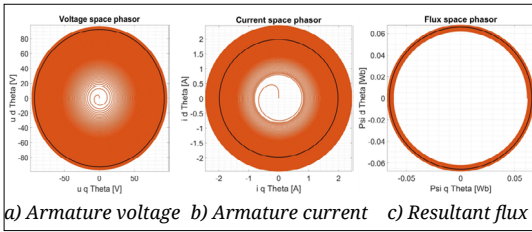


Fig. 22. Space-phasor diagrams of the structure VC_SimS_Sin during the first 1.5 seconds of the start-up (orange) and in rated steady state during ten periods in 1.45 - 1.5 s interval (black).

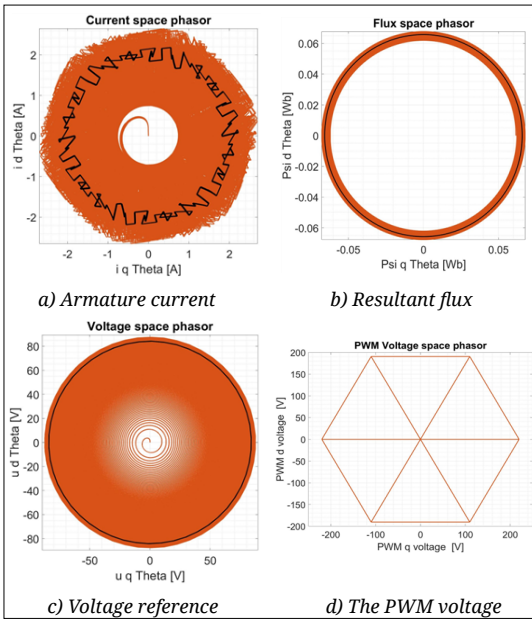


Fig. 23. Space-phasor diagrams of the structure VC_SimS_PWM during first 1.5 seconds start-up (orange) and in rated steady state during ten periods in 1.45 - 1.5 s interval (black).

under the same conditions as the previous structures, with the difference that there was included an idealized PWM-inverter model realized with simple bi-positional switches.

The three-phase motor block is connected to the output of the ideal inverter by the „Controlled Voltage Source” Simulink® library block.

The simulation results obtained with 220 V DC link voltage and $f_s^{CrW} = 5$ kHz frequency of the carrier wave are shown in Figures 19–21 and 23.

The simulation results were generated with maximum integration step size: 5 μ s by means of the solver method „ode23t(mod.Stiff/Trapezoidal)”.

Compared to the results of the subsection 6.3 the effect of the PWM control in pulsation of the cur-

rent and electromagnetic torque EMT is clearly visible.

The effect of the PWM control also occurs in the input errors of the current component controllers, but it is no longer noticeable in the speed error, because the drive system naturally filters it out thanks to the moment of inertia of the drive.

The recommended minimum frequency of the carrier wave must be at least 20 times the maximum f_s stator frequency, which at the rated value $f_{SN} = 200$ Hz would be minimum $f_{Min}^{CrW} = 4$ kHz, so the modulation frequency used in the simulation meets this condition.

It is noticeable that at starting with increasing the operating frequency the pulsation of the current and electromagnetic torque increases. This can be explained by the fact that at low speeds, where the supply frequency is also low, the number of the modulated pulses during a period is higher than at the rated speed.

According to the procedure presented in this paper the experimentally determined parameters and calculated data of a given motor can be checked.

7. Conclusions

The simulation results of the two simplified static structures, with two types of input (St_SimS_U and St_SimS_f), are the same.

The steady state of the dynamic structures is the same, but the transient processes differ.

Furthermore, the correctness of the MaMo parameterization used in the simulations can also be checked.

The presented simulation results confirm the correct identification of the motor data and parameters and prove the functional ability of the vector control structure.

In the future, the motor feeding will be simulated with the „Universal Bridge” inverter model from the Simulink® library, which will be even closer to the practical solution.

In the following, in the vector control structure the carrier wave modulation will be replaced with space vector modulation (SVM), which can optimize the inverter operation with the so-called “flat top” two-phase modulation, reducing the commutation losses by up to 30%.

The research continues with the implementation of the vector control drive system on a test bench built in the power electronics laboratory in the Faculty of Târgu Mureş of the Sapientia Hungarian University of Transylvania.

References

- [1] Kelemen A., Imecs M.: *Sisteme de reglare cu orientare după cîmp ale mașinilor de curent alternativ*. Editura Academiei Române, București, 1989.
- [2] Kelemen Á., Imecs M.: *Vector Control of AC Drives*. Vol. 2: *Vector Control of Synchronous Machine Drives*. Écirture Kiadó, Budapest, 1993.
- [3] Imecs M., Szabó Cs.: *Permanens-mágneses-forgórészű szinkronmotor*. *Terminológia, Magyar nyelvű szakelőadások a 2002–2003-as tanévben*. Erdélyi Magyar Műszaki Tudományos Társaság – EMT, Kolozsvár, 2004, 56–64.
- [4] Imecs M., Birou I., Jánky P., Kelemen Á.: *High performance control of PM-synchronous servomotors using the MS320C5x processor*. Intelligent Motion, International Conference on Power Electronics and Intelligent Motion – PCIM'97, Nürnberg, Germany, 1997, 157–166.
- [5] Imecs M.; Birou, I.; Szabó, Cs.: *Control strategies for synchronous motors with permanent magnet or constant exciting current*. Proceedings of Power Electronics and Intelligent Motion International Conference – PCIM'99, Nürnberg, Germany, June 22–24, 1999, 339–344.
- [6] Imecs M., Birou I., Szabó Cs.: *Modelling and simulation of vector-control strategies for PM-synchronous motors.*, Proceedings of the IEEE-TTTC International Conference on Automation, Quality and Testing, Robotics Q&A-R 2000, Tome 2, Cluj-Napoca, 2000, 151–156.
- [7] *** Product Details - Industry Mall - Siemens China, SIMOTICS S-1FL6 SERVO MOTOR Manual (add-furnace.com)
<https://www.add-furnace.com/product-catalog/siemens/simotics-s-1fl6-servo-motor-manual.pdf>
- [8] Imecs M., Ferencz J., Kelemen A.: *Vektoriálisan szabályozott permanens mágneses szinkron gépek hajtás egyszerűsített modellezése és szimulálása*. ENELKO 2023 – XXIV. Nemzetközi Energetika-Elektrotechnika Konferencia, Kolozsvár, 2023. okt. 12–15, EMT, Kolozsvár, 2023.10.11, 7–13.
<https://ojs.emt.ro/enelko-szamokt/issue/view/59>
<https://ojs.emt.ro/enelko-szamokt/article/view/1340/1350>
- [9] IEC/EN 60034-30-1, International Efficiency Classes, Standard on Efficiency Classes for Low Voltage AC Motors.
<https://webstore.iec.ch/publication/136>



NON APPROXIMATIVE MODELLING OF INVOLUTE GEAR PAIR SLIDING

Márton MÁTÉ,¹ Krisztina SZÓCS²

¹ Sapiientia Hungarian University of Transylvania, Faculty of Technical and Human Sciences, Department of Mechanical Engineering. Târgu Mureș, Romania, mmate@ms.sapiientia.ro

² Sapiientia Hungarian University of Transylvania, Faculty of Technical and Human Sciences, Department of Mechanical Engineering. Târgu Mureș, Romania, szocs.krisztina@student.ms.sapiientia.ro

Abstract

One of the main problems with the operation of involute tooth gears is that during engagement, the tooth profiles slide. The point of contact is the only point where pure rolling occurs among the engaging tooth profiles. This sliding, coupled with abrupt changes in load, collectively contribute to the failure and various malfunctions of the gears. In this research, the theoretical behavior of gears during sliding is studied. Existing mathematical models are examined for describing sliding and the results analysed. Then, a precise mathematical model developed for this research is presented. In creating the model, the aim was to avoid any geometric approximations and only consider the profile points where actual engagement between the gears could occur. Therefore, the contact points are interpreted within the real engagement zone. The overall goal is to create a mathematical solution that is equally applicable to simple and general involute tooth gear drives and which provides an accurate, realistic description of the relative sliding of gears.

Keywords: gear, sliding, exact method, gear engagement.

1. Introduction

In the case of gear drives, except for the cycloidal drive, the teeth do not roll cleanly over each other, slippage occurs and this can lead to rapid tooth wear. Common tooth failures include tooth surface damage such as progressive wear, pitting and chipping. Slippage between tooth surfaces causes wear, especially during the "break-in" phase after assembly, when prominent microgeometric irregularities in tooth surfaces are worn away by sliding with the counter gear. This type of wear diminishes and then disappears over time. It is not considered a failure because it leads to an increase in the contact area of the gears, which in turn increases the life expectancy of the drive. The problem is progressive wear, which occurs when wear increases after the running-in phase. Causes include: inadequate or insufficient lubrication, inadequate lubricant or dirt in the lubricant, or insufficient hardness of the tooth surfaces. Pitting occurs around the intersection of the tooth surface and the rolling

surface. It occurs when the shear stress induced by the surface compressive stress and the sliding of the tooth surfaces against each other exceeds a limit value related to the number of cycles. First, small hairline cracks appear in the vicinity of the rolling surface tooth alignment, below the surfaces where the composite stress is greatest. As these hairline cracks reach the surface parts of the material fragment, forming dimples with rough edges. Pitting is mainly caused by surface fatigue of the material due to inadequate sizing or uneven surface load distribution, and inadequate hardness of tooth surfaces. Scratches on the tooth surface are short, straight, very shallow grooves in the direction of tooth profile sliding, caused by dust particles or other small impurities in the lubricating oil. The grooves are deeper than the scratches and occur in groups. Inadequate lubrication causes metallic contact between the tooth surfaces, causing them to momentarily weld together. However, due to the relative sliding of the tooth surfaces, the welded particles are torn out

of one of the tooth surfaces. These particles can subsequently contaminate the lubricating oil and cause further damage to the tooth surface. This phenomenon is called chewing. In the 20th century, many studies were carried out to increase the load capacity and service life of gears. The sliding between tooth surfaces and the sliding speed have been studied extensively. Vidéki [1] found a close relationship between service life and sliding speed. He found that the sliding velocity decreases when the spindle distance is increased as much as the gearing allows. Diker [2], Szeniczai [3] and Bolotovszkij [4] based their design of gear drives on relative sliding. Szeniczai developed a model describing the relative slip for gear drives with an involute profile. This model is based on an approximation, since instead of the involute arc length, he used the arc length of the simulation circle, where the radius of the simulation circle is equal to the radius of curvature. According to his calculations, the length of the circular arcs can be obtained as the product of the radius of curvature, denoted ρ and the angular rotation of the gear, denoted γ , which, as above, is $\rho_1 \cdot \gamma_1$ for one gear and $\rho_2 \cdot \gamma_2$ for the other gear. Thus, the value of the relative slip from Figure 1 is:

$$\chi = \frac{\rho_1 \cdot \gamma_1 - \rho_2 \cdot \gamma_2}{\rho_1 \cdot \gamma_1} \tag{1}$$

The relative slip is described by a hyperbolic function, which shows that the relative slip is zero at the principal point and increases steadily away from the principal point (Figure 2).

However, the model also shows that the relative slip is zero at the principal point of coupling. This would imply that there is no wear at that point. This statement was contradicted by the experiments of Gavrilenko [5] Through his experiments he established a new method for sizing gears. He used slip accelerations to determine the location and magnitude of tooth surface wear. He described the tooth surface failure by taking the positional derivative of the relative slip along the contact line. The Ganz-Botka evolutionary tooth system is also based on relative slip. Botka [6] sought to compensate for relative slip when designing gears. He proved that if the relative slip values at the interface points are equalized, this implies the equalization and minimization of the instantaneous temperature rise and Hertzian stress and slip velocity multiplications of the tooth surfaces.

Research on the sizing of gear drives using relative slip and slip accelerations is still ongoing [7].

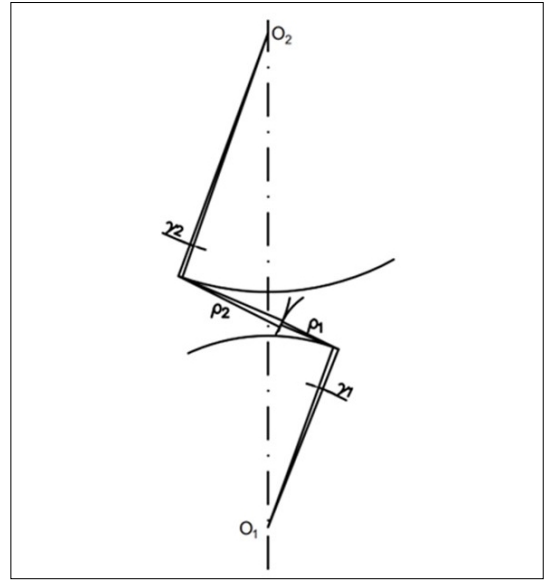


Fig. 1. Gears in the moment of engagement.

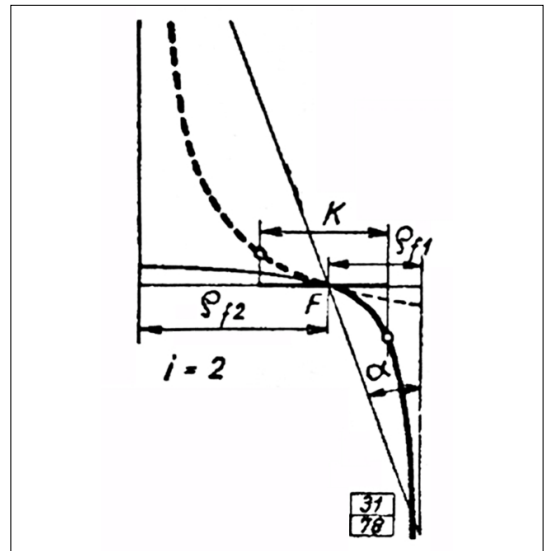


Fig. 2. The relative sliding curve. [3]

Many studies based on relative slip are matched with the model proposed by Szeniczai, which only approximates the real geometric ratios. In this thesis, our aim was to rethink this model in a way that avoids geometric approximations. Specifically, we wished to obtain a more accurate and realistic value for the relative slip. The hypothesis is that this may help in the future to design gear drives with increased gear life.

2. The proposed mathematical model

The basis of this research was to avoid any kind of geometric approximation when writing up relative slip. It was intended to investigate the points where the coupling between tooth surfaces could actually occur, so the coupling points within the real coupling section were interpreted. To achieve this the Erney diagram was used, as it contains the essential geometric elements of the gear drive without the need to draw circles [8]. The figure shows that the connecting line is the common tangent of the base circles. The actual coupling is established at A_1A_2 which is defined by the intersection of the coupling line and the head circles A_1 and A_2 (Figure 3). The theoretical coupling section is defined by the points T_1 and T_2 of the base circles tangent to the coupling line.

Figure 4.a. shows the relationship between the switching line and the position of the teeth. It can be seen that in all cases the points of contact are located in the plane of the coupling. The message in Figure 4. c. is equivalent to that in Figure 2: the relative slip is zero at the principal point and increases steadily away from the principal point.

Subsequently, the optimal sizing of the gear drive was checked. We investigated where the point cut out by the base circles lies on the coupling line. This is significant because if its location is not correct, the task would require re-sizing the drive pair since, within these circles, instead of the involute profile ensuring correct coupling, is

the derived looped involute or epicycloid of the root curve, and the involute profile should not be coupled with the root curve. It can therefore be stated that the coupling is correct if the head circle of the steering wheel intersects the coupling section outside the section defined by the base and base circle points of the wheel.

The first step is to add the points T_1 and T_2 which are at a tangent to the base circle. Next, we record the intersection points A_1 and A_2 of the head circles and the connecting line. From Figure 3 the following relationships can be written:

$$T_1A_1 = \sqrt{r_{a1}^2 - r_{b1}^2} \tag{2}$$

$$T_2A_2 = \sqrt{r_{a2}^2 - r_{b2}^2} \tag{3}$$

$$T_1T_2 = a_w \cdot \sin \alpha \tag{4}$$

$$T_1A_2 = T_1T_2 - T_2A_2 \tag{5}$$

$$T_2A_1 = T_1T_2 - T_1A_1 \tag{6}$$

$$A_1A_2 = T_1T_2 - T_1A_2 - T_2A_1 \tag{7}$$

Consider the point P, which is the intersection of the line of contact and the rolling circle, observing Figure 5, we can write down the following equations:

$$OT = \frac{m \cdot z}{2} \cdot \cos \alpha \tag{8}$$

$$LP = (h_0 - \xi + c_0 - \delta) \cdot m \tag{9}$$

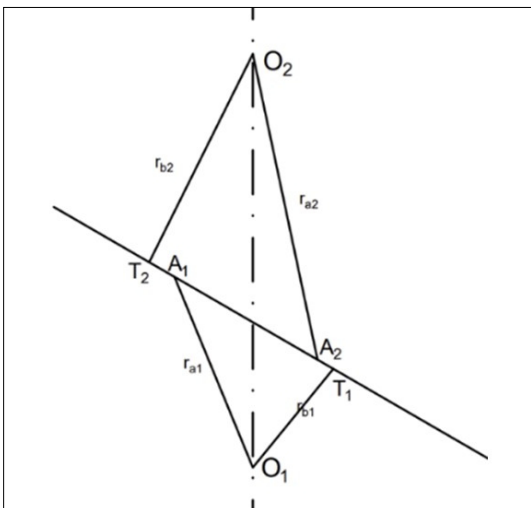


Fig. 3. The simplified model of the Erney diagram.

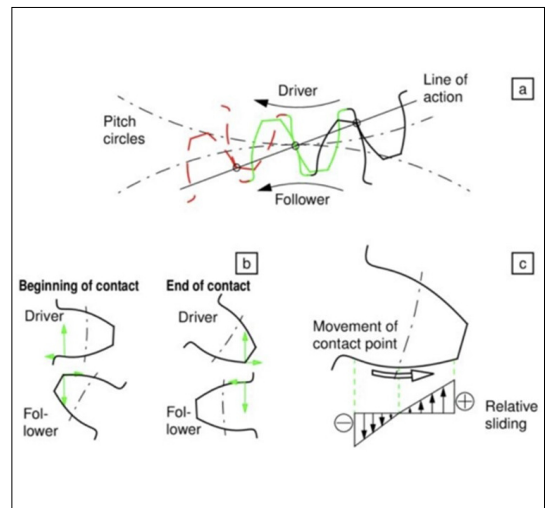


Fig. 4. The sliding of gears, [9] a) The meshing of the teeth during transmission; b) The position of the teeth at the beginning and end of engagement; c) The relative sliding occurring on the teeth.

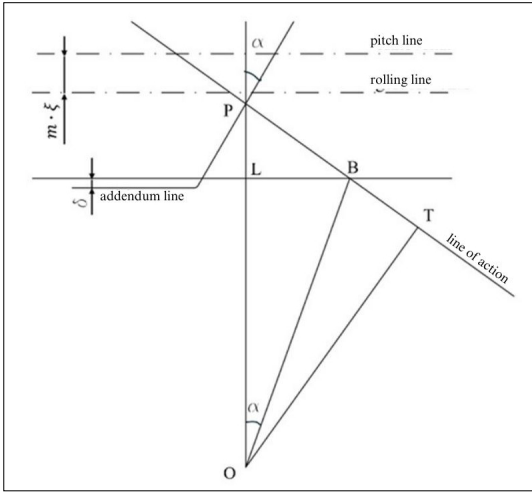


Fig. 5. The calculation of the root circle radius.

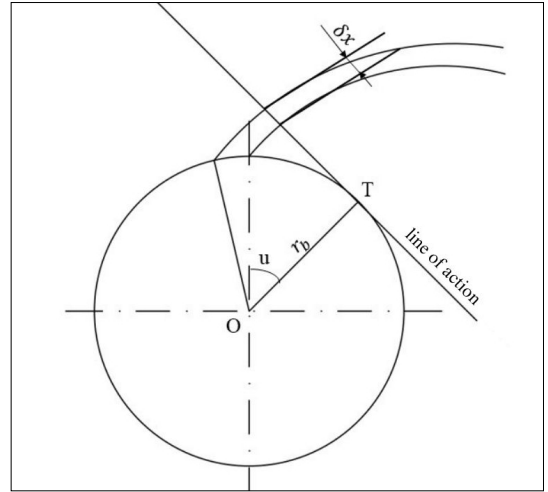


Fig. 6. The calculation of the involute arc length.

$$PB = \frac{LP}{\sin \alpha} \tag{10}$$

$$BT = PT - PB = OT \cdot \operatorname{tg} \alpha - PB \tag{11}$$

$$r_t = \sqrt{BT^2 + OT^2} \tag{12}$$

It follows that the distance between the points cut by the base circles and the head circles on the contact line and the points of contact of the base circles is:

$$B_1 T_1 = \sqrt{r_{t1}^2 - r_b^2} \tag{13}$$

$$B_2 T_2 = \sqrt{r_{t2}^2 - r_b^2} \tag{14}$$

The points of contact of the base circles and the intersection of the root and head circles define the real working contact. The connection is good if the head circle of the counterpart wheel intersects the coupling section outside the section defined by the root and base circle points of the respective wheel, i.e

$$T_1 A_2 \geq T_1 B_1 \text{ and } T_2 A_1 \geq T_2 B_2 \tag{15}$$

The slip is defined here as the difference between the evolutionary arc lengths $\Delta \ell_1$ and $\Delta \ell_2$ corresponding to the distance between two finitely spaced attachment points. Formulas (16) and (17) are used to calculate the evolution arc lengths. To write the evolute arc length, we need to use the central angle corresponding to the rolling of the line generating the evolute on the base circle, i.e. a parameter u . Under the angular rotation u , the arc length of the circle affected by the generating

line is equal to the product of the base circle of radius r_b and the angular rotation u . The evolute generating line makes a planar motion with respect to the base circle, the instantaneous pole of which is the point of contact, i.e., for a given decoiling position, the radius of the evolute curve is given by exactly the segment of length $r_b u$, so that the elementary arc length of the evolute curve is $d\ell = r_b u du$. This expresses two decoiled evolute arc lengths corresponding to finite values of angular rotation u (Figure 6):

$$\Delta \ell_1 = \int_{u_1}^{u_2} r_{b1} \cdot u \cdot du = \frac{r_{b1} \cdot (u_2^2 - u_1^2)}{2} \tag{16}$$

$$\Delta \ell_2 = - \int_{u_1}^{u_2} r_{b2} \cdot u \cdot du = \frac{r_{b2} \cdot (u_1^2 - u_2^2)}{2} \tag{17}$$

The value of the relative slip can be obtained by relating the difference in the evolutionary arc length to the smaller evolutionary arc length, which in our case is the one associated with the driving wheel.

$$\chi = \frac{\Delta \ell_1 - \Delta \ell_2}{\Delta \ell_1} \tag{18}$$

The calculation function of the evolutionary arc length is written according to the following pseudocode:

<N> = 100	the number of points along the contact line
< δx > = $\frac{A_1 A_2}{N - 1}$	the length of the section travelled by the interface on the contact line

cycle from $\langle i \rangle = \langle 0 \rangle$ to $\langle N - 2 \rangle$	definition of the loop variable
$\langle u_1 \rangle = \frac{T_1 A_2 + \text{változó1} \cdot \delta x}{r_{b1}}$	lower parameter of the driving wheel
$\langle u_2 \rangle = \frac{T_1 A_2 + \text{változó1} \cdot \delta x + \delta x}{r_{b1}}$	upper parameter of the driving wheel
$\langle u'_1 \rangle = \frac{T_1 T_1 - (T_1 A_2 + \text{változó1} \cdot \delta x)}{r_{b2}}$	lower parameter of the driven wheel
$\langle u'_2 \rangle = \frac{T_1 T_1 - (T_1 A_2 + \text{változó1} \cdot \delta x + \delta x)}{r_{b2}}$	upper parameter of the driven wheel
$\langle dl_1 \rangle = \frac{r_{b1} \cdot (u_2^2 - u_1^2)}{2}$	length of the arc in contact with the driving wheel
$\langle dl_2 \rangle = \frac{r_{b2} \cdot (u_1'^2 - u_2'^2)}{2}$	length of arc in contact with driven wheel
$\langle \chi \rangle = \frac{dl_1 - dl_2}{dl_1}$	relative slip value
$a_{i,0} = i \cdot \delta x$	first column of the output, length of the distance travelled on the contact line
$a_{i,1} = \chi$	second column of output, value of relative slip
cycle end	
return a	

According to the code, we obtained the relative slip model for elementary gears. Subsequently, we wished to investigate the use of the model for general-purpose involute gear drives. To achieve

Table 1. The parameters of the gears

Title	Indication	Value
Module [-]	m	4
Pressure angle [rad]	a	$\pi/9$
Drive gear tooth number [-]	z_1	17
Driven gear tooth number [-]	z_2	34
Drive gear pitch radius [mm]	r_{w1}	34
Driven gear pitch radius [mm]	r_{w2}	68
Drive gear root radius [mm]	r_{f1}	29
Driven gear root radius [mm]	r_{f2}	163
Drive gear tip radius [mm]	r_{a1}	38
Driven gear tip radius [mm]	r_{a2}	72
Drive gear base radius [mm]	r_{a1}	31.94
Driven gear base radius [mm]	r_{a2}	63.89
Tooth height [mm]	h	9
Tooth thickness [mm]	c	1
Center distance [mm]	a_w	102

this, the maximum and minimum possible profile offsets were calculated, according to the literature, and then applied to the number of teeth of our choice. The maximum profile shift from the second law of evolutionary trigonometry and the minimum profile shift from the known geometric model of spline gearing were calculated, [3].

2.1. Numerical evaluations

The next part of the study is the numerical evaluation of the models. The mathematical models were applied to a specific gear drive in the MathCad environment, the parameters of which are shown in **Table 1**. The MathCad environment was chosen because it allowed easy verification of the calculations and the creation of graphs.

Using the relations (2) - (14), the length of the radius of the root circles was calculated taking into account the values defined in **Table 1** and the position of points B_1 , B_2 . Since we aim for simplification, we do not consider profile shift, so tip clearance $h_0 = 1$ mm, root clearance $c_0 = 0.25$ mm, profile shift $\xi = 0$ mm and tooth root height $\delta = 0.15$ mm. Applying the equations to both the driving and driven wheels, we see that the radius of the root circle of the driving wheel is $r_{t1} = 31.97$ mm and the radius of the base circle of the driven wheel is $r_{t2} = 4.73$ mm.

Therefore, since $A_1 T_2 = 14.31$ mm, $A_1 T_1 = .23$ mm and $A_3 T_1 = 1.70$ mm, $B_2 T_2 = 10.39$ mm, it follows that the points intersected by the root circle are between the points intersected by the tip circle and the points intersected by the base circle, i.e. point B_1 is between T_1 and A_2 , and point B_2 is between T_2 and A_1 . In conclusion, we can say that the fold under consideration is correctly connected, i.e. it does not require re-measurement.

In the following, the mathematical solution of Szeniczai has been transferred to the MathCad environment, in order to make it easier to compare the results with our proposed model. We calculated the relative slip between the teeth using our mathematical model. The minimum and maximum profile shifts of the chosen gear drive were examined (**Table 2**) in order to investigate how the models behave for general gearing..

Table 2. The limits of profile shifts for the selected number of teeth

Tooth number	Minimum profile shift	Maximum profile shift
17	0	0.83
34	-0.98	1.71

Table 3. The examined profile shifts

ξ_1	ξ_2
0	-0.3
0	0.3
0.3	0
0.5	0

It is shown that both negative and positive profile shifts are allowed on the driven wheel, while only positive shifts are allowed on the drive wheel. Values from the allowed ranges were chosen as profile offsets therefore we set up four cases for general gearing (Table 3), for which the model behaviour is investigated. According to the profile shift, the gear drive parameters and the relative slip both from the Szeniczai model and from the model were re-calculated.

3. Discussion

Figure 7 illustrates the results obtained for elementary gears. The functions obtained are hyperbolic, as expected. However, there are clearly visible differences between the hyperbolas plotted by the two relative slip functions. Although they

both show that as we move forward along the contact line, the relative slip between the gears decreases rapidly, their starting point and the moment when they reach zero differ significantly. In the Szeniczai solution, the initial value of the relative slip is considerably larger, almost double that in our model, and the zero point is reached at a point further along the line of contact.

Applying a profile shift to the drive wheel, the curves are visibly flattened, especially in the case of a positive profile shift (Figure 8). The curves representing the two models behave similarly when compared to the results obtained for the elementary gear. In the case of negative profile shifting, both curves show a reduction in the initial relative slip, reaching zero at almost the same point. For the positive profile shift, both curves start from a higher relative slip value, although the hyperbola illustrating the solution of Szeniczai has a much higher relative slip value compared to the elementary value and reaches the zero point much earlier than in the previous curves. The spatial difference between the two curves still remains: in our model, the value of relative slip, especially at the initial moment, is significantly smaller and reaches the moment of zero slip sooner at the contact line.

In the case of profile shifting on the driving gear, in both cases, the relative slip is reduced compared to the elementary gear, although it is reduced almost double in the case of the Szeniczai model compared to our model (Figure 9). Furthermore, observing the Szeniczai model, there does not seem to be any change relative to the elementary gear when the zero moment is reached, while in our solution the zero slip moment is more easily reached by positively shifting the profile of the driving wheel.

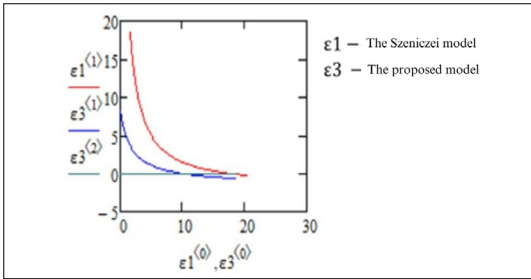


Fig. 7. Models describing relative sliding for elementary gearing.

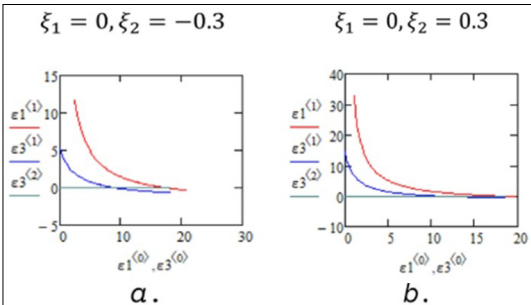


Fig. 8. Models describing relative sliding for elementary gearing, profile shifting performed on the driven gear a) negative profile shifting b) positive profile shifting.

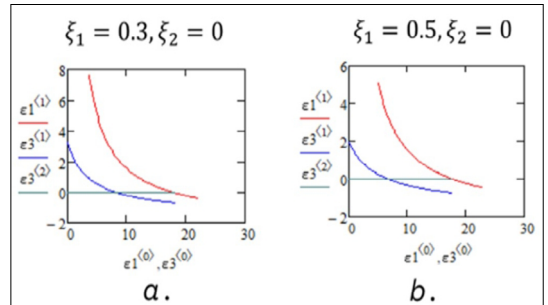


Fig. 9. Models describing relative sliding for elementary gearing, profile shifting performed on the driving gear a) 0.3 mm profile shifting b) 0.5 mm profile shifting.

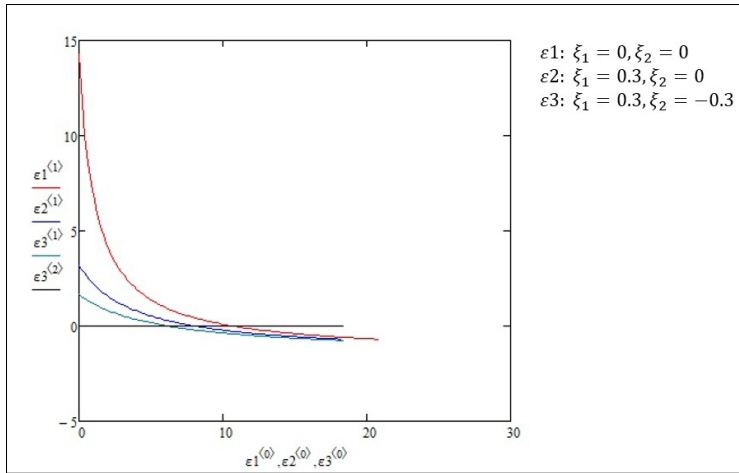


Fig. 10. The proposed model describing relative sliding for various profile shifts.

Figure 10 illustrates a proposed model for different profile shifts, which highlights how relative slip varies as a function of profile shift. It can be seen that the hyperbola flattens more and more as the profile shift increases. The model shows that the relative slip value can be significantly reduced by profile shifts on both gears. As shown in the figure, the relative slip value is then less than one third of the relative slip present in the case of elementary gears. The zero point is also reached sooner with a larger profile shift. At the same time, it is observed that the curves do not follow a new hyperbola after reaching the zero point, but almost converge. This allows us to conclude that the proposed model requires further, more detailed mathematical analysis, including the examination of specific cases.

4. Conclusions

Based on the evaluation of the results, it is observed that the relative slip is significantly reduced in the exact model compared to the previously established model. Moreover, the zero-slip condition is achieved earlier. Additionally, both elementary and general gears exhibit similar behavior across various profile shifts, indicating that the exact model of slip for involute gears applies universally.

The key mathematical difference between the Seniczei model and my proposed model is that in the classical (Seniczei) mathematical model, the angular rotations γ_1 and γ_2 satisfy the transmission ratio, i.e. $i_{12} = \frac{\omega_1}{\omega_2} = \frac{\gamma_2}{\gamma_1}$, so that the slip can

be interpreted as an instantaneous limit, i.e. $\chi = \frac{\rho_1 - i_{12} \rho_2}{\rho_1} = 1 - i_{12} \frac{\rho_2}{\rho_1}$, where the slip is only

affected by the ratio of the transmission ratio and the profile curvature radii corresponding to the instantaneous contact, my proposed model follows the path of the contact along the real contact section and gives the ratio of the differences between the relative contact sections corresponding to discrete time intervals. Considering that the micro-geometric, i.e. real contact of the surfaces can be interpreted in terms of finite rather than elementary displacements, I believe that the formulation of the model I have derived is appropriate.

Further investigation into how these new findings impact gear drive sizing, operation, and longevity is deemed crucial. Experimental studies on machine elements are necessary to validate these results and explore their practical implications. There is also potential to extend this methodology to accurately predict relative slip not only for involute profiles but also for other tooth profiles such as cosine or sinusoidal profiles.

References

- [1] Vidéki E.: *Fogaskerekek*. „Pátria” Irodalmi Vállalat és Nyomdaipari Rt. nyomása, Budapest, 1912.
- [2] Diker J. I.: *Evolventnije zaceplenyije sz uprjamimi zubcami*. Organmetal, Moszkva, 1935.
- [3] Seniczei L. *Az általános fogazás*. Királyi Magyar Egyetemi Nyomda, Budapest, 1941.
- [4] Bolotovskiy I. A., Bolotovskaya T. P., Bocharov G. S., Guryev V. I., Kurlov B. A., Merkurjev I. A.,

- Smirnov V. E.: *Spravochnik po geometricheskomu raschotuevolventnih zubchatih i chervyachnih peredach*. Mashinostroyenie, Moszkva, 1963.
- [5] Gavrilenko V. A.: *Osznovi teoriji evolventnoj zubsatoj peredaci*. Masinosztroyenie, Moszkva, 1966.
- [6] Botka I.: *Fogaskerek-méretezés kiegyenlített kontakt-hőmérsékletre*. Gép, 4/11. (1964) 425–430.
- [7] Tomori Z.: *A relatív csúszást leíró modellek, hajtó keréken végzett profileltolás esetén*. PhD-értekezés, 2019. (accessed on: 2024. 03. 28.)
<http://midra.uni-miskolc.hu/docu-ment/32638/29328.pdf>
- [8] Erney Gy.: *Fogaskerekek*. Műszaki Könyvkiadó, Budapest. 1983.
- [9] Alfredsson B.: *A Study on Contact Fatigue Mechanisms*. Doctoral Thesis no. 44. Department of Solid Mechanics, Royal Institute of Technology, Stockholm, Sweden, 2000. (accessed on: 2024. 04. 02.)
https://www.researchgate.net/publication/265867484_A_Study_on_Contact_Fatigue_Mechanisms



HEAT-TREATING PROCESSES OF THE TITANIUM ALLOYS

Ahmad Buhairi Minhalina Binti,¹ Pinke Péter,² Tóth László,² Kovács Tünde Anna²

¹ Óbuda University, Doctoral School on Material Sciences and Technology, Budapest, Hungary.

² Óbuda University, Bánki Donát Faculty of Mechanical and Safety Engineering, Budapest, Hungary.
kovacs.tunde@bgk.uni-obuda.hu

Abstract

Titanium is a metal with a short history and is the ninth most abundant element in the Earth's crust. It is expensive to produce but is increasingly used for its many useful properties. The application of titanium alloys has been increasing in recent decades because titanium is a low-density, high-strength, highly corrosion-resistant and biocompatible material. Its different alloys exhibit different mechanical properties. Heat treatments can be applied to achieve the required mechanical properties. These typical heat treatments achieve the desired properties by phase transformation of the microstructure or reduction of stress. In this summary study, the authors aim to present the typical heat treatments of titanium and its alloys.

Keywords: *titanium alloy, heat treatment, precipitation hardening, annealing.*

1. Introduction

Heat treatment is a technological process used to modify the mechanical, technological and/or chemical properties of materials.

Heat treatment technology is a process consisting of heating a material to a predetermined temperature, removing heat and then cooling it in order to achieve the desired properties or combination of properties, e.g. an increase in hardness, a softening of the material or an appropriate strength/heat ratio [1].

Heat treatment can be a process with or without a change in chemical composition. Chemical composition changes usually involve the diffusion of some chemical element into the surface of the material, e.g. carbon during cementation, and nitrogen during nitriding, to help achieve the desired mechanical properties such as hardness, and wear resistance.

The importance of heat treatments carried out without changing the chemical properties is relevant in the field of heat treatments, where changes in the fabric structure over the whole volume can be used to achieve changes in mechanical and other properties.

Titanium is a "new" metal, discovered in 1795 by the German chemist Martin Heinrich Klaproth

and named after the mythological titans (which were symbols of strength and toughness). In 1932, Wilhelm Kroll developed a process for extracting titanium, and in the 1940s, based on this process, commercially pure titanium began to be produced in industrial quantities [2].

The Kroll process produces pure titanium from ores (rutile (TiO₂), ilmenite (FeTiO₃)). In the first step, pure titanium dioxide is produced chemically or metallurgically, then it is heated together with carbon and chlorine to produce titanium tetrachloride (TiCl₄), which is reduced with magnesium melting at 900 °C. [2]. Reduction results in the formation of powdery or spongy titanium. The titanium sponge or powder is cleaned of magnesium residues by aqueous washing and dilute hydrochloric acid treatment, possibly by vacuum distillation. The resulting titanium is 99.4–99.9% pure followed by further processing. The high-purity titanium powder is powder metallurgically combined into blocks and then processed by a remelting process in a neutral protective gas or vacuum.

Titanium is the ninth most abundant element in the earth's crust, but its use has not been widespread because of the cost of its production. Titanium is an environmentally and human-friendly material. Its main properties are: low density

($\rho = 4500 \text{ kg}\cdot\text{m}^{-3}$), high strength (e.g. ASTM Grade 4 $R_m = 550 \text{ MPa}$), high corrosion resistance, biocompatibility [2, 3, 4].

Titanium and titanium alloys are now widely used in many areas of aerospace, energy, chemicals and automotive production. Many titanium alloys, due to their biocompatibility, are excellent materials for surgical prostheses and medical devices. With the advent of additive technologies, it has become even more widespread, particularly in the field of dental implants.

The heat treatment technology for titanium and titanium alloy products has evolved significantly in recent decades [5, 6]. In this paper, the authors have aimed to collect and systematize the main heat treatment technologies used in practice.

2. Titanium and alloys

Titanium is an allotropic metal, composed of αTi (hexagonal close-packed) and βTi (body-centred cubic) phases depending on temperature (Fig. 1) [7]. The temperature of the phase transition is 900°C [1].

Different alloys change the transformation or precipitation temperature of the resulting phases depending on the type and amount of the alloy. Alloying elements can be classified into three categories based on their effects [2]: - α phase stabilizing elements such as Al, O, N and C; - β phase stabilizing elements such as Mo, V, Ta, Nb (isomorphous elements), Fe, Mn, Cr, Co, Ni, Cu, Si, H (eutectoid forming elements) and -neutral elements such as Sn, Zr and Hf. The elements O, N, C and H form an interstitial solid-solid solution with titanium. All other elements form a substitution solid solution with titanium. The elements that stabilise the α phase expand the range of the α phase, and the elements that form the β phase expand the range of the β phase and simultaneously narrow the α phase field. Neutral elements have only a minor

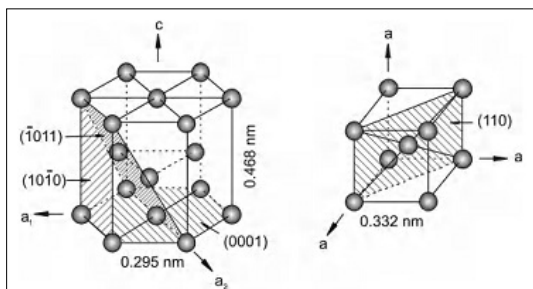


Fig. 1. Crystal structure of pure titanium α (hexagonal close-packed crystal lattice) and β (body-centred cubic crystal lattice) [7]

effect on the βt temperature. The effect of alloying elements on the phase diagrams of titanium alloys is summarised in Table 1.

Table 1. Titanium alloy types [7, 8]

Type	Alloy	Typical equilibrium diagram
Pure Titanium	-	
α solid solution	Al, O, N, C	
β stabilized	Mo, V, Ta, Nb	
Eutectoid	Fe, Mn, Cr, Co, Ni, Cu, Si, H	

2.1. α Titanium phase alloys

A single-phase alloy consisting of an α -phase solid solution. Whether at room temperature or higher practical application temperatures, it is α -phase, has a stable structure, higher wear resistance, is more stable than pure titanium and has strong corrosion resistance. At $500^\circ\text{C} \sim 600^\circ\text{C}$, it still retains its strength and creep resistance, but cannot be heat treated to increase its strength.

A significant group of α -phase alloys are near α titanium alloys, which also contain small amounts of β -phase alloys, for which strength-enhancing heat treatment can already be applied. Typical examples of near α alloys are Ti-8Al-1Mo-1V and Ti-6Al-5Zr-0.5Mo-0.2Si alloys [9].

2.2. ($\alpha + \beta$) Titanium phase alloys

A two-phase alloy with good structural stability, good toughness, good ductility and high-temperature ductile properties, which can be processed by hot forming and the strength of the alloy can be increased by ageing. The strength after heat treatment is about 50-100% higher than in

the annealed condition. The strength after heat treatment is about 50-100% higher than in the annealed state. This alloy retains its strength at high temperatures and can operate at temperatures between 400°C and 500°C for long periods [10, 11].

The α -phase is stabilised by Al, the main β -stabilisers are V, Mo, Nb and Cr, and the alloys often contain neutral elements such as Zr and Sn. Major biphasic ($\alpha + \beta$) alloys include Ti-6Al-4V, Ti-6Al-6V-2Sn and Ti-6Al-4Zr-2Sn-1Mo [9].

The Ti6Al4V alloy is a typical ($\alpha + \beta$) phase alloy. The schematic phase diagram (Fig. 2) shows the phases as a function of the alloy contents.

2.3. β Titanium phase alloys

Metastable β titanium alloys, which typically consist of a β -phase solid solution, have high strength before heat treatment. After solution annealing and subsequent ageing (precipitation hardening), the strength of the alloy can be further increased and the strength measured at room temperature can reach 1400 MPa. The most common β phase-forming alloys are V, Mo, Nb, Cr and Si, the α phase-forming alloys 3% Al and the neutral alloys Sn and Zr. Widely used β -titanium alloys include Ti-3Al-8V-6Cr-4Zr-4Mo (Beta C), Ti15Mo-3Nb-3Al-0.2Si (Timetal 21S) and Ti-15V-3Cr-3Sn-3Al [5]. Fig. 2 shows the area of the β -phase solid solution of Ti6Al4V alloy. The β stabilizer in this alloy is vanadium.

3. Heat treatment of titanium alloys

3.1. Stress relieving

Stress relief heat treatment is important for titanium alloys, especially for α -solid solution alloys. Stresses from the manufacturing steps can be reduced by this heat treatment. Stress relief heat treatment consists of annealing at 500 °C in a neutral atmosphere followed by slow cooling. The stress-relieving annealing temperature for ($\alpha + \beta$) alloys is between 500 °C ~ 700 °C, while that for metastable β alloys is higher, 700 °C ~ 800 °C [12].

3.2. Annealing

Annealing increases fracture toughness, ductility, dimensional and thermal stability, and creep resistance. Annealing is a heat treatment process in which a metal alloy is heated to a temperature slightly higher than the temperature of the solution annealing and then allowed to cool very slowly. The main purpose of the annealing process is to increase ductility and remove stresses from the material [12].

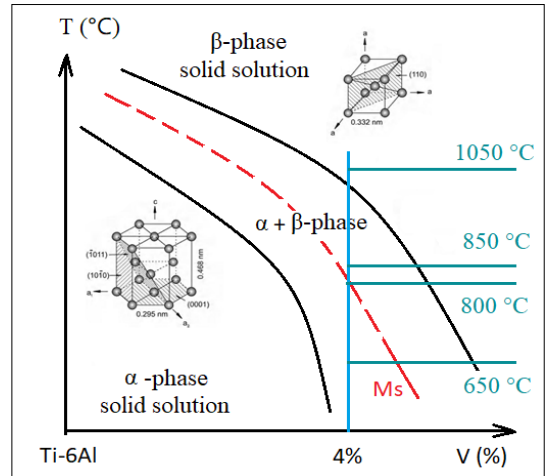


Fig. 2. Schematic phase diagram of the Ti6Al4V alloy.

Typical annealing:

1. Recrystallization annealing, the alloy is heated to the upper α - β range, held there and slowly cooled.
2. Duplex annealing improves creep resistance or fracture toughness. It typically consists of solution annealing below T_{β} and subsequent ageing at 320°C ~ 500 °C.
3. Beta annealing heat treatment to improve fracture toughness, characterised by heat treatment above T_{β} followed by slow cooling [13].

3.3. Solution annealing

Solution annealing is a process in which the alloy is heated to an appropriate temperature for a specified time to form the desired component in a solid solution, followed by rapid cooling [5].

The three steps of solution annealing are as follows:

- a) heating the material to a high temperature to bring the alloying elements in the β -phase into solution,
- b) maintaining at this temperature to achieve homogenisation,
- c) rapid cooling to room temperature.

For β titanium alloys, the solution annealing temperature is usually above T_{β} , for ($\alpha + \beta$) alloys it is usually below T_{β} .

3.4. Ageing

Ageing heat treatment is also called precipitation heat treatment. It is a heat treatment process used to increase the yield strength of materials. During ageing, phase precipitation occurs by de-

composition of the β -phase. Through the mechanism of a precipitation, which is finely dispersed in the β matrix, it leads to an increase in the strength of the material.

There are three types of ageing:

- High-temperature ageing,
- Low-temperature ageing,
- Duplex ageing [9].

3.4.1. Ageing at high temperatures

Grain boundaries are the process of decomposition of the β -phase at relatively high ageing temperatures (above 500 °C).

3.4.2. Ageing at low temperatures

Intermediate decomposition products (ω or β' phases) are formed when β -Ti alloys are aged at relatively low (~320 °C) ageing temperatures. If the ageing temperature is particularly low, the transformation takes a long time to complete; the transformation to an equilibrium microstructure consisting of only α and β phases may not be achieved.

The ω phase (hexagonal lattice) causes severe brittleness of the alloy. The coherent ω -particles shear during deformation, causing intense slip localisation and fracture with little or very little ductility.

3.4.3. Duplex ageing

After a rapid cooling (water) following solution annealing (~840 °C) the treatment consists of a long period of low-temperature ageing (~320 °C), followed by a short period of high-temperature ageing (~500 °C). The actual temperature and time chosen for the solution annealing and the two steps should be optimised for the specific alloy composition. The heat treatment results in higher strength and toughness.

3.5. Cryogenic annealing

Cryogenic annealing is the rapid cooling from the homogenizing annealing temperature to -196°C using nitro-gas vapour (boiling point of nitrogen at atmospheric pressure -195,8°C) [14]. This heat treatment significantly increases the ductility of Ti6Al4V alloys (from 5.3% to 8.3%), while the yield strength is reduced by a small amount (2%) [15]. Cryogenic treatment at low temperatures for a long time stabilizes Ti6Al4V alloy by reducing the effect of internal stress, transforming unstable phases into stable phases and improving the mechanical properties and ductility of the material [16].

4. Conclusion

The use of titanium alloys is becoming more widespread despite the fact that they are expensive to produce. Titanium and its alloys have a number of advantageous properties. New alloys are being developed and tested in order to achieve good mechanical, corrosion and wear resistance properties. However, adjusting the chemical composition is not enough, as it is also necessary to create the right microstructure, which can be achieved by heat treatment. In the case of titanium, an alloy-dependent microstructure is formed under equilibrium conditions as shown in **Table 1**. Titanium is an allotropic metal and therefore phase transformations can also occur under equilibrium cooling conditions due to changes in temperature. However, with proper heat treatment, a stable structure can be created which reliably provides mechanical, corrosion resistance and wear resistance properties at the given application temperature.

References

- [1] W. D. Callister, Jr., D.G. Rethwisch: *Materials Science and Engineering. An Introduction*. 10th edition, Wiley, 2018.
- [2] Leyens C., Peters M.: *Titanium and Titanium Alloys: Fundamentals and Applications*. Wiley-VCH Verlag GmbH & Co: Weinheim, Germany, 2003.
- [3] Seward G. G. E., Celotto S., Prior D. J., Wheeler J., & Pond R. C.: *In Situ SEM-EBSD Observations of the Hcp to Bcc Phase Transformation in Commercially Pure Titanium*. *Acta Materialia*, 52/4. (2004) 821–832.
<https://doi.org/10.1016/j.actamat.2003.10.049>
- [4] Tarin P. et al.: *Caracterización de las transformaciones $\alpha \rightarrow \beta$ de la aleación Ti-6Al-4V y de las características mecánicas y microestructurales obtenidas*. *Cerámica y Vidrio*.
- [5] Dipankar Banerjee, J. C. Williams: *Perspectives on Titanium Science and Technology*. *Acta Materialia*, 61. (2013) 844–879,
<http://dx.doi.org/10.1016/j.actamat.2012.10.043>
- [6] Nihal Yumak, K. Aslantas: *A Review on Heat Treatment Efficiency in Metastable β Titanium Alloys: the Role of Treatment Process and Parameters*. *Journal of Materials Research and Technology*, 9/6. (2020) 15360–15380.
<https://doi.org/10.1016/j.jmrt.2020.10.088>
- [7] The Crystal Structure of Titanium. V., 43 [2] 267–272 (2004). (accessed on: 2024. okt. 10.).
<http://www.metalspiping.com/the-crystal-structure-of-titanium.html>
- [8] Semiati S. L.: *An Overview of the Thermomechanical Processing of a/b Titanium Alloys: Current Status and Future Research Opportunities*.

- The Minerals, Metals & Materials Society and ASM International, 51A. (2020) 2020–2593.
<https://doi.org/10.1007/s11661-020-05625-3>
- [9] Pallavi Pushp, S.M. Dasharath, C. Arati: *Classification and Applications of Titanium and Its Alloys*. Materials Today: Proceedings, 54. (2022) 537–542.
<https://doi.org/10.1016/j.matpr.2022.01.008>
- [10] Basic Titanium Metallurgy. (accessed on: 2024. okt. 10.).
<https://usa-titanium.com/basic-titanium-metallurgy/>
- [11] Types of Titanium Alloys and Their Uses
<https://www.refractormetal.org/types-of-titanium-alloys-uses/> (accessed on: 2024. okt. 10.).
- [12] M. J. Donachie (ed.): *Titanium a Technical Guide*, 2nd edition, ASM International, 2000.
- [13] Heat Treating of Titanium and Titanium Alloys
<https://www.totalmateria.com/en-us/articles/heat-treating-titanium-and-titanium-alloys/>
(accessed on: 2024. okt. 10.).
- [14] Tushar Sonar, Sachin Lomte, Chandrashekhar Gogte: *Cryogenic Treatment of Metal – A Review*. Materials Today: Proceedings, 5/11. Part 3, (2018) 25219–25228.
<https://doi.org/10.1016/j.matpr.2018.10.324>
- [15] M. Vijayakumar, A.M. Shanawaz, N. Prabhu, K. Arunprasath, C. Ramesh, Midhun Mohan: *The Influence of Cryogenic Treatment on Titanium Alloys Mechanical Properties*. Materials Today: Proceedings, 66/3. (2022) 883–888.
<https://doi.org/10.1016/j.matpr.2022.04.513>
- [16] Shiteng Zhao et al.: *Cryoforged Nanotwinned Titanium with Ultrahigh Strength and Ductility*. Science 373. (2021) 1363–1368.
<https://doi.org/10.1126/science.abe7252>



SAFETY QUESTIONS CONCERNING MANUAL LASER WELDING

Nagy Balázs Ákos,¹ Gáti József,² Kovács Tünde Anna³

¹ Óbuda University, Bánki Donát Faculty of Mechanical and Safety Engineering, Budapest, Hungary, nagy.balazs@bgk.uni-obuda.hu

² Óbuda University, Bánki Donát Faculty of Mechanical and Safety Engineering, Budapest, Hungary, gati.jozsef@uni-obuda.hu

³ Óbuda University, Bánki Donát Faculty of Mechanical and Safety Engineering, Budapest, Hungary, kovacs.tunde@bgk.uni-obuda.hu

Abstract

Manual laser welding equipment is increasingly used in industry. Unfortunately, the safety regulation of this equipment is not yet fully developed, and in this paper, the authors have attempted to provide a summary study of the safety classes and current standards for laser welding equipment. The harmful effects of laser radiation on the human body (skin, eyes) and the environment are described. The authors also provide protection recommendations on the need to signal the dangers and how to avoid them and summarise the most important rules in ten points.

Keywords: *laser welding, laser safety, diffuse radiation, normal optical hazard distance (NOHD).*

1. Introduction

Today, there are several laser technologies optimised for a wide range of tasks. In some cases, the harmful effects of radiation can be neglected (class 1 and 2 lasers), but in industrial environments with high power densities, the indirect radiation (reflection) in the machining area must be taken into account [1–5]. Radiation has been classified, safety requirements have been laid down in standards (EU: IEC 60825-1; USA: ANSI Z136) and compliance with these requirements is required by law [6]. The radiation safety requirements for lasers are laid down in several standards, and only the requirements of these standards can be applied [4, 7, 8].

The first laser (Theodore Maiman, Hughes Kuta Lake Institute, California, 1960) was a solid-state laser that excited chromium ions in ruby, which contaminated the corundum (Al_2O_3) with photons. Two years later, the first gas laser (William R. Bennett, Don Herriott and Alfonso Arons Hughes Kuta Lake Institute, California, 1961) was born, in which a He-Ne gas mixture was the laser medium, which was raised to higher energy levels by electrical discharge [9, 10].

Soon after the first lasers appeared, the need arose to study the wavelengths and properties

of different laser beams and types. These He-Ne lasers operate in the visible red-light range and were relatively easy to study (using optical prisms), but considerable spectroscopic knowledge was needed to detect the wavelength of each laser. By 1976, in the USA, this knowledge had led to the classification of lasers into categories (ANSI Z136.1: Safe Use of Lasers): four main classes were defined. This American standard was sufficiently permissive that in 1994, in response, the IEC 60825-1 standard was created based on the same classification.

2. Security classes

2.1. Classification according to Standards

The IEC 60825-1 standard takes the following factors into account when classifying laser devices: radiation power (W, mW), wavelength (nm, μm), exposure time (s), type of radiation (continuous mode, pulsed mode). In addition to the four main classes, subclasses are distinguished by a special letter (M).

Class 1 laser devices include those whose wavelength range is not hazardous to human health and which are generally of the closed system type (e.g. CD reader).

Class 1M includes laser devices with wavelengths from 302.5 to 400 nm, which are not dangerous to humans without optical amplification (e.g. laser pointers).

Class 2 includes low power (1 mW) laser devices with wavelengths between 400 and 700 nm. Without optical amplification, they do not require protective equipment, since the automatic blink reflex of the human eye (0.25 s) provides sufficient protection (e.g. laser pointer), the requirements of Class 1 apply.

For Class 2M, the Class 2 guidelines apply, but with the interposition of an optical device, it becomes dangerous to the human eye (e.g.: marking lasers).

Class 3R (3A) laser systems operate at powers between 1 and 5 mW in the visible light wavelength (400–700 nm). During short exposure times ($< 0,25$ s), they do not endanger the human eye, but they can damage the eye through the collecting lens by maintaining the interaction for longer periods. Warning signs and stickers should be placed on such equipment or in the vicinity of the equipment used, and the use of protective goggles is recommended (e.g., medium-power laser cutting machines).

Class 3B is already markedly harmful to the eyes, even in the case of scattered radiation. It is true for these devices that they operate continuously at power levels between 5 mW and 500 mW (e.g.: industrial/medical laser irradiation). The use of protective goggles is mandatory!

Class 4 laser products can cause eye and skin damage and are even a potential fire hazard. Devices exceeding the limits of the previous class are included here, and the use of protective equipment is mandatory (e.g. industrial material processing lasers) [4, 7, 8, 11].

In order to ensure safe operation, it is necessary to become familiar with the properties of the different laser beam properties. We highlight two main groups of lasers for industrial applications: solid-state lasers (in our case, transistors) and gas lasers (usually CO_2 lasers). The formation of the laser beam is schematically illustrated in [Figure 1](#).

2.2. Classification by Wavelength

2.2.1. Solid-state laser

This type of laser uses as a laser medium, a rod, a disc or a glass fiber, which are crystals with excellent refractive index ($\text{Y}_3\text{Al}_5\text{O}_{12}$ /YAG: yttrium aluminium garnet, YVO_4 : yttrium orthovanadate)

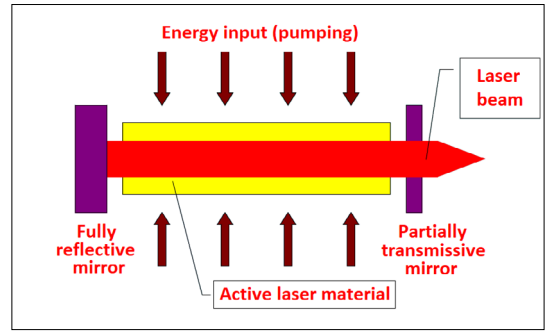


[Fig. 1.](#) Schematic representation of the creation of a laser beam.

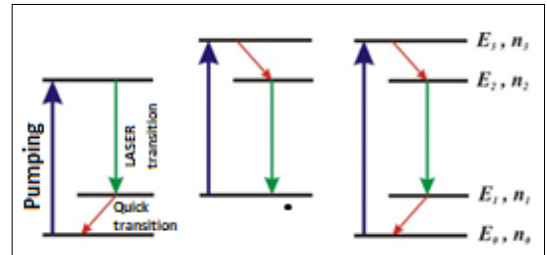


[Fig. 2.](#) Schematic representation of three- and four-level energy systems. [12]

doped with constituents (neodymium, erbium, ytterbium, etc.). Two energy sources are not sufficient for population inversion to occur since the excited particle immediately tends to reach rest, so systems with 3 and 4 energy sources are typical at the population scale ([Figure 2](#)). To date, it is true that this type of lattice is usually equipped with Nd: YAG crystals, in which neodymium ions (Nd^{+3}) are excited to the highest energy level of the system by diode lattices emitting at 808 nm. This is followed by a radiation-free transition, during which the vibrational energy of the crystal lattice is much lower than the energy of the system, resulting in a typical photon beam with a wavelength of 1064 nm. In order to maintain the laser radiation as a circular flux, the neodymium ions have to be brought from the lower energy level of the emission to the so-called hegemonic state in order to bring the active laser beam back down to the highest energy level of the system [1, 5, 10].

2.2.2. CO_2 lasers

In industrial machining, an airy laser medium can be used, usually carbon dioxide (CO_2) for high power density requirements. The gas medium is contained in a quartz glass tube and is excited by

an electric field (DC high-frequency excitation). The CO₂ laser operates between the vibration levels of the carbon dioxide molecule. It is the most powerful gas laser and has the highest efficiency (15-20%). The laser medium is a mixture of CO₂, N₂, He or H₂O vapour in a ratio of about 1:1:8. Four-energy arc system: a large number of N₂ molecules is excited by gas discharge, enriched in a long-lived, metastable state, and then energy is transferred to the carbon dioxide molecules by collision. A laser transition is created between their two vibrational states, typically with a wavelength of 10600 nm that can be coupled. Helium gas or water vapour helps to empty the lower laser nozzles during energy transfer (collisional energy transfer) [1, 10].

The excitation induces electromagnetic radiation of different wavelengths depending on the laser beam, which may pose a hazard to human health if the operator is inside the work area. In the following, only protection against scattered radiation will be discussed.

3. Risk areas

3.1. Eyes

The eye is the most sensitive organ of the human body to radiation, and suitable protective equipment must be provided during work. **Figure 3** shows how the eye reacts to certain types of radiation.

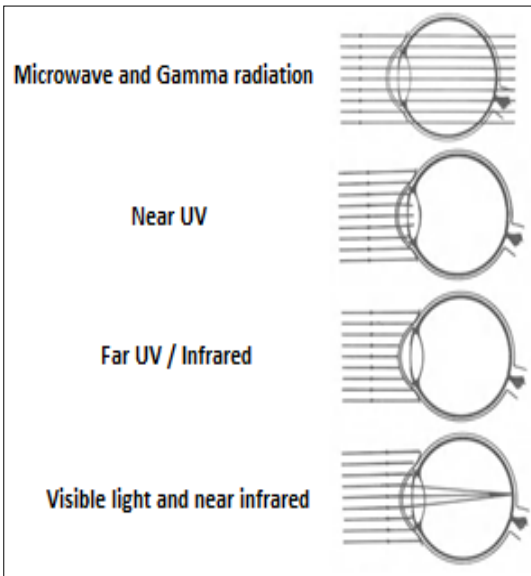


Fig. 3. Behaviour of the human eye to certain types of radiation, schematic diagram.

General case:

$$NOHD = \sqrt{\frac{4 \cdot P \cdot \alpha}{\pi \cdot MPE \cdot \omega_0^2}} = (m) \tag{1}$$

In the case of multimode optical fiber:

$$NOHD = \sqrt{\frac{1,79}{NA}} \cdot \sqrt{\frac{P}{\pi \cdot MPE}} = (m) \tag{2}$$

where:

- *P* is the laser power (W),
- α is the beam divergence (rad),
- ω_0 is the initial beam radius (m),
- *MPE* is the maximum permissible exposure (W/m²),
- *NA* is the numerical aperture .

Glasses with different refractive index lenses have been designed to protect the eye depending on the wavelengths to which it is exposed. The most widely used standard for such products is MSZ EN 207:2020, but there is an American equivalent (AISI Z136.3), but this standard only specifies the optical density of the glasses, the European one is much stricter. It can be said that there is no product on the market that can be used safely at all wavelengths, so the protective device must be selected for the specific laser machine. In order to ensure protection, it is necessary to be able to determine the safety class of the glasses.

Such devices are tested before they are put on the market, in order to determine the most important metric, the optical density, which indicates their effectiveness against radiation. It is true that the higher this value, the more effective the protection against the radiation, but it is worth determining the minimum safety level, as the cost increases with the optical density. Knowledge of the wavelength, power, beam diameter and mode of operation is required. With this in mind, we can use the table in EN 207:2020 to work out the minimum safety level required to ensure safe operation. In the documentation for safety goggles, there is a diagram showing the transmittance and optical density at each wavelength, so safety equipment must be chosen accordingly. It is advisable to define the normal danger distance (NOHD), which should be communicated to the operator and enforced (1), (2) [2, 7].

3.2. Skin

Human skin protects us from the dangers of the environment, but it is less effective against this artificial exposure. Radiation at different wavelengths can penetrate deeper into human skin,

and these will have their own specific damage mechanisms. As shown in **Figure 4**, there are two cases where there is a big difference: the wavelength of the CO₂ laser penetrates the epidermis, our skin is damaged by thermal conduction, can overheat and possibly coagulate (irreversible).

The small wavelengths of radiation from solid-state lasers reach the deepest layers of our skin, where they evaporate the water in our skin. In addition to the water in the capillaries, there is also iron in our blood, which readily absorbs this wavelength (**Figure 5**). The superheated iron atoms explode and the 'slag' in the bloodstream can then clog capillaries (particularly in the eyes, which have the thinnest vessels).

In order to avoid these hazards, all parts of the body must be covered and the protective clothing material must absorb the radiation present without damage. Because of the long wavelength of CO₂ laser light, conventional welding clothing (cowhide) provides sufficient protection, while other special materials (composites) must be used to protect against solid-state laser radiation. It is essential to make sure that protective equipment is able to perform its function [3].

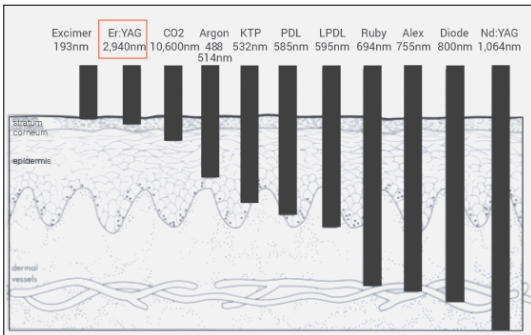


Fig. 4. Schematic representation of penetration depths of various laser beams into human skin. [14]

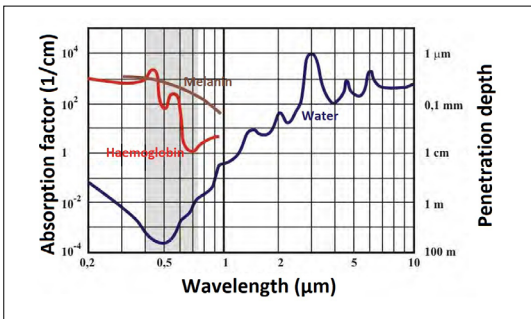


Fig. 5. Behaviour of fluids in the human body (skin) under various laser radiation types. [15]

3.3. Environment

Aware of the damaging effects of laser light, the work area must be insulated from the outside world, and suitable materials must be chosen depending on the wavelength of the radiation. The aim is to prevent radiation from escaping: either reflection or absorption of the radiation can be the basic principle. If the latter is chosen, since the device is used indoors, Plexiglas (PMMA) offers protection against CO₂ lasers but is transparent to near-infrared waves. For this wavelength, special enclosures, special sandwich panels (graphite between Al-plates), and reflective building elements coated with an absorbing layer on the inside (painting, coating, fixing of other material panels) can be used as a cost-effective solution. Special attention must be paid to the absorption of radiation from the area towards which the light source is directed (thicker light absorbing layer). It is advisable to choose a door design that can operate a safety switch, because only in an enclosed space can laser light be coupled. For safety reasons, anyone outside the work area should be able to see into it in case of a possible complication during the operation of the laser source. For this purpose, windows are available in a similar way to spectacles, for which the control principles for the choice of the spectacle lens apply. The extraction of airborne metal in the environment must be ensured. For material handling reasons, it is advisable to follow LEAN principles to avoid mechanical injuries, and hazard warnings and obligations (e.g. wearing protective clothing) should be displayed (**Figure 6**) [6].



Fig. 6. Pictograms representing obligations and hazards.

4. Safety Recommendations in the NIR Range

The Bánki Donát Faculty of Mechanical and Safety Engineering at Óbuda University plans to install a handheld laser welding machine, which is a fiber laser welding device, with the support of CLOOS Hungary Crown International Kft. Its most important characteristic is that the laser medium is a solid-state material with an increased specific surface area (thin fiber), a maximum power of 2000 W, and it operates at a wavelength in the near-infrared range (1080 nm, or 1070 ± 20 nm) according to the manual). This wavelength range can be dangerous for the machine operator, as 17% of the radiation can penetrate the deepest layer of human skin (the hypodermis), potentially causing the damages discussed previously. What exacerbates the problem is that this radiation can "burn out" the optic nerves of the human eye, creating blind spots for the operator (an irreversible process). Because of these dangers, individual and environmental safety must be ensured. As a solution, safety goggles with a specific safety factor will be selected from specialists, as it is not advisable to economize on this because the brightness of our eyes can be at stake, e.g. Laservision, UVEX, and NoIR [16, 17]. In terms of clothing, fabrics containing metal fibers (stainless steel, silver) should be chosen, which are also ergonomic. Jackets and trousers from ISA Technology are recommended, as they protect against radiation and heat effects [18]. Gloves made of white-pigmented materials are popular due to the reflectivity of titanium dioxide (TiO_2) [2, 7]. The product named "Guide 70" is widely used by those engaged in handheld laser welding [20]. In terms of footwear, safety work shoes can be applied. The environment can be designed in a cost-effective way, with sliding doors being used to operate the safety interlock. Lasers operating in the near-infrared range typically release metal vapours; in this respect, industrial ventilation and air purification systems are sufficient.

5. Conclusion

Nowadays, the increasingly popular handheld laser devices pose a danger to the machine operator, as they are in the same enclosed space. Even industrial lasers have their work areas enclosed to protect the operator. When using handheld units, those within the working area are protected by safety clothing, while those outside the area are safeguarded by hermetically sealed enclosure

1. **Never look directly into the laser beam.**
2. **Never aim the beam at another person.**
3. **Do not view Class 3R or higher-powered lasers through optical instruments.**
4. **Operate lasers only in designated areas.**
5. **Position the beam path well above or below eye level for both standing and seated positions.**
6. **Always use diffuse reflective beam guards.**
7. **Remove all reflective objects, such as jewelry or tools, from the beam path.**
8. **Only authorized personnel may enter areas with Class 3B and 4 lasers.**
9. **Always wear laser safety glasses when exposed to Class 4 invisible radiation.**
10. **Always implement safe configurations.**

Fig. 7. Principles for Injury-Free Laser Operation. [21]

elements. Such devices are "cheap" and easy to acquire, capable of performing multiple tasks (such as cleaning lasers); however, the belief that they are risk-free is a misconception. We must familiarize ourselves with these devices and perform risk assessments of the hazards to ensure, with high expertise, the safe operation of laser equipment. Finally, we must strive to comply with the rules shown in Figure 7 to avoid injuries.

References

- [1] Christopher Dawes: *Laser Welding*. Abington Publishing, Cambridge, 1992.
- [2] David Sliney, Myron Wolbarsht: *Safety with Lasers and Other Optical Sources*. Springer Science+Business Media, New York, 1980.
- [3] Halász G.: *Kézi lézeres berendezések biztonságos használata*. Hegesztéstechnika, 35/1. (2024), 41–47.
- [4] Bagyinszki Gy.: *Lézerek alkalmazásának technológiai és biztonságtechnikai szempontjai*. XI. Nemzeti és IV. GTE-MHtE-DVS hegesztési Konferencia, Budapest, 2004, 14–30.
- [5] Bitay E.: *Lézeres felületkezelés és modellezés*. Erdélyi Múzeum-Egyesület, Kolozsvár, 2007. <https://doi.org/10.36242/mtf-04>

- [6] 2012. évi I. törvény a munka törvénykönyvéről: 51. § és 86. §
- [7] Ken Barat: *Laser Safety: Tools and Training*. Second Edition, Taylor & Francis LTD, Broken Sound Parkway, 2017.
- [8] Bagyinszki Gy., Bitay E.: *Lézeres anyagmegmunkálás veszélyessége*. Műszaki Tudományos Füzetek - FMTÜ, 18. (2013) 51-56.
<https://doi.org/10.36243/fmtu-2013.05>
- [9] Kovács Z.: *A lézerek működési alapjainak és a lézersugárzás alkalmazásainak tanítása*. Doktori értekezés, József Attila Tudományegyetem, Szeged, 1995.
- [10] Buza G: *Lézersugaras technológiák I.*, Edutus Főiskola. Budapest, 2012.
- [11] California Institute of Technology: *Laser Safety Manual*. Caltech Environmental Health and Safety Office, California, 2023.
- [12] Online tananyag: *Lézerek az Orvostudományban, Szegedi Tudományegyetem*.
https://titan.physx.u-szeged.hu/tamop411c/public_html/Lezerek_az_orvostudomanyban/23_a_polulciinverzi_s_energiaszint_smk.html (2024)
- [13] Seiji Katayama: *Handbook of Laser Welding Technologies*. Woodhead Publishing Limited, Cambridge, 2013.
- [14] <https://wtlaser-en.com/144> (2024)
- [15] Buza G.: *Lézersugaras technológiák tegnap, ma, holnap*. Nagy energiasűrűségű ankét, Magyar Hegesztési Egyesület, Kecskemét, 2023. október 26., előadás-prezentáció.
https://maheg.hu/wp-content/uploads/2023/11/Buza_Nagy_energiasurusegu.pdf
- [16] <https://www.uvex-laservision.de/> (2024)
- [17] <https://www.noirinsight.com/> (2024)
- [18] Meszlényi Gy., Bitay E.: *The Role of Focus Position in Single Pulse Laser Drilling of Highly Reflecting Materials*. Acta Materialia Transylvanica, 2/1. (2019) 61–68.
<https://doi.org/10.33924/amt-2019-01-10>
- [19] <https://www.isatechnologies.com/> (2024)
- [20] <https://guidegloves.com/> (2024)
- [21] Tóth László: *A kézi lézeres hegesztőgépek biztonságtechnikája*. Nagy energiasűrűségű ankét, Magyar Hegesztési Egyesület, Kecskemét, 2023. október 26. előadás-prezentáció.
https://maheg.hu/wp-content/uploads/2023/11/Lezervedelem_PPT_MDTL-231026-Nagy_energiasurusegu_Anket.pdf



NUMERICAL MODELLING OF WEB CRIPPLING UNDER REALISTIC END SUPPORT CONDITIONS

Örs NAGY,¹ Annabella SÁNDULY,² F.-Zsongor GOBESZ³

¹ *Technical University of Cluj-Napoca, Faculty of Civil Engineering, Doctoral School, Cluj-Napoca, Romania, rsnagy8@gmail.com*

² *Lodz University of Technology, Faculty of Mechanical Engineering, Department of Strength of Materials, Lodz, Poland, annaberlla.sanduly@gordias.ro*

³ *Technical University of Cluj-Napoca, Faculty of Civil Engineering, Department of Structural Mechanics, Cluj-Napoca, Romania, go@mecon.utcluj.ro*

Abstract

Determination of web crippling resistance of thin-walled steel sections can be achieved by two different methods: by laboratory experiments or with numerical models, dividing the geometry into finite elements. Trapezoidal sheeting is particularly sensitive to concentrated loading. The support conformation has a significant influence on the resistance of the profile. Understanding the influential support parameters and taking into account in calculations is essential, since it can have a major influence on the bearing resistance and failure mode. The American and the European standards differ in their approach regarding the boundary conditions. The Eurocode does not consider the fixing of the sheets to the roof purlins or beams, which is generally applied in the construction industry. The present study investigates the web crippling resistance of trapezoidal cross-sections with numerical finite element models for several support configurations, considering also the influence of bottom flange fixing.

Keywords: *cold-formed steel, trapezoidal sheeting, web crippling resistance, Eurocode, finite element model.*

1. Introduction

1.1. Web crippling of cross-sections with multiple webs

The failure modes of thin-walled sections include the local buckling of the web under concentrated shear forces, namely the web crippling. Deep trapezoidal profiles are especially sensitive to the studied failure type, because of the thin (0.3–1 mm), but high (up to 150 mm) web plate subjected to shear. The transversal force resistance of web can be less than the bending resistance of the whole profile.

In case of roof sheeting or decking of composite slabs, the main applications of trapezoidal sheets, usually the highest shears are concentrated at the supports. In design practice is extremely important to use the real parameters of the bearings. The length of the sheet-to-support contact surface and the length of the free end in console has a significant influence on the web crippling

resistance. With adequate support conformation a design capacity can be achieved that is not determined by the web crippling failure.

1.2. End support conformations

In practice, deep sheets are mostly used as roof decking, for increased distance between the supports. The general characteristics of the bearing supports differ based on the materials used for the primary structure and the design details. The upper plane of the concrete purlins generally does not follow the roof angle. As a consequence, the sheet-to-purlin contact is a theoretical line. At the ridge support, the trapezoidal profile has a cantilever free end (**Fig. 1**).

The orientation of steel purlins can follow the roof angle, but there are cases when their upper plane remains horizontal.

The cantilever length of trapezoidal profiles at eave support can be variable (**Fig. 2**). In many cases the designer does not give any specification concerning the end length.

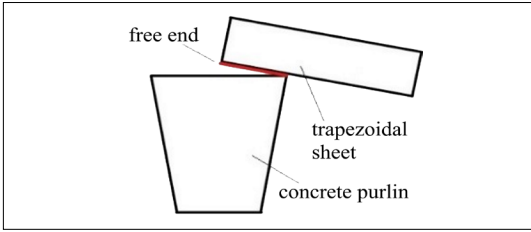


Fig. 1. Typical ridge support for concrete purlins.

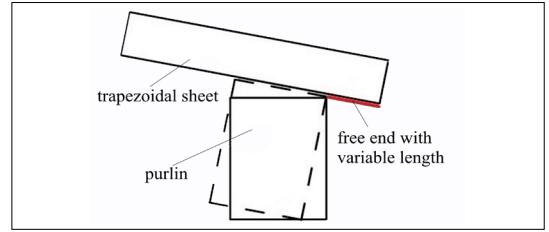


Fig. 2. Eave supports for concrete and for steel roof purlins.

End supports differ in two main parameters. One is the bearing surface's length that can be the width of the bearing element's upper flange or a narrow edge for inclined supports. The second parameter is the length of the sheet portion being in console. The present study does not inspect the web crippling resistance at intermediate supports.

2. Particularities of analytical calculations

2.1. AISI Standard

The investigation of web crippling resistance of steel sections began in the 1940's at Cornell University, with the set of experiments conducted by Winter and Pian [1], in which they studied back-to-back lipped channels, under 4 different loading types: IOF – interior one-flange loading, EOF – end one-flange loading, ITF – interior two-flange loading and ETF – end two-flange loading (Fig. 3).

The standardization of the laboratory experiments was carried out by LaBoube and Schuster [2], which has been included in the AISI S909-17 [3].

It is still common to determine the concentrated shear resistance of the web by testing, since the failure of thin-walled sections is caused by several factors acting simultaneously [4]. Several test sets were done with various cross-sections. The analytic relation (1) of the AISI S100-16 [5] was developed based on the empirical results [6]. The code defines the web crippling resistance in function of the following parameters: sheet thickness (t), yielding strength (F_y), slope of the web (θ), inner bending radius (R), bearing length – length of contact surface between the profile and the support (N), web height (h).

$$P_n = Ct^2F_y\sin\theta \left(1 - C_R\sqrt{\frac{R}{t}}\right) \left(1 + C_N\sqrt{\frac{N}{t}}\right) \left(1 - C_h\sqrt{\frac{h}{t}}\right) \tag{1}$$

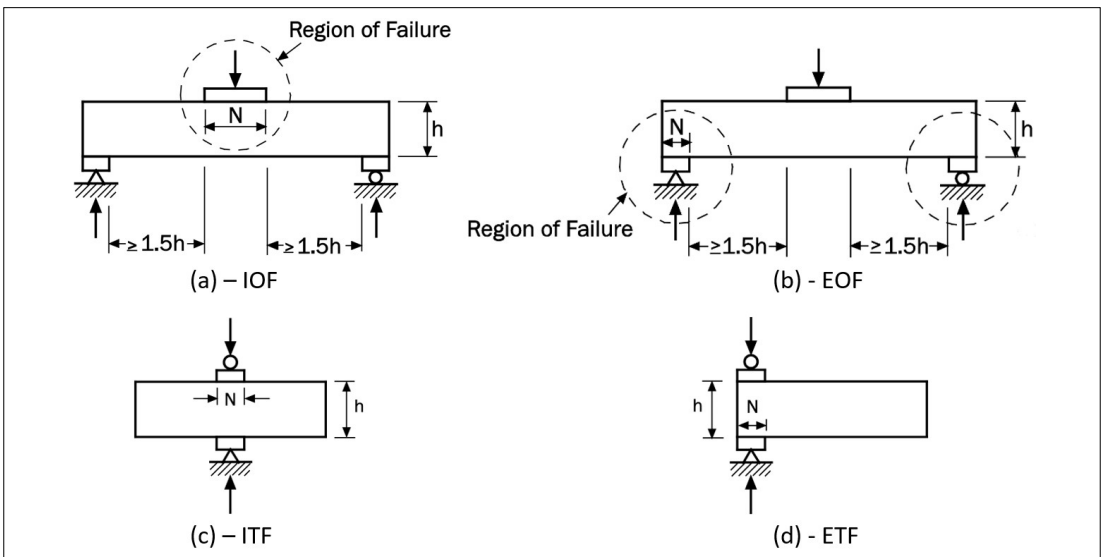


Fig. 3. Distinguished loading types (source – AISI S909-17 [3])

time, only half of a rib was introduced in the FE model, while on the longitudinal sides symmetry boundary conditions were applied. Close to the imposed load, the profile lies on an inclined steel plate and on the opposite side a hinge is provided. Loading is introduced as a vertical displacement transmitted to the bottom flange, that is increased with each time increment (Fig. 7).

The mesh formulation follows the expected distribution of the deformations. The mesh is refined where larger displacements can take place. In the end zone, the indicated size of the finite elements is 3 mm, on the load-transfer portion is 6 mm and on the remaining segment is 10 mm. The meshing is quadrilateral dominant and second order SHELL281 finite elements were used. The contour of the rounded corners was divided into 4 segments.

The measured yield strength of 362.8 MPa was considered. For the numerical analysis a bi-linear material model was used for the steel elements. The elastic zone had a Young's modulus of $E = 210$ GPa, while the plastic zone of $E = 2.1$ GPa. Instead of the $t = 0.75$ mm design thickness, the measured mean thickness of the base material of $t_{real} = 0.684$ mm was introduced in the calculation. (Fig. 8)

The finite element model was validated on the GRISPE project's [9, 10] experiments. The web crippling resistance obtained with the model differs by 0.23% from the experimental value, while the second load maximum in the post-elastic domain is less by 13.34% than the measured one [11]. The deformed shape and the failure mode identified with the FE model correspond to those observed in the laboratory.

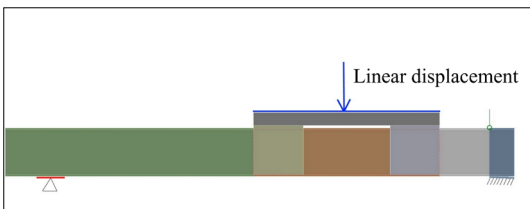


Fig. 7. Boundary conditions

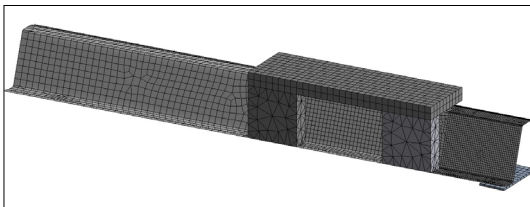


Fig. 8. Meshing

4. Results

In the recent European experiments [10, 13] trapezoidal profiles were not connected to the support, while in the construction practice a sheet-to-purlin or sheet-to-beam fixing is always present. This chapter compares the web crippling resistance of fastened and unfastened ends for variable end lengths in console. The investigation of the fixing's influence at intermediate supports is less relevant. In general there is no loading condition that tends to separate the bottom flange of the trapezoidal profile from the bearing.

The rigidity of the screw and the washer is increased compared to the sheet. Tension forces lead to significant deformations only on the bottom flange of the thin-walled profile. To reduce computational time only, the effect of the fastener was introduced in the Ansys model. The bottom flange was bonded to the support at a circular perimeter, equal to the dimension of the washer.

4.1. Short consoles

Unfastened short ends tend to rotate around the inner edge of the support, causing an upward movement of the bottom flange. The phenomenon was observed both in the experiments and in the numerical simulations. Stress concentrations appear at the contact point between the sheet's web and the support's edge.

Fastening of the end constrains the rotation of the end section and changes the stress distribution. The stresses are concentrated along the whole contact edge between the rounded bottom corner and the support. Fig. 9 presents the deformed shape and Fig. 10 the stress distribution of the following conformation: support width (l_{sb}) 40 mm, free end length (l_{end}) 0 mm.

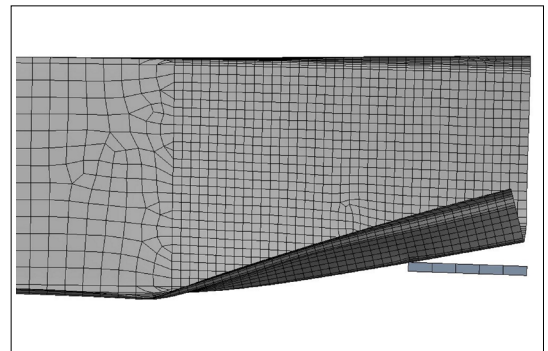


Fig. 9. Typical deformation of short consoles, without fastening.

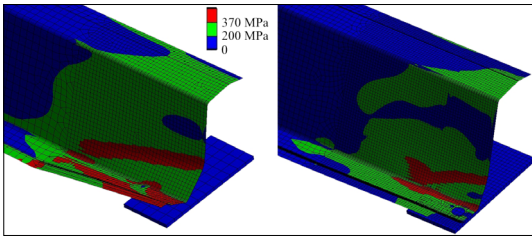


Fig. 10. Stress distribution at short ends, without fastening (left) and with fastening (right).

4.2. Long consoles

In the case of long free ends, the concentrated support reaction tends to have a more local-like effect. The end section of the profile does not deform, the behavior of the cross-section becomes similar to that in the case of loads applied in the field.

Fig. 11. shows the deformed shape and stress distribution of the PCB 80 cross-section having 80 mm end length, with and without fastener. The behavior of the profile is similar in both cases. It can be noticed that for the fastened configuration the stresses are more symmetric to the support.

4.3. Effect of fasteners on the web crippling resistance

The force-displacement curves for the fastened and unfastened ends were compared for variable end lengths. For short ends, the fixing significantly influences the bearing resistance. The effect of the fasteners for long consoles is neglectable.

In terms of numbers (Fig. 12), for short consoles (AISI – EOF, EN – category 1), the presence of fastener led to a 20-23% increase in the section’s resistance to web crippling, which corresponds to the difference provided by the AISI S100-16 calculation. For long ends (AISI – IOF, EN – category 2), sheet-to-support fixing is insignificant, which is in accordance with the American standard. (Table 1.)

5. Conclusions

For the determination of the true web crippling resistance of trapezoidal cross-sections it is essential to know the real support parameters. The validated finite element models show that for end configurations with short consoles, fasteners have a significant influence on the profile capacity, which is considered in the American standard.

The Eurocode does not give guidance regarding the studied parameter, which leads to underestimation of the sheet capacity for concentrated loads. The authors consider it important for struc-

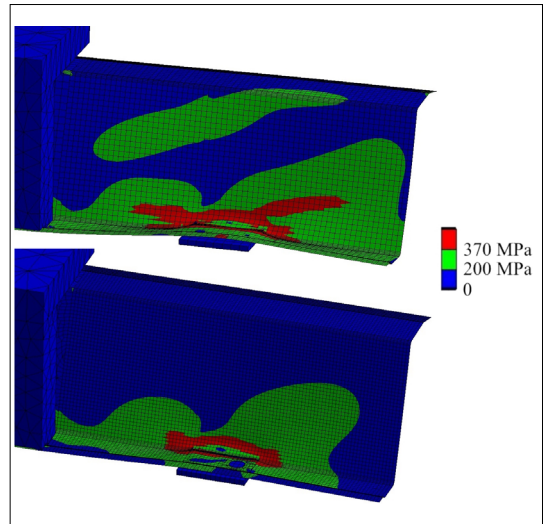


Fig. 11. Stress distribution at long ends, unfastened (above) and fastened (below).

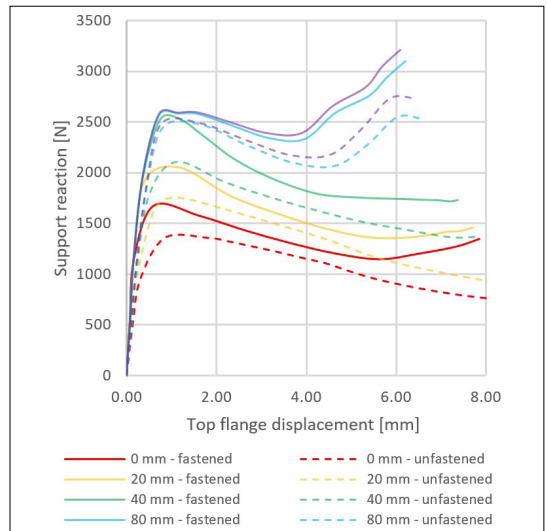


Fig. 12. Force-displacement curves from the numerical simulations for increasing free end lengths with and without fastening.

Table 1. Changes in web crippling resistance due to fasteners for variable free end lengths

l_{end}	$R_{w,Rd}$ without fastener [N]	$R_{w,Rd}$ with fastener [N]	Influence of fixing [%]
0	1360	1672.7	22.99
20	1747.9	2104.7	20.41
40	2105.6	2528.5	20.08
80	2479.3	2580.6	4.09
160	2489.6	2592.5	4.13

tural engineers to be aware of the significance of providing proper support details.

In the future, we will propose the revision of the relevant chapter of the Eurocode, to take into account the effect of sheet-to-support fasteners on the web crippling resistance of thin-walled steel profiles with multiple webs.

Acknowledgments

The research was supported by the Collegium Talentum Grant of Sapientia Hungariae Foundation and by the Engineering Department of Márton Áron Professional College of the Eötvös Loránd University.

References

- [1] Winter G., Pian R. H. J.: *Crushing Strength of Thin Steel Webs*. Engineering Experiment Station Bulletin, 35/1. (1946) New York, USA.
- [2] LaBoube R., Schuster R.: *Standard Test Method for Determining the Web Crippling Strength of Cold-Formed Steel Members*. Research Report RP02-6, American Iron Steel Institute, USA, 2002.
- [3] AISI S909-17: Test Standard for Determining the Web Crippling Strength of Cold-formed Steel Flexural Members, 2017.
- [4] Macdonald M., Heiyantuduwa M. A., Harrison D. K., Bailey R., Rhodes J.: *Literature Review of Web Crippling Behavior*. Proceedings of the 2nd Scottish Conference for Postgraduate Researchers of the Built and Natural Environment (PRoBE), 2005, Rotterdam, Netherlands, 473–482.
- [5] AISI S100-16: North American Specifications for the Design of Cold-Formed Steel Structural Members, 2016.
- [6] Dwivedi R., Vyavahare A.Y.: *Review: Web Crippling Behavior of Cold-Formed Beam Sections*. Structures, 33. (2021) 4629–4641. <https://doi.org/10.1016/j.istruc.2021.07.042>
- [7] EN 1993 1-3: Design of Steel Structures – Part 1-3: General Rules – Supplementary Rules for Cold-Formed Members and Sheeting, 2006.
- [8] Misiek T., Belica A.: *Calibration of European Web-Crippling Equations for Cold-Formed C-and Z-Sections*. Steel Construction, Design and Research, 12/1. (2019) 31–43. <https://doi.org/10.1002/stco.201800006>
- [9] GRISPE WP1: Background Guidance for EN-1993-1-3 to Design of Sheeting with Embossments and Indentations, 2015.
- [10] GRISPE: Test Report of Steel Trapezoidal Sheeting with and without Embossments and Outward Stiffeners, Annex, 2015.
- [11] Nagy Ö.: *Influence of End Support Configuration on Web Crippling Resistance of Trapezoidal Profiles*. MS thesis, Technical University of Cluj-Napoca, 2021, Cluj-Napoca, Romania.
- [12] Sánduly A.: *Web Crippling in Deep Trapezoidal Sheeting*. MS thesis, Universitat Politècnica de Catalunya, 2020, Barcelona, Spain.
- [13] Ádány S., Kachichian M., Kövesdi B., Dunai L.: *Experimental Studies on Deep Trapezoidal Sheeting with Perforated Webs*. Journal of Structural Engineering, 139/5. (2013) 729–739. [https://doi.org/10.1061/\(ASCE\)ST.1943-541X.0000593](https://doi.org/10.1061/(ASCE)ST.1943-541X.0000593)



AIR VELOCITY MEASUREMENTS IN THE OFFICES OF THE FACULTY OF ENGINEERING

Bíborka NÉMETH

University of Debrecen, Faculty of Engineering, Debrecen, Hungary. bibike.nemeth@gmail.com

Abstract

During renovations in various areas of the Engineering Faculty, fan coil and split air conditioning units have been installed. These devices have significantly improved the indoor environment quality during the summer season. However, if the indoor units are not properly positioned, they can exert several negative effects on the comfort of occupants and the quality of the indoor environment. Furthermore, improperly selected indoor units can increase installation and operational costs.

As a conclusion we can say that a correctly positioned and selected air conditioning unit can help maintain optimal indoor environmental conditions, while improperly chosen or positioned equipment can adversely affect occupants' comfort and increase operational costs.

Keywords: *air velocity measurement, Testo 400, comfort.*

1. Introduction

People spend 80...90% of their lives in closed spaces. In order to be in a pleasant atmosphere in a building, we require comfort. However, humans make use of more and more glazed surfaces, which causes an increase in summer heat load on one side and, as a consequence, the drastically increase of cooling load on the other side. [1] The glazed building envelope is becoming an important component of contemporary architecture. Glass allows natural light, offers a visual communication with the outdoors, reduces structural load and enhances the aesthetic appearance of buildings. With the many benefits that glazing offers the occupants and the designers, it is not free of problems if it is not properly selected. The building envelope and its glazed fenestration represents a major source of unwanted heat, solar gain and thermal discomfort. Moreover, glazed curtain walls cause glare problems and increase the energy consumption required for cooling systems due to the high internal air temperature. This has resulted in a complete reliance on mechanical means to manipulate the indoor temperature and finally to achieve the thermal comfort at high energy consumption [2]. Hungary has a continental climate, with hot summers and low

overall humidity levels but frequent rain showers and mildly cold snowy winters. Average annual temperature is 9.7°C. Temperature extremes are about 42°C in the summer and -29°C in the winter. (Wikipedia) Since July is the hottest summer month in Hungary I analyzed the interior temperature fluctuation during a specific day of this month in different rooms of a building. [1] Internal temperature in detached buildings varies during the day depending on the external temperature, orientation of the facades, glazed area and thermophysical properties of the opaque building elements. [3] The natural ventilation helps to temper the building structure, which greatly reduces the risk of overheating in the building during the summer period.

In summer the natural ventilation is through windows, which highly depends on prevailing winds and on the temperature difference caused by sunshining, on different parts of the building, so we cannot regulate the quantity of the entering air. [4]

The eastern-facing facade of the Faculty of Engineering has been renovated, and over the years, several expansions have been made to the complex. I had the opportunity to record the internal air velocity in various rooms during the summer period.

2. Introduction of the building

The University of Debrecen, Faculty of Engineering's building can be found in Ótemető street, 2-4, Debrecen. (Fig. 1, Fig. 2) The building complex includes, the educational part, the workshops, the laboratories and the college with 270 living accommodations. In the educational part of the building is placed the Faculty's restaurant served by a 500-dose cuisine. The educational building has five floors (Ground floor + 4 floors), but the third and the fourth level floor space differs from the other levels. [1]

Floor plan of the third-floor offices and split air conditioners installed after the building's HVAC renovation. (Fig. 3)

On the third floor of the old wing, there are 9 offices with different layouts, as illustrated in Fig. 4.

During summer months, Dr. Csáky Imre and Dr. Kalmár Ferenc presented thermal imaging in their article "Indoor temperature monitoring in

east orientation offices," revealing surface temperatures (up to 49.3 °C) contributing to high air temperatures within the offices. (Fig. 5, Fig. 6) [5]

The office air temperature reached its peak between 10-11 am, as high as 37 °C. (Measurements ranged from 31-37 °C during a summer day.) [5]

In those spacious offices, where artificial ventilation is not feasible, alternative measures need to be taken during operating hours. Therefore, the building management implemented the following measures: Split air conditioners were installed in the rooms of the old wing. In the renovated wing, fan coil units were installed. In those areas where neither split air conditioners nor fan coil units were installed, desk and tower fans are used by occupants during the summer months.

According to the MSZ CR 1752:2000 standard, in large office spaces, the average air velocity in the occupancy zone is 0.18 m/s for comfort category A, 0.22 m/s for comfort category B, and 0.25 m/s for comfort category C. [6]



Fig. 1. Satellite image of the Faculty of Engineering. (Google Maps)



Fig. 2. Eastern wing of the Faculty of Engineering.

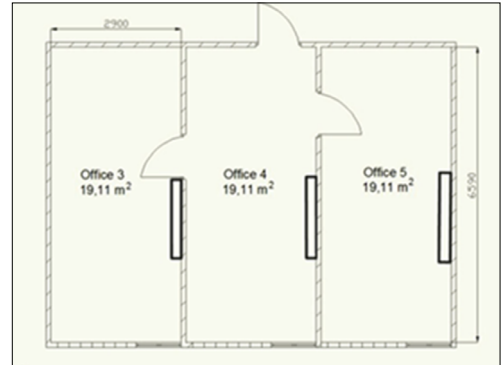


Fig. 3. Office floor plan with split air conditioners. [1]

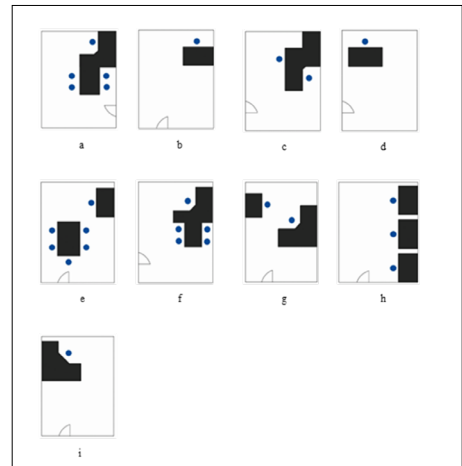


Fig. 4. Office layouts at the Faculty of Engineering.

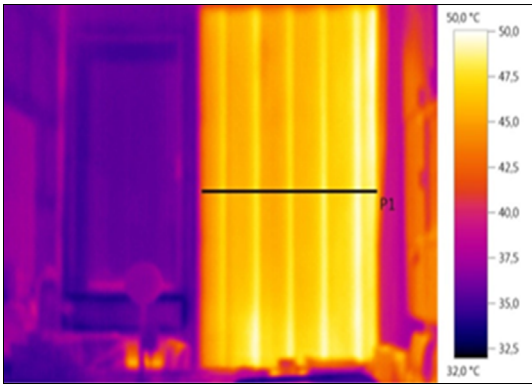


Fig. 5. Thermal image [5]

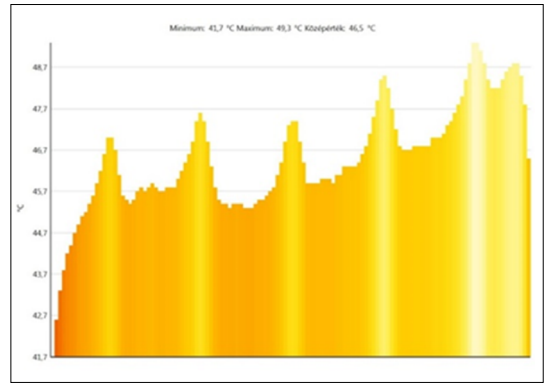


Fig. 6. Temperature distribution. [5]

3. Introducing the Measurement Instrument

During my measurements, I used the Testo 400 climate and air conditioning measuring instrument and Testo turbulence probe. (Fig. 7, Fig. 8)) The air velocity experienced indoors has an impact on thermal comfort. Turbulence intensity is expressed as a percentage and calculated based on the average air velocity and air temperature prevailing in the room. Turbulence intensity reflects the temperature fluctuations occurring within the indoor space and the intensity of air movement. There is a direct correlation between air temperature and measured turbulence intensity. [7] The climate and air conditioning measuring instrument, with its built-in measurement assistant, provides optimal support for conducting air velocity and thermal comfort measurements according to standards, as well as for examining and adjusting ventilation and air conditioning systems. [8]

The Testo turbulence probe can measure independent of direction and simultaneously calculate turbulence intensity and draft risk according to EN ISO 7730 / ASHRAE standards. To ensure precise measurement results, it compensates for air density using built-in absolute pressure measurement. Draft restricts comfort and is the most common cause of indoor air-related complaints. The probe is ideally suited for determining turbulence intensity and draft risk typical in workplaces. Turbulence intensity corresponds to the degree of fluctuation in air velocity over time. It is necessary for determining draft risk. [9] The climate and air conditioning measuring instrument provides optimal support for conducting air velocity and thermal comfort measurements according to standards, as well as for examining and adjusting ventilation and air conditioning systems, with its built-in measurement assistant features a high-precision, location-independent, built-in differential pressure sensor. It can meas-

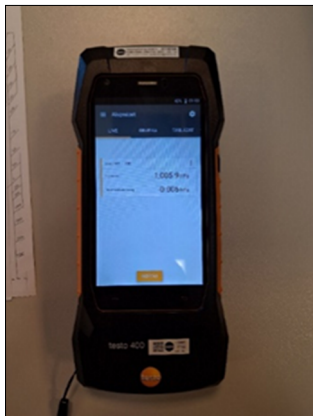


Fig. 7. Testo 400



Fig. 8. Testo turbulence probe

ure all IAQ parameters: air velocity, temperature, humidity, pressure, illumination, radiant heat, turbulence intensity, CO₂ and CO. [10] Among these, I examined air velocity, temperature, turbulence intensity, and draft ratio during my measurements.

4. Measurement

I performed my measurements at two locations: in actual offices and in the laboratory. In the offices, I carried out measurements with split air conditioners and fan coils. In the Air Conditioning and Air Ventilation Laboratory, measurements were carried out by using fans to simulate office spaces. Laboratory measurements were necessary because the walls are painted black to make smoke from the fans clearly visible. Smoke was used to demonstrate how the outgoing air arrives at the point of interest. (Fig. 14 and 16)

4.1. Measurements with split air conditioners

I performed my measurements at five points in the office depicted in Fig. 9 (magnified view of Fig. 4/a), at two specific heights: 1.7m and 1.1m. These correspond to the standing person's head height and the seated person's neck height, respectively. I chose point 5 as the specific location since it is where the desk computer is located, and where occupants spend most of their time.

I designated Position 2 as the most unfavorable location since it has the highest air velocity, which even on the lowest setting exceeds the comfort criteria by more than twice. I organized the measured results into a table, where it is evident that the air velocity does not correspond to the comfort categories. (Table 1.)

The offices are equipped with Midea split-type air conditioners. Their cooling capacity is 4982 W, and their heating capacity is 5275 W. The maximum operating pressure under suction is 1.5 MPa, and under pressure is 4.2 MPa. The nominal power consumption is 2200 W. (Fig. 10)

4.2. Measurements with tower fans

I performed measurements in the climate and air conditioning laboratory, where I set up the room to simulate the office layout. I examined a section of the offices where one person is seated at a desk and adjusts the fan according to their own preferences. (Fig. 4/b, d, g)

Fig. 11 illustrates the position of the equipment relative to the individual. According to standards for comfort measurements, it is necessary to measure at four heights: 1.7m for standing

height; 1.1m for seated individual's neck height; 0.6m for seated individual's waist; and 0.1m for ankle height. I did not include the results measured at 0.6m and 0.1m heights, as they are below the work surface and thus not affected by the air-flow generated by the fan. The fan was in a fixed position, and I performed measurements at three different power levels (Fig. 12, Fig. 13).

Table 1. Measurement results of Room 302

Position	Height (m)	Air velocities at different settings (m/s)		
		Erős	Közepes	Gyenge
1.	1.7	0.58	0.24	0.11
	1.1	0.31	0.17	0.08
2.	1.7	0.61	0.46	0.45
	1.1	0.5	0.4	0.39
3.	1.7	0.3	0.1	0.08
	1.1	0.17	0.11	0.03
4.	1.7	0.32	0.24	0.07
	1.1	0.31	0.19	0.04
5.	1.7	0.08	0.04	0.03
	1.1	0.09	0.06	0.03

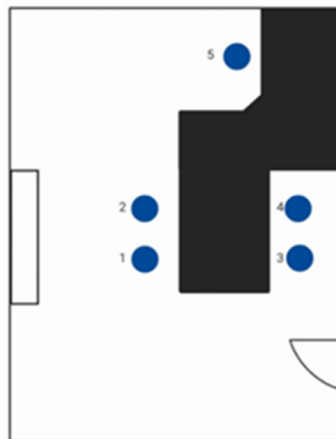


Fig. 9. Room 302 at the Faculty of Engineering.



Fig. 10. Midea split air conditioner

I recorded my measurement results in **Table 2**. I highlighted air velocities (v) exceeding the comfort criterion in red. It is evident that even at level 1, the air velocity at the distinguished point is many times higher than the allowed limit. Furthermore, I measured turbulence intensity (Tu), draft ratio (DR), and temperature (t).

4.3. Measurements with desk fan

The procedure and setup for the measurements were the same as those carried out with the tower fan. The measurement setup is shown in **Fig. 14** while the smoked condition is illustrated in **Fig. 15**.

The measurement results were similar to those obtained with the tower fan. The results that do

not meet the comfort criteria are highlighted in red in the table. (**Table 3**).

During the summer season, in rooms where there is no split air conditioner or fan coil, and the temperature exceeds 28°C , higher air velocity is appreciated by people and improves comfort. These offices, which only have fans, are used only briefly during the summer season. In the long term, rooms equipped with fan coils or split air conditioners are preferred. Each person can adjust the desk fans according to their own preferences, thus improving their personal comfort. The position and angle of the fan's head are adjustable, so I was not able to examine every option. Increasing the fan's speed depends on the internal air velocity.



Fig. 11. Placement of the fan and the person

Table 2. Measurement results of the tower fan

Fan speed	h (m)	Tu (%)	DR (%)	v (m/s)	t (°C)
1.	1.7	63	0	0.04	23.7
	1.1	7	84	1.26	22.3
2.	1.7	51	0	0.04	23.4
	1.1	7	100	1.57	21.9
3.	1.7	56	0	0.05	23.1
	1.1	7	100	1.78	26.1



Fig. 12. Tower fan measurement.



Fig. 14. Desk fan measurement.



Fig. 13. Smoke test of the tower fan.



Fig. 15. Smoke test of the desk fan.

4.4. Measurements with fan coil

I performed measurements using the SABIANA CARISMA fan coil. Its cooling capacity is 2.87 kW, and its heating capacity is 3.56 kW. [11] (Fig. 16)

During the measurements with the fan coil, I measured at 3 points. Point 1 was directly above the fan coil (most unfavorable location), point 2 was where one person was seated at the office desk, and point 3 (specific point) was where two people were seated at the desk, and I considered the position of the person closer to the fan coil during my measurements. (Fig. 17).

The most unfavorable location is near the fan coil, where high air velocities have been recorded. At the distinguished point, however, the air velocity has exceeded the comfort criteria compared to position two (Table 4).

5. Conclusions

I carried out comprehensive measurements during the summer period to demonstrate air velocities in areas where people typically spend most of their time in offices at specific heights. The results indicate the need to pay attention to the proper placement of workstations. I examined and con-

firmed the application possibilities of equipment in offices with different layouts through both field and laboratory measurements. After outlining the research methodology, I performed measurements in the offices. The offices of the Engineering Faculty provided me with fan coils, fans, and air conditioning units for my measurements. During the measurements, I used calibrated Testo instruments to measure indoor air velocity, turbulence intensity, draft ratio, and temperature. In the future, my goal is to explore the potential of natural ventilation during the summer season to understand the air velocities that develop in the occupancy zone.

Acknowledgments

Supported By The ÚNKP-23-1 New National Excellence Program of The Ministry For Culture And Innovation From The Source of The National Research, Development And Innovation Fund.

„The project with the reference number TKP2021-NKTA-34 was implemented with the support of the National Research, Development and Innovation Fund of the Ministry for Innovation and Technology within the framework of the TKP2021-NKTA grant program.”

Table 3. Measurement results of the desk fan

Fan speed	h (m)	Tu (%)	DR (%)	v (m/s)	t (°C)
1.	1.7	51	0	0.05	23.7
	1.1	12	100	1.36	22.7
2.	1.7	57	3	0.06	23.7
	1.1	19	100	1.47	22.7
3.	1.7	66	6	0.08	23.6
	1.1	27	100	1.72	22.8



Fig. 16. Fan coil.

Table 4. Measurement results of the fan coil

Position	h (m)	Tu (%)	DR (%)	v (m/s)	t (°C)
1.	1.7	31	100	0.76	20.8
	1.1	10	100	1.24	20.8
2.	1.7	46	7	0.08	21.3
	1.1	71	0	0.04	21.2
3.	1.7	44	25	0.21	22
	1.1	32	7	0.11	21.6

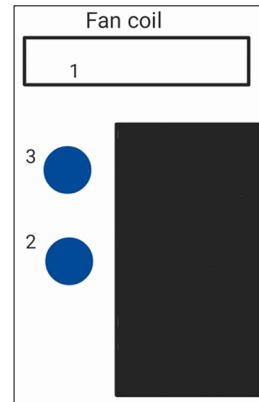


Fig. 17. Simulated office.

References

- [1] Csáki E.: *Influence of Transparent Surfaces on Summer Thermal Comfort in Buildings*. Proceedings of 16th Building Services, Mechanical and Building Industry Days, Debrecen, Hungary, 2010.)
- [2] Nedhal A., Sharifah F., Adel A.: *The Effect of Orientation and Glazed Area to the Indoor Air Temperature in Unventilated Building Sin Hot-Humid Climate*. The 3rd International Conference on Built Environment in Developing Countries, Universiti Sains Malaysia, 424–433.
- [3] Kalmár F., Csiha A.: *Interrelation between Glazed Surfaces, Building Structure and Thermal Comfort*. The 23rd Conference on Passive and Low Energy Architecture, Geneva, Switzerland, 6-8 September 2006.
- [4] Recknagel, Sprenger, Schramek: *Fűtés és klíma technika 2000*. Dialóg-Campus kiadó, Budapest–Pécs 2000.
- [5] Csáky I., Kalmár F.: *Indoor Temperature Monitoring in East Orientation Offices*. In: Proceedings of Denzero International Conference: Sustainable energy by optimal integration of renewable energy sources, Debrecen, 2014. 155–164.
- [6] MSZ CR 1752:2000; *Épületek szellőztetése. Épületek belső környezetének tervezési alapjai*; Magyar Szabványügyi Testület
- [7] https://www.testo.com/hu-HU/komforterzet-meres/turbulencia-fok/c/applications_building_construction_comfort_level_turbulence_degree (2023.08.23.)
- [8] <https://www.testo.com/hu-HU/testo-400/p/0560-0400> (2023.09.27.)
- [9] <https://www.testo.com/hu-HU/turbulencia-fok-szonda/p/0628-0152> (2023.09.27.)
- [10] <https://www.testo.com/hu-HU/testo-400/p/0560-0400> (2023.10.01.)
- [11] <https://climamarket.com/products/fan-coil-sabiana-carisma-crc-mv-33-kw-2-92-2-39> (2024.02.17.)



A WEAR DEVICE FOR PLASTIC GEARS

Szilveszter PORTIK,¹ Attila GERGELY²

¹ Sapiientia Hungarian University of Transylvania, Faculty of Mechanical Engineering, Târgu Mures, Romania, szilviportik@gmail.com

² Sapiientia Hungarian University of Transylvania, Faculty of Mechanical Engineering, Târgu Mures, Romania, agergely@ms.sapiientia.ro

Abstract

Our goal was to design and build a device that allows the investigation of wear for plastic spur gears. In the initial phase of the design process, cost-effectiveness was at the forefront. The device is part of a license project for the Faculty of Mechanical Engineering at Sapiientia Hungarian University of Transylvania and it will be used for research purposes in the Polymer Technologies Laboratory of the university. The designed test equipment allows the investigation of plastic spur gear wear properties at different loading and rotational speeds.

Keywords: *spur gears, wear, plastic, design.*

1. Introduction

The spur gear has a cylindrical cross-section, with teeth located on the surface. Spur gears are most commonly used to transfer the rotating motion from one shaft to another. There are several other choices regarding the transfer of rotating motion or torque from one shaft to another, however gears are exclusively used when slip between the two rotating parts is not permitted.

Spur gears are used in different industrial application, for example in agricultural machines, automotive transmissions, electrical home appliances, tools etc. The usability of spur gears is also widened by their increased load bearing nature. The high precision, high load bearing and high rotational speed can be seen as advantages of spur gears.

Steel is the material of choice for gears. In the case of metal as raw material, there are four types of base material to choose from, depending on the applied stresses and the use of the gear: non-alloy or low alloy steel, stainless steel, case hardenable steel and nitride steel. Each of these materials has its advantages, for example, hardened steel is more durable, nitrideable steel can be used to increase the insertion strength, but the highest strength is achieved with case hardened steel.

Depending on accuracy and productivity requirements, gears can be manufactured using the profiling process, a disc mill or finger mill, or the hobbing method. The hobbing method can be carried out by using a gear rack, gear hobs or gear shaper cutters. These processes, although widespread in industry and highly productive, require large and expensive equipment. Consequently, in an increasing number of applications, metal gears are being replaced by plastic gears.

Plastic gears have unique advantages over metal gears, including high efficiency, quiet operation, no external lubrication is needed and lower production costs. As a shortcoming, it should also be mentioned that the load bearing properties of plastic gears are inferior to that of metal gears. However, one of the most important consequences of their use is the significant weight reduction [1]. As a result, they are widely used in the automotive and aerospace industries, as well as in household and various appliances

Several technologies exist for the production of plastic gears. Machining processes are used for low volumes, but injection moulding is an economical way to produce high volumes. Over the last 10-15 years, however, 3D printing technology has become increasingly popular for the production of polymer substrate parts. 3D print-

when changing the distance between the axis. Furthermore, it has four short channels which are used to tension the belt between the motor and the drive shaft. A 3D model of the motherboard is shown in [Figure 3](#).

2.2.3. The moving plate

The driven axle is mounted on the movable table and a spindle is used to adjust the desired axle distance. All parts of the structure are made of metal and machined with a milling machine. The movement is generated by an M14×110 spindle which turns in a nut fixed on the table. This creates the linear displacement. The table consists of three parts. Parallel to the base, at a distance of 270 mm between the two uprights, are two 220 mm long, 45 mm wide and 21 mm high pair of dovetails, fixed by three bolts each. A 30° cut is made longitudinally, from the inside towards the bottom. The table rests on these two dovetails. Under the moving table there are also two shorter dovetails with the following dimensions: 130 mm long, 45 mm wide and 20 mm high. As a result of this method, the table can only move in the direction of the longitudinal axis. The bearing housings of the driven shaft are mounted on the two edges of the table. A 3D model of the moving table is shown in [Figure 4](#).

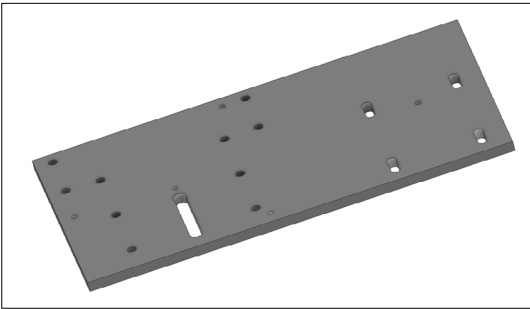


[Fig. 3.](#) The 3D model of the base plate.

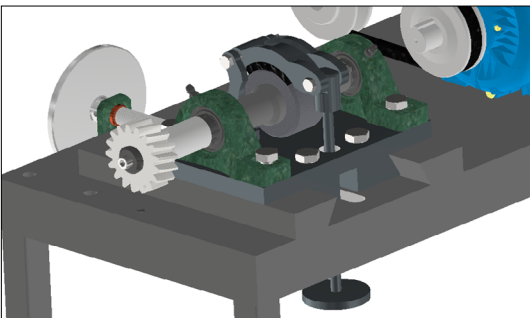


[Fig. 4.](#) The 3D model of the moving plate.

2.2.4. Angled support

The positioning of the driven axle is necessary to achieve the minimum axle distance. Positioning is provided by the two supports shown in [Figure 5](#). The elements are made of 40 mm thick plate. The workpieces are made from scrap metal, which reduces the production cost. In addition, the machining was carried out on a milling machine. The upper plane of the support is positioned at an angular offset of 23° to the base, thus preventing the axles and the chassis bearing housings from colliding when the minimum axle distance is set. There are also two M8×30 holes on the top to fix the bearing housing.

2.2.5. Shafts

The equipment has two axles. In order to minimize the shaft clearance, the bearings of the drive shaft are positioned between the bearings of the driven shaft. Both shafts are manufactured on a lathe from c45 material. The length of the shafts is 331 mm. The drive shaft is connected to the motor by a belt drive. The gears transmit the torque to the shafts by means of a latching connection, and an M6×20 bolt connection ensures constant positioning in the axial direction. Measured from the bearing housing, the gear is located at a distance of 10 mm. The distance between the two bearing housings is 201.5 mm. On the drive shaft, the gear is located 42.7 mm from the bearing. At the opposite end of this shaft is a centering hole. A 3D model of the propeller shaft is shown in [Figure 6](#).

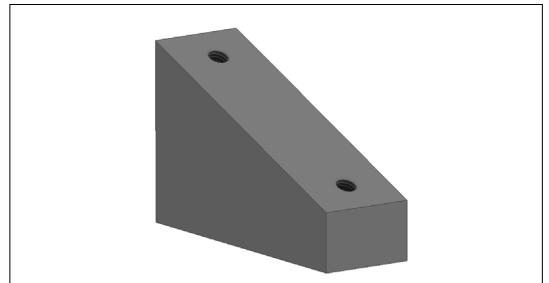


[Fig. 5.](#) The 3D model of the angled support.

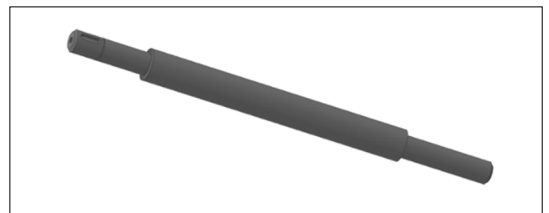


[Fig. 6.](#) The 3D model of the drive shaft.

A shorter length (249.75 mm) was specified for the drive shaft. The gears fixed to the two shafts must be in the same plane. The gears are also fixed by means of a latch and a locking screw. The bearing is located 69.75 mm from the end of the shaft. The space between the two bearings is 120 mm, in the middle of which a 30 mm wide brake disc will be located. The brake disc will also be secured by a latch. The other end of the axle can be used to retain the bearing. This end of the shaft also has a centering hole. A 3D model of the driven shaft is shown in [Figure 7](#).

2.2.6. Braking mechanism

The braking mechanism consists of five parts: a stand (1) which raises the brake disc (2) 57 mm on either side of the brake disc (2), and a brake insert (3) on which a brake pad (4) is fixed. In order to create a larger surface area, the brake shoe follows the curve of the disc at 100°. The braking torque is provided by means of load weights placed on the brake lever (5). This method has been chosen because it has proved to be the simplest way of providing a constant braking torque. The braking mechanism is shown in [Figure 8](#).

3. Conclusions

We have successfully designed a device that is capable of testing the wear properties of plastic gears. 3D modelling was used to identify design flaws. We were able to correct these errors during the design phase, thus avoiding the production of defective or inappropriate parts. The production was entirely carried out by myself in my own workshop. In the majority of cases I used a milling machine and lathe for machining. This was an excellent opportunity to gain insight into the execution of a complex task. Small adjustments were also made during the production process to achieve a better result.

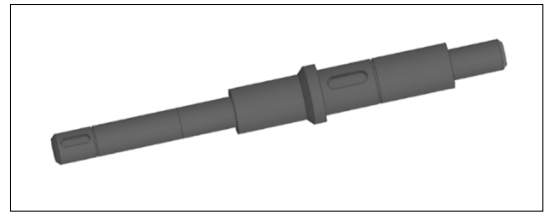


Fig. 7. The 3D model of the driven shaft.

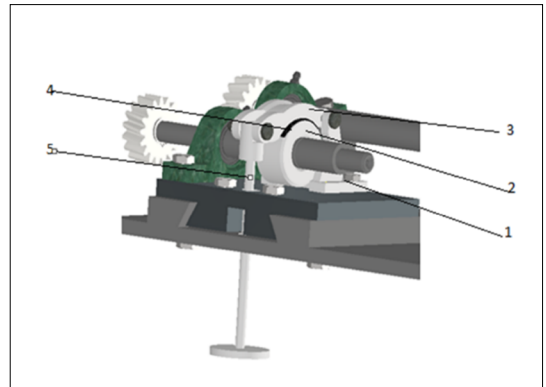


Fig. 8. The 3D model of the braking mechanism.

References

- [1] Mao K., Li W., Hooke C. J., Walton D.: *Friction and Wear Behaviour of Acetal and Nylon Gears*. *Wear*, 267/1. (2008) 639-645. <https://doi.org/10.1016/j.wear.2008.10.005>
- [2] Ye Z., Chris P., Ken M., Simon L.: *A Physical Investigation of Wear and Thermal Characteristics of 3D Printed Nylon Spur Gears*. *Tribology International*, 141. (2020) 105953. <https://doi.org/10.1016/j.triboint.2019.105953>.
- [3] Ye Z., Ken M., Simon L., Akeel S., Guotao M.: *A Parametric Study of 3D Printed Polymer Gears*. *The International Journal of Advanced Manufacturing Technology*, 107. (2020) 4481–4492. <https://link.springer.com/article/10.1007/s00170-020-05270-5>



AN EXAMINATION OF THE EFFECTIVENESS OF TUMBLING ON SAND-CAST PARTS

Balázs RAPPERT,¹ Erzsébet EGYED-FALUVÉGI²

¹ Sapiientia Hungarian University of Transylvania, Faculty of Technical and Human Sciences, student, Târgu-Mureș, Romania, gépészmérnöki szak, IV. év, Marosvásárhely, Románia, rappertbalazs@gmail.com

² Sapiientia Hungarian University of Transylvania, Faculty of Technical and Human Sciences, Department of Technical Engineering, Târgu-Mureș, Romania, faluvegi.erszebet@gmail.com

Abstract

The purpose of this study is to examine the effectiveness of the tumbling method on sand-cast metal parts. The first phase of the research was to design and construct a laboratory-scale tumbling mill, make samples for the measuring instruments available and to construct a coal-powered furnace that can be used in the making of the metal samples. After the design and construction of the necessary hardware, we conducted the experiment, took the necessary measurements and processed our data: this consisted of measuring the surface roughness of the metal samples before, during and after a complete tumbling cycle, then processing the resulting data. The experiment allows us to determine the optimal tumbling parameters such as the ideal tumbling medial size, the optimal speed of revolution of the tumbling drum and the smallest surface roughness achievable via the tumbling method. The experiment also allows us to find a correlation between the tumbling time and the change in surface roughness, which makes it possible to determine the optimal time frame in which the method is the most effective.

Keywords: *surface roughness, tumbling mill, sand-cast parts, tumbling, sand casting, tumbling media.*

1. Introduction

1.1. Surface Roughness

Tolerances are the permissible limits of certain properties on a part or an assembly, and they can refer to various aspects of the part: geometric tolerances like parallelism, roundness, perpendicularity or deviations in certain dimensions. Parts must also be manufactured to meet other criteria such as structural properties (hardness, elasticity, density and isotropy of the crystal matrix), optical (transparency, reflectivity) and others. One of these properties is surface roughness.

Surface roughness refers to the micro-irregularities of a surface usually created in the machining process. These can be feed marks or other irregularities in the measured area. [1] Surface roughness tolerances determine the acceptable roughness of a given surface of a part or a lower and upper limit, which the roughness cannot exceed.

One of the most widely used roughness index is the average surface roughness index, which,

according to the ISO 21920-2:2021 standard, corresponds to the numerical average of y-ordinates of the peaks and valleys along a continuous profile.

1.2. Measuring Surface Roughness

In order to determine whether the surface roughness of a part is within tolerance, it must be measured via various methods. These methods can be categorized as contact-based and contactless methods. [1]

Contact-based measuring instruments are the most common as they are widely available due to their relatively simple construction. They are reliable and easier to use than the more precise and more complex optical measuring instruments. Before the beginning of the 20th century, surface roughness was determined either through observation or by dragging one's fingernail on the surface. However, as the resolution of the average human eye is around 400 μm , more precise instruments were needed. [2]

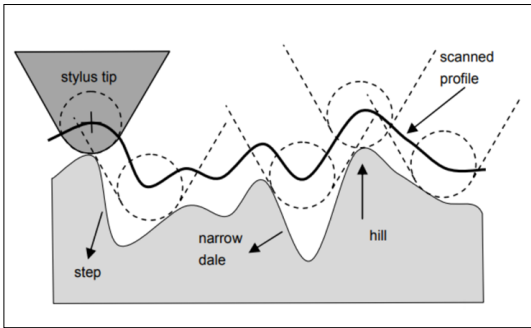


Fig. 1. The profile created by the stylus tip. [1]

The first contact-type stylus profilometer (from here on referred to as “SP”) was invented in 1929 by G. Schmaltz. The way portable SPs work is by dragging a diamond or ruby stylus along the surface of the part via the use of an electric motor. The accuracy of the resulting profile curve (in the case of analogue devices) or cloud of points (in the case of digital devices) ranges between 0.1 and 4 μm (Ra). The radius of the stylus tip is usually 5 μm and the length of the profile varies between 5 and 8 mm. [2] Thus it follows that the accuracy of the measurement depends greatly on the stylus tip radius, since the stylus cannot enter valleys narrower than the tip diameter (see Fig. 1).

1.3. Tumbling Mills and their Operation

The construction of a tumbling mill is simple, it consists of three main parts: a revolving drum, tumbling media and the drive mechanism.

The drum is usually a tube with a circular or polygonal cross-section, and depending on the size of the machine, can be closed, half-open or open on both ends. The tumbling or grinding media is placed in the drum, and it is usually a small granulate of some hard material (sand, ceramics, hard composites or metal). Larger metal or ceramic media is used for grinding powders. The grinding effect is a result of the continuous contact and friction between the media and the surfaces of the workpiece, small particles of the surface are abraded.

It has been proven that the shape of the media affects its behaviour and effectiveness in both grinding and tumbling. The research of Shi shows that cylpeb-shaped (conical cylinder with rounded points) media are more effective than spherical media with the same mass, since they have a larger surface. [3] Nanda P. et al used prism-shaped and pyramidal me-

dia in order to ensure contact between the media and the entire surface of the sample. [4, 5] Spherical and cylindrical media have a smaller chance of coming into contact with inner corners on the sample due to their rounded shape, while the tips of prism-shaped and pyramidal media have a better chance of coming into contact with these areas.

2. Methodology

2.1. The Measuring Instrument and the Samples

The goal of this study is to build a device that can be used to determine the effectiveness of tumbling and to examine how low of a surface roughness we can achieve with the method. The first phase consisted of designing and building a small tumbling mill and a fixture for the Insize ISR-C002 Surface Tester, along with metal samples. The fixture is necessary for holding the surface tester in place relative to the metal sample, thus ensuring that all measurements are taken on the same profile. Since the surface roughness of sand-cast metal parts is not only high but very uneven, this step was crucial in order for us to be able to examine the change in surface roughness between tumbling cycles, since even a deviation of a few millimetres would result in a drastic change in the roughness profile. Since the radius of the ruby stylus is very small and the technology at our disposal cannot provide such accuracy, each measurement was repeated multiple times and the final data was compiled from the numerical averages of these measurements.

The samples were sand-cast using fine mesh greensand. The blank for the samples was made using a Creality K1C 3D printer. Their dimensions can be seen in Fig. 2.

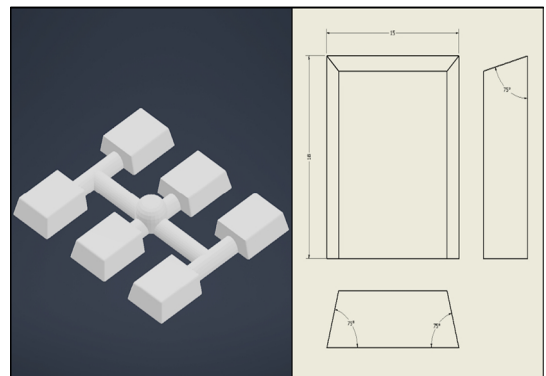


Fig. 2. CAD model and dimensions of the samples.

Using the CAD model of the sample, we generated a casting blank for six samples. We used cast samples from two metals, lead and aluminium.

2.2. Design and Construction of the Tumbling Mill

The second phase consisted of building the tumbling mill. During the design phase, we had to keep in mind multiple criteria: small size, low cost, reliability and simple assembly. The tumbling mill is shown in Fig. 3.

The drive chain is used to create the friction drive for the tumbling mill. The diameters of the drum and the rollers are known, therefore, in order to achieve the correct rotational speed for the drum, we had to calculate the appropriate pulley diameters.

In his book titled *Ball Milling Theory and Practice for the Amateur Pyrotechnician*, L.E. Sponenburgh explains why the optimal rotational speed is crucial. Under a certain rotational speed, the friction between the inside wall of the drum and the media is less than it is required for the rotating drum to move the media, thus the media simply slides along the bottom of the drum, and the relative motion between the media particles is zero. Beyond the so-called critical speed, the media travels so fast in the drum that centrifugal forces push it into the wall, thus the media once again behaves like a solid body with no relative movement between its particles. Critical speed is the highest rotational speed the drum can spin without this phenomenon occurring. [6]

Given that the inside diameter of the drum is $\varnothing D_{inner} = 110$ mm, and the size of the media varies between 3 and 5 mm, we can calculate the critical speed using the following formula:

$$N_{crit}[RPM] = \frac{423}{\sqrt{D_{Drum_{inner}} - \bar{d}_{media}}}$$

$$= \frac{423}{\sqrt{110 - 4}} = 41,08 \text{ RPM}$$

where the \bar{d}_{media} value indicates the average diameter of media particles (considering spherical media).

The optimal speed of rotation is 80% of the critical speed [6], which, in this case is 32.86 RPM. This rotational speed is achieved by using appropriate diameters for the pulleys for the transfer ratio.

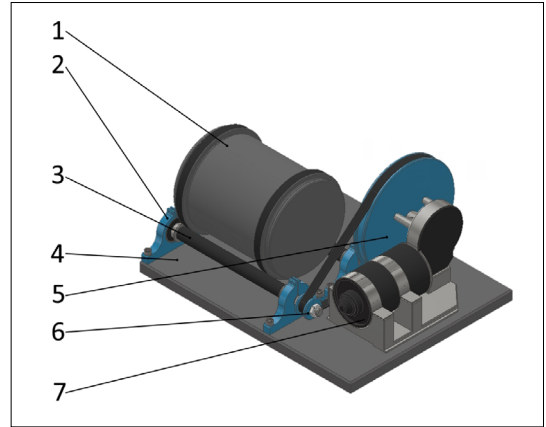


Fig. 3. CAD model of the tumbling mill (1 – Drum; 2 – Bearings; 3 – Driven Shaft; 4 – Baseplate; 5 – $\varnothing 90$ mm pulley; 6 – $\varnothing 16$ mm pulley; 7 – Motor)

2.3. Experiment Parameters

The goal of the experiment is to determine how tumbling time affects surface roughness. We started from the assumption that some change in surface roughness was guaranteed to occur, however, we aimed to examine the following in particular:

We used 3-5 mm grain bentonite-clay tumbling media for the experiment. In order to have a reference for our measurements, we measured the initial roughness of the raw-cast, unpolished surfaces (Rainital). We took three measurements from each sample and calculated the numerical average of the results. It is possible to increase the accuracy of the results by increasing the number of measurements per cycle, however, considering that both lead and aluminium are soft metals and the ruby stylus has a much higher hardness, we ran the risk of smoothing over the micro-deviations in the surface.

Tumbling time per sample was 4.5 (four and a half) hours. During the four and a half hours of tumbling, the samples were taken out of the drum regularly for measurements in order to track the changes in surface roughness. Thus, the total tumbling time was divided into smaller tumbling cycles. We determined the cycle time to be 30 minutes: this is long enough for detectable change to occur in surface roughness and provides a sufficient amount of data with a total of 10 cycles.

The samples were numbered from 1 to 6 in order to track their individual changes in surface roughness.

3. Results

We used Microsoft Excel for processing the data and all calculations (like numerical averages, for example) were done using the built-in functions of Excel.

The samples were given IDs based on their metal composition and number, such as Pb1, Pb2, ..., Pb6 for the lead samples and Alu1, Alu2, ..., Alu6 for the aluminium ones. The samples will be referred to by their IDs from here on. Both the surface tester and the sample were tightened down in the fixture in order to ensure that the measurements were taken on the same profile, however, due to the difference in accuracy between the fixture and the stylus, some measurements were still thrown off-profile.

The initial average surface roughness was $Ra(Pb_avg1) = 8.785 \mu m$ on the lead samples and $Ra(Alu_avg1) = 4.816 \mu m$ on the aluminium ones. These values show the total numerical average of the surface roughness values from the samples,

since the values for individual samples vary (such as: $Ra(Pb2) = 12.003 \mu m$, $Ra(Pb6) = 6.37 \mu m$; $Ra(Alu4) = 6.482 \mu m$ and $Ra(Alu2) = 3.49 \mu m$).

We used line plots to illustrate the results and compiled graphs for both the surface roughness change on the individual samples and the combined averages. The surface roughness changes for individual samples are shown on Fig. 4 and Fig. 5.

We can observe that for both lead and aluminium samples we have a spike at the 90-minute mark. We suppose that this is either a measurement or fixture error, since had the surfaces of the samples been damaged, this would have shown up in successive measurements as well.

Since the goal of our research was not to examine individual samples but the effectiveness of the tumbling method as a whole, the more relevant graphs are the ones showing the change in the average values of surface roughness. This is shown in Fig. 6 and Fig. 7.

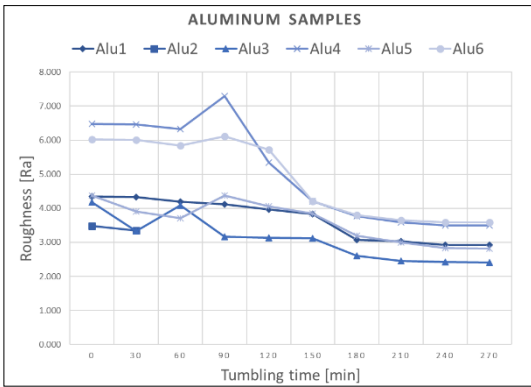


Fig. 4. Surface Roughness Change in Lead Samples.

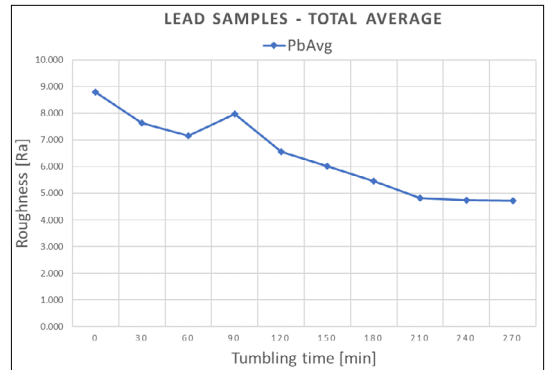


Fig. 6. Surface Roughness Change in Lead.

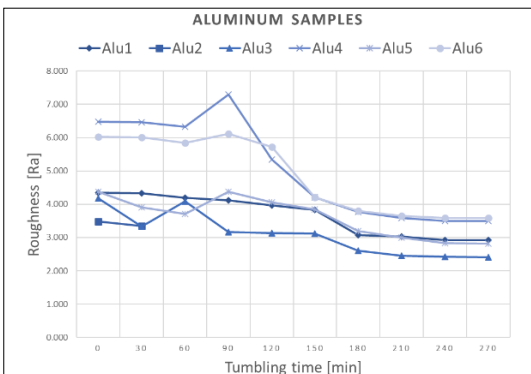


Fig. 5. Surface Roughness Change in Aluminium Samples.

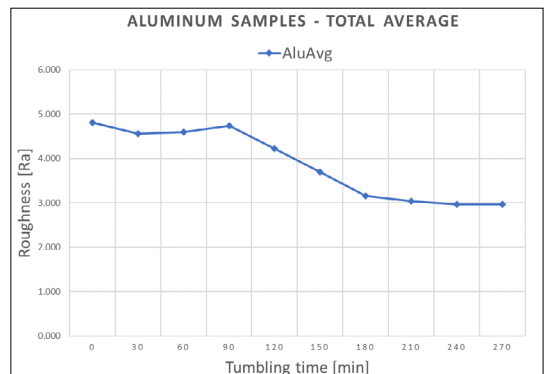


Fig. 7. Surface Roughness Change in Aluminium Samples.

The final surface roughness on the lead samples was $Ra(Pb_final) = 4.725 \mu\text{m}$ while on the aluminium samples it was $Ra(Alu_final) = 2.962 \mu\text{m}$. The difference between the initial and final values of surface roughness gives us the total change in surface roughness, ΔRa , which is $4.059 \mu\text{m}$ for the lead samples and $1.853 \mu\text{m}$ for the aluminium sample.

4. Conclusions

When observing the graphs, we notice that the not only are the slopes of the curves similar (despite the difference in material and initial surface roughness) but both slopes show a decrease in steepness and start to flatten out towards the final values.

This led us to believe that the tumbling method is only effective in changing the surface roughness to a certain point, after which it becomes impossible to achieve significant change. This can be explained by the peaks of the roughness profile being sharper in the initial stage, thus require less force to remove than in later phases once the sharp peaks have been abraded to smoother ones. After a certain point, the tumbling media can no longer create enough force on the peaks to remove significant amounts of material, thus the rate of decrease in surface roughness slows down or even stagnates.

The parameters of this phenomenon are dependent on various factors such as the difference in hardness between the samples and the media and

the media's grain size (larger grains cannot enter the deeper and narrower valleys of the profile).

We have also noticed an inverse correlation between the change in amount of surface roughness and the hardness of the material (given the same tumbling media): the softer lead samples exhibit a much greater change in surface roughness ($\Delta Ra(Pb) = 4.059 \mu\text{m}$) than the harder aluminium ones ($\Delta Ra(Alu) = 1.853 \mu\text{m}$).

References

- [1] Erik O., Franklin D., Holbrook L, Henry H. R.: *Machinery Handbook*. 27. kiad., Industrial Press Inc, New York, 2004.
- [2] Demircioglu P.: *Topological Evaluation of Surfaces in Relation to Surface Finish*. Adnan Menderes University, Aydın, Turkey, 2017.
- [3] Shi F.: *Comparison of Grinding Media—Cylpebs Versus Balls*, Minerals Engineering, 17. 2004.
- [4] Alban J. L., Chester A. R.: *The History of Grinding*. Society of Mining, Metallurgy and Exploration, Colorado, 2009.
- [5] Nanda P., Hassim, M. H., Idris M. H., Muhammad, H. J., Arafat, A.: *Effect of Mechanical Tumbling Parameters on Surface Roughness and Edge Radius of Medical Grade Cobalt Chromium Alloy*. International Journal on Advanced Science Engineering Information Technology, 9/1. 2019.
- [6] Sponenburgh L. E.: *Ball Milling Theory and Practice For the Amateur Pyrotechnician*. Bridge City Enterprises, 1995;
- [7] ISO 21920-2:2021 Geometrical Product Specifications (GPS) — Surface Texture: Profile — Part 2: Terms, Definitions and Surface Texture Parameters, 2021;



DESIGN OF ELEVATOR DOOR FOILING MACHINE

Rezes Gábor,¹ Szigeti Ferenc,² Dezső Gergely³

¹ University of Nyíregyháza, Institute of Technical and Agricultural Sciences, Nyíregyháza, Hungary, rgaborezes@gmail.com

² University of Nyíregyháza, Institute of Technical and Agricultural Sciences, Nyíregyháza, Hungary, szigeti.ferenc@nye.hu

³ University of Nyíregyháza, Institute of Technical and Agricultural Sciences, Nyíregyháza, Hungary, dezszo.gergely@nye.hu

Abstract

The topic of this article is the design of a foiling machine for covering elevator doors and their components with protective film. The thesis presents the design process, from the initial parameters and material selection through structural design to strength dimensioning and verification, and the selection of the necessary drive motor and worm gear based on the results of the calculations is further explained. The compliance of the elements of the equipment with the strength requirements is verified by finite element testing, taking into account door panels of different sizes and numbers. A detailed flow analysis of the air smoothing of the foiling operation is presented with the help of the Ansys application.

Keywords: *elevator, foiling machine, machine design, finite element method, automation.*

1. The construction of the foiling machine

As a starting point, the dimensions are based on the highest and widest door manufactured at the company. The height of this door is 3020 mm, and its width is 930 mm. Therefore, the dimensions of the laminating machine to be manufactured were slightly increased (Fig. 1) [1] ensuring that wrapping with protective film can be carried out for all sizes without any issues.

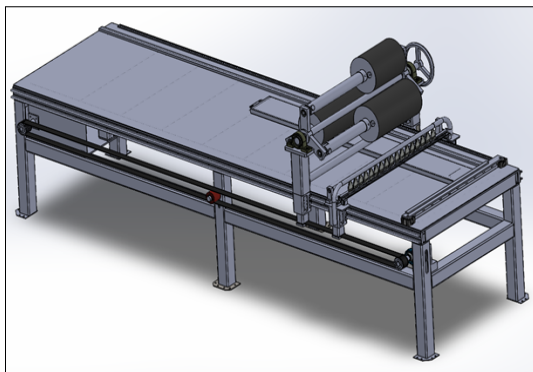


Fig. 1. Foiling machine

1.1. Design and loading conditions of the table

A finite element analysis was first performed on the table in its upright position without any load, and later with the load of multiple elevator doors and other loads [1].

In this part of the examination, the assembly to be presented later was not included, for simpler calculations. Throughout the analysis, the load resulting from the weight of the assembly was accounted for as a distributed load (Fig. 2) [1].

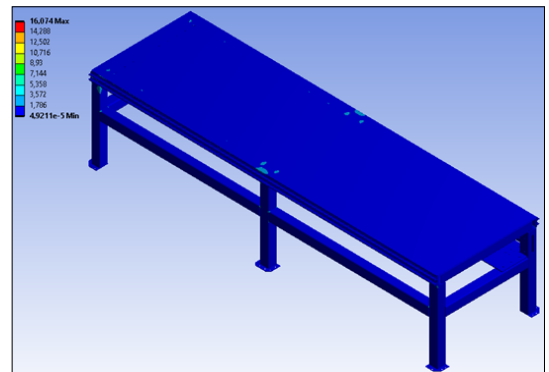


Fig. 2. The of the table in idle state.

It can be observed that the structure is not stressed by the empty condition even when the assembly is positioned between the supports of the frame, resulting in a maximum stress of 15.4 N/mm². As depicted in Fig. 3 [2], the deflection of the structure barely reaches the value of 0.06 mm.

During the examination of the results (Table 1) it may be striking that an average elevator door (Fig. 4) [2] is capable of generating almost the same maximum compressive stress as the largest panel (Fig. 5) [2].

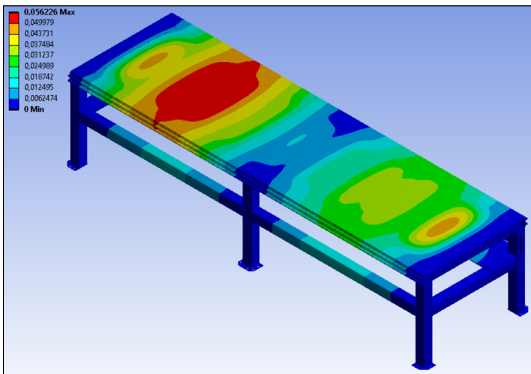


Fig. 3. The deflection of the table in idle state.

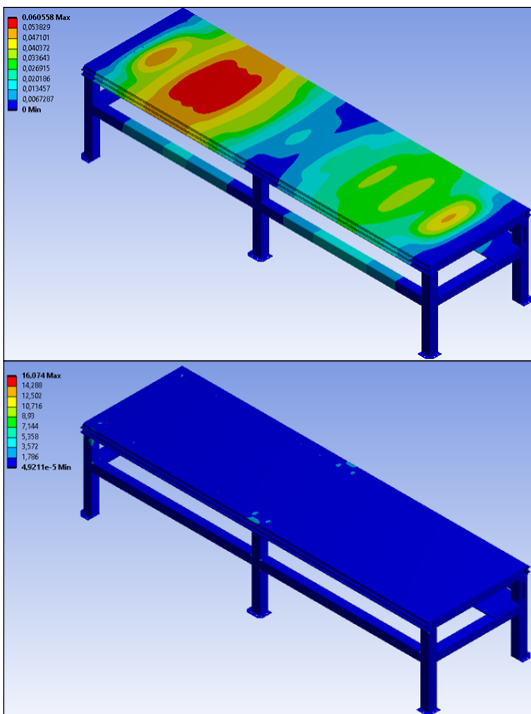


Fig. 4. Average compressive stress and deflection under the load of a typical lift door.

This is possible because the larger panel lies over a greater surface area, allowing its weight to distribute over a larger area and encounter more stiffening ribs, thus reducing the load on individual elements.

Under the additional load scenario, a situation was considered where four individuals weighing 80 kilograms each are seated on the structure (Fig. 6) [2]. As can be deduced from the data, even this scenario does not critically stress the structure.

Table 1. Stresses and deflections on the table under various loads

	Average lift door	In case of the largest lift door
Stress	16.0 N/mm ²	16.1 N/mm ²
Deflection	0.06 mm	0.058 mm
	Stress in idle state	In case of other load
Stress	15.4 N/mm ²	20.8 N/mm ²
Deflection	0.05 mm	0.14 mm

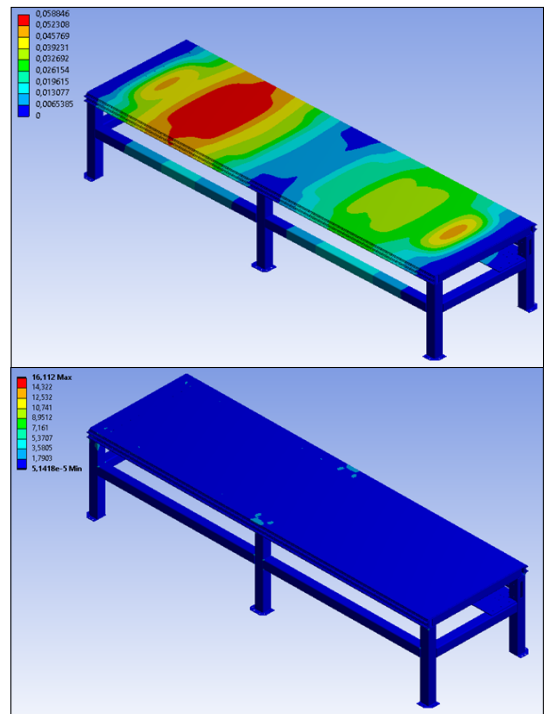


Fig. 5. Compressive stress and deflection under the maximum load of a lift door.

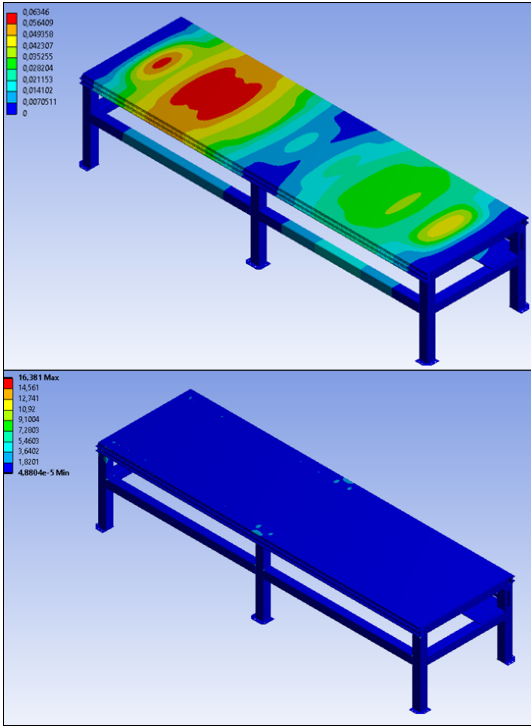


Fig. 6. Compressive stress and deflection under other loads.

1.2. Designing the assembly and its loads

The assembly consists of two units. There is one unit responsible for holding, guiding, and aligning the film, and another unit responsible for smoothing, forwarding, and cutting. First, I will present the part responsible for holding the film. (Fig. 7) [1].

The loads acting on the assembly include the force resulting from its own weight, the shafts of the coil holder and its bearings, as well as the weight of the film coil, the force associated with pulling it down, and the weight of other machine elements and components. We did not conduct a separate analysis for the second unit because the forces acting on the linear carriage in this case are significantly smaller than those in the first unit.

To pull down the film, a force of 15 N is required, which was determined using a spring force gauge, testing several pulling angles. The maximum force recorded was 20 N; therefore, this value was considered for the loads.

The maximum stress acting on the assembly was 2.7 N/mm² (Fig. 8).

During the examination of the assembly, we did not account for other loads. The maximum deflec-

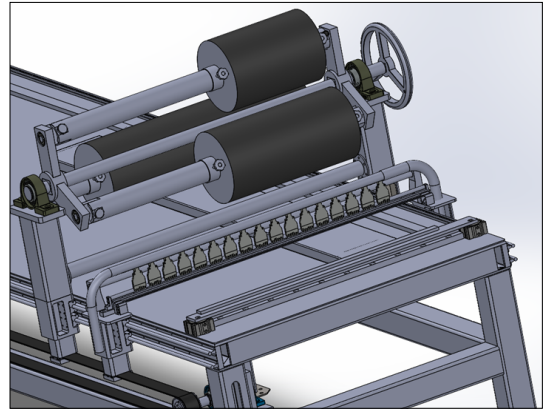


Fig. 7. Assembly.

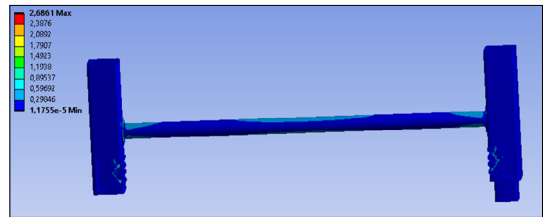


Fig. 8. Diagram of the deflection of the assembly.

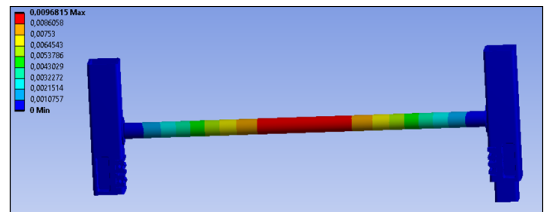


Fig. 9. Diagram of the compressive stress of the assembly.

tion is visible at the center, which is significant due to the length of the assembly, but the magnitude of deflection does not even reach 0.01 mm (Fig. 9).

1.3. Operation of the assembly

The worker selects and places the appropriate width of film based on the width of the element to be wrapped, then places the element to be wrapped on the table. Next, the machine is positioned at its starting position for threading the film. After threading the film through the smoothing roller, the worker threads it through the pair of rollers and then between the pneumatic jaws. Then, the operator starts the machine, which seals the film, initiating the wrapping process. The unit responsible for smoothing moves along with the assembly and, using high-pressure air,

smoothens the film. After wrapping is completed, the assemblies stop, and a hot wire is used for cutting. Once the cutting is done, the gripping jaws release to allow the worker to comfortably remove the element and insert the next one. After completing the operations, the assemblies return to their starting positions, and threading occurs.

We solved the replacement of the rolls with a rotatable shaft (Fig. 10). One end of this shaft is equipped with a hinge, which can be easily unfolded to facilitate roll replacement. The other end of the shaft is provided with an easily detachable locking pin.

Clamping rings ensure the proper positioning of the films, determining the position of the film from both side (Fig. 11). Both rings are adjustable, so if a larger series is needed, the operational time can be reduced by positioning the same preset film on multiple arms simultaneously.

1.4. Assembly inserts

The purpose of the assembly inserts is to facilitate the connection of the linear carriages with the assembly. If the assembly consisted only of closed sections, the carriage would only be able to rest on the

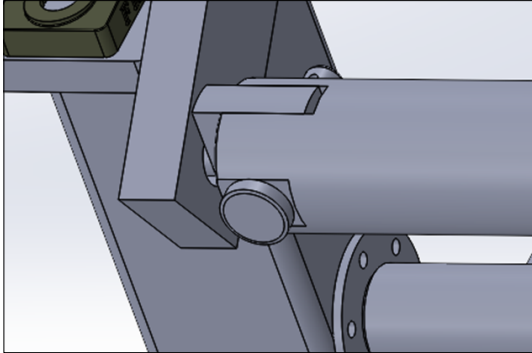


Fig. 10. Hinged axis.

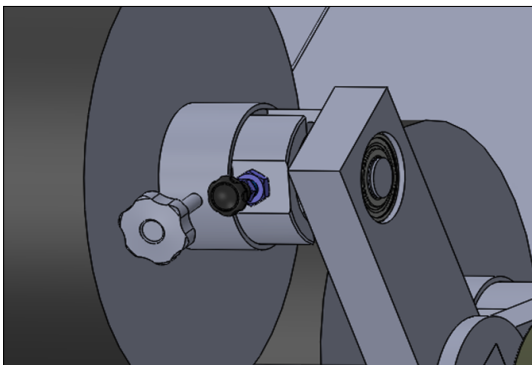


Fig. 11. Retaining ring and retaining pin.

thickness of the closed section walls, which would not allow for safe and stable movement of the carriage.

Part 01 of the assembly insert (Fig. 12) will contain the surfaces necessary for connection with the toothed belt. This part will connect to the toothed belt, transmitting the required movement for the wrapping process. Part 02 of the assembly insert (Fig. 13) assists in guiding on the opposite side.

2. Sizing of linear guide and linear carriage

The linear guide is loaded by the weight of the assembly in idle mode, but during the wrapping process, the pulling of the film also exerts some force on the guide (Fig. 14) [1].

Maximum load on the linear carriage:

$$C_{max} = C_{lcs} \cdot z = 774 \text{ N} \cdot 8 = 6192 \text{ N}$$

$$F_{ly} = F_1 \cdot \sin \alpha = 20 \text{ N} \cdot \sin 20^\circ = 6,84 \text{ N}$$

$$\begin{aligned} C &= (m_{szerelevény} + m_{fólia} + m_{egyéb}) \cdot g \cdot F_{ly} = \\ &= (52,5 \text{ kg} + 13,5 \text{ kg} + 12,5 \text{ kg}) \cdot 9,81 \text{ m/s}^2 + \\ &\quad + 6,84 \text{ N} = 776,925 \text{ N} \end{aligned}$$

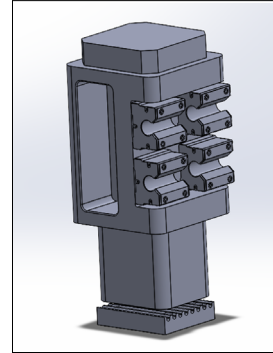


Fig. 12. Assembly inserts 01.

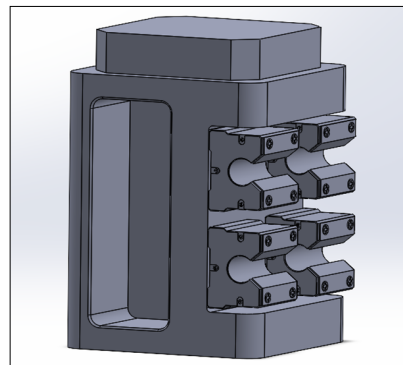


Fig. 13. Assembly inserts 02.

where:

- C_{lcs} : load capacity of the linear carriage
- C_{max} : maximum load capacity of the linear carriage
- C : load
- z : number of linear carriages
- F_1 : force required to pull the film
- α : angle of film pulling
- $m_{szerelevény}$: mass of the assembly
- $m_{fólia}$: mass of the film roll
- $m_{egyéb}$: mass of machine elements and the smoothing roller
- g : gravitational acceleration
- $C < C_{max} = 3096 \text{ N}$

So, the selected linear carriage is suitable

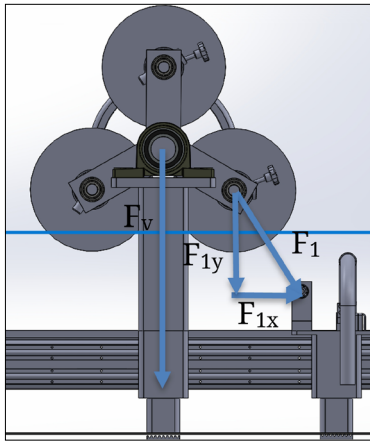


Fig. 14. Load on the linear guide.

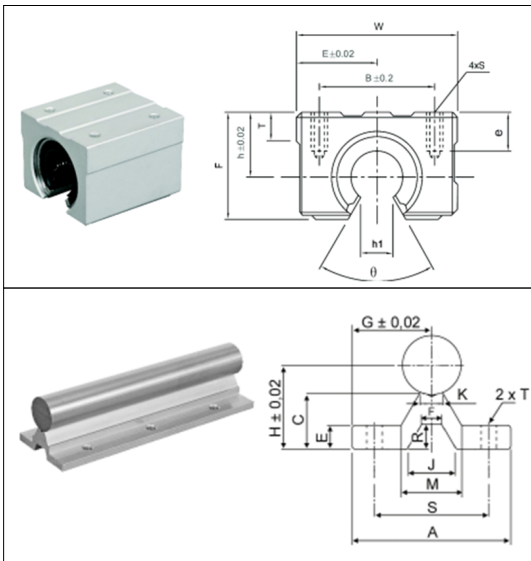


Fig. 15. Linear guide and linear carriage. [3, 4]

3. Smoothing of the foil

Compressed air was used to smooth the film, thereby achieving the ability to wrap elements with more complex contours following future developments. The blow-off device operates at a pressure of 4 bar and uses 17 multi-channel flat jet nozzles [5] These nozzles are energy-efficient and have a lower noise level compared to similar high-performance counterparts (Fig. 16).

In the rest of this section, I will present the fluid flow simulation of this unit. It was found necessary to perform fluid flow simulation because the assembly itself is quite long, and we wanted to ensure that the pressure remained consistent throughout the entire conduit, or at least within a certain tolerance. This is crucial because most of the wrapping occurs on the opposite side of the power supply, and only the front of the largest panels receives the highest pressure.

As seen in Fig. 17, the maximum pressures occurring on the surface are nearly identical beneath the openings of the nozzles. Moving away from these points, we can observe that the pressure decreases rapidly to about half. This does not pose a problem during wrapping, as this air jet will travel across the entire surface, performing both a pre-smoothing and a post-smoothing action. The spacing between the nozzles (dead zone) is relatively small, so this does not cause issues in smoothing the film.

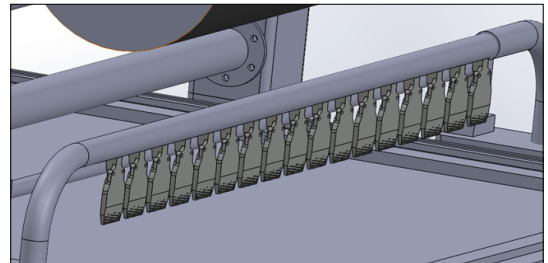


Fig. 16. Foil smoothing unit.

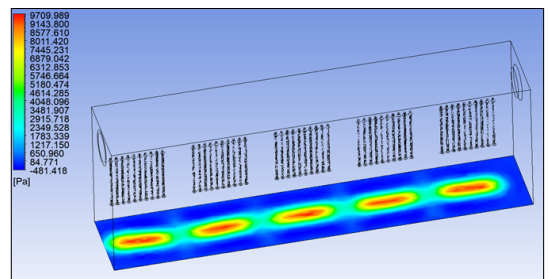


Fig. 17. Pressure distribution on the area to be wrapped.

In Fig. 18 the complete pressure distribution in the pipe and the nozzles is depicted. While the pressure in the pipe is 4 bar, when the air exits the nozzles, it exerts only approximately 1 bar of pressure. However, the velocity of the exiting air is several times greater than that of the compressed air flowing in the pipe.

In Fig. 19, the trajectory of airflow is illustrated. In this figure, we see 200 flow paths, and the surface pressure generated by the airflow is also indicated, with values that can be read from Fig. 17.

Based on the simulation, it can be concluded that the designed multi-channel nozzle will be suitable for the task at hand.

4. Cutting of the foil

The film cutting is ensured by a hot wire, which is heated by passing an appropriate amount of current through it. At one end of the wire, there is a hinge connected to a spring, which keeps the wire constantly tensioned (Fig. 20).

At the other end of the wire, a CAF6/10 type mini pneumatic piston is connected, which is used to carry out the cutting process (Fig. 21).

5. Selection of motor and drive

To select the motor, we first need to know the load force. In this case, the load force is determined by the frictional force resulting from the weight of the

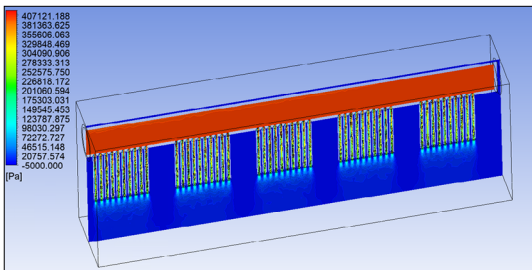


Fig. 18. Full pressure map across the cross-section of the subassembly.

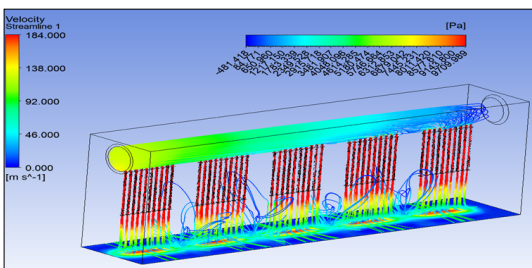


Fig. 19. Presentation of speed and pressure distribution.

assembly and the force required to pull the film. Then, based on the combined force determined above, we determine the torque and select a motor accordingly. The motor type is a three-phase asynchronous motor, along with a gear drive.

Drive type: Belt drive (Fig. 22)

5.1. Determining the forces and torque acting on the motor

We will present the load on the motor in Fig. 23, then determine the torque load.

$$M_{motor} = (P \cdot 60) / (2 \cdot n_1 \cdot \pi) = (250W \cdot 60) / (2 \cdot 31.66 \text{ 1/min} \cdot \pi) = 75.4 \text{ Nm}$$

$$F_g = (m_{szerelevény} + m_{fólia1} + m_{fólia2} + m_{fólia3} + m_{egyéb}) \cdot g = (52.5 \text{ kg} + 5 \text{ kg} + 8.5 \text{ kg} + 12.5 \text{ kg}) \cdot 9.81 \text{ m/s}^2 = 770.085N$$

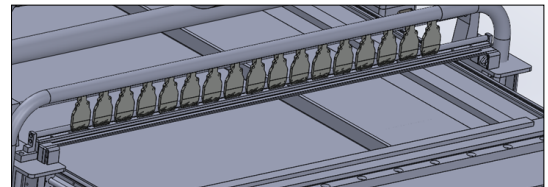


Fig. 20. Foil cutting unit.

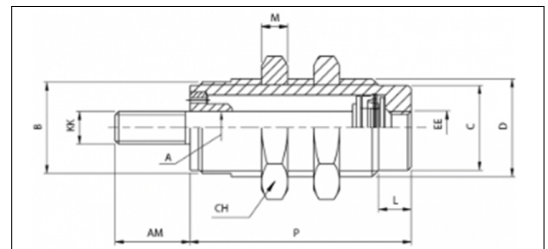


Fig. 21. Pneumatic cylinders of the foil cutting unit. [6]

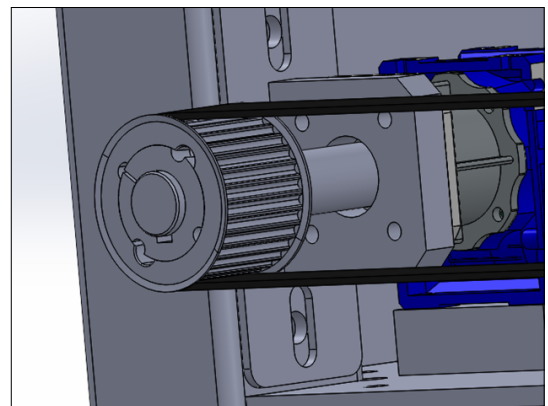


Fig. 22. Belt drive.

$$F_{1x} = F_1 \cdot \cos \alpha = 20 \text{ N} \cdot \cos 20 = 18.79 \text{ N}$$

$$F_s = F_g \cdot \mu = 770.085 \text{ N} \cdot 0.2 = 154.017 \text{ N}$$

$$F_t = F_s + F_{1x} = 154.017 \text{ N} + 18.79 \text{ N} = 172.807 \text{ N}$$

$$M_{\text{terhelő}} = d/2 \cdot F_t = (0.08 \text{ m})/2 \cdot 172.807 \text{ N} = 6.91 \text{ Nm}$$

$$M_{\text{terhelő}} \leq M_{\text{motor}}$$

where:

- F_g : force resulting from the weight of the pulled elements
- F_s : frictional force
- μ : coefficient of sliding friction
- F_t : load force

The motor is also loaded by the unit responsible for smoothing and cutting the film, but its load is much smaller than that of the film holding unit. Therefore, a three-phase asynchronous motor (Fig. 24) and a worm gear drive (Fig. 25) for the drive were chosen.

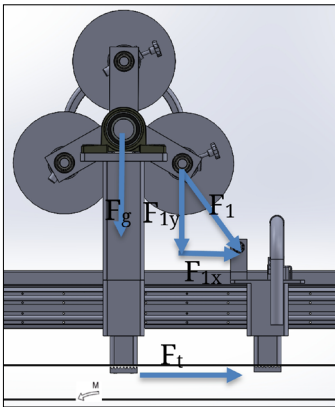


Fig. 23. The loads on the motor.



Fig. 24. Three-phase asynchronous motor. [8]



Fig. 25. Type VI worm gear unit. [9]

$$n_1 = n_2/i = (850 \text{ 1/min})/30 = 31.66 \text{ 1/min}$$

$$v_k = (d_1 \cdot n_1 \cdot \pi)/60 = (0,08 \text{ m} \cdot 31.66 \text{ 1/min} \cdot \pi)/60 = 0.133 \text{ m/s}$$

where:

- n_1 : speed of the pulley [7]
- n_2 : motor speed
- i : gear ratio of the worm gear drive
- v_k : peripheral speed
- d_1 : diameter of the pulley

Determining the wrapping speed:

$$v_{\text{föltöltés}} = d_1 \cdot \pi \cdot n_1 = 0.08 \text{ m} \cdot \pi \cdot 31.66 \text{ 1/min} = 7.957 \text{ m/min}$$

The required wrapping speed is 3 average elements per minute, which is 20 seconds per element. The height of an average panel is 2200 mm.

$$s_{\text{teljes}} = s_{\text{panel}} \cdot 3 = 2200 \text{ mm} \cdot 3 = 6600 \text{ mm}$$

The required distance to be covered in one minute is 6600 mm. The provided distance is 7957 mm. Therefore, the motor ensures the required wrapping speed.

6. Conclusions

A structural analysis revealed that the construction is considerably oversized; however, due to the stiffness of the structure, this overdesign is justified from a static perspective. After sizing and selecting various machine components, such as the linear guide or the carriages running on it, it became apparent that these components can be operated with very low utilization rates, as the loads acting on them are also low.

Further design tasks include selecting the appropriate components for the subassemblies and ensuring their energy supply. Additionally, increasing workplace safety requires greater attention, necessitating the implementation of light curtains for contact protection, obstruction protection, and occasional overload protection.

As a development direction, we have identified full automation, meaning that only the film roll would need to be replaced, and threading would only be required once at the start of the roll. Furthermore, the development of a new type of automatic cutting system is necessary to minimize the worker's tasks to material handling only. The need for film cutting arises because not all lift doors are of the same width, but the width of the film is fixed. Therefore, to avoid waste, another cutting system and track need to be designed and programmed. This development could potentially

increase productivity, as if the width of the film is at least twice the width of the elements to be wrapped, the machine could wrap two elements in one cycle. To support this, we aim to introduce a user-friendly, touch-screen programmed PLC. With this PLC, we aim to enable the worker to achieve the best material yield with minimal downtime by entering few parameters.

Another development goal is to enable the wrapping of columns in addition to lift doors and their decorative elements. To achieve this, separate moving segments need to be designed due to the different heights of the elements.

Acknowledgments

Research work was supported by the Scientific Council of the University of Nyíregyháza.

References

- [1] Solidworks
- [2] Ansys
- [3] https://www.powerbelt.hu/uploads/source/catalogs/4460_sme_kbe.pdf
- [4] [https://www.powerbelt.hu/uploads/source/catalogs/4457_sa_ftsn_gw_%C3%BAj%20\(1\).pdf](https://www.powerbelt.hu/uploads/source/catalogs/4457_sa_ftsn_gw_%C3%BAj%20(1).pdf)
- [5] https://www.hennlich.hu/fileadmin/user_upload/KATEGORIEN/Luftduesen/Mehrkanaelduesen/Dokumente/hu_Druckluftdusen_600.130.56.pdf
- [6] https://www.hafnerpneumatika.com/caf/caf_6-10
- [7] https://www.powerbelt.hu/uploads/source/couplings_pulleys_joints/sit/Timing-pulleys-taper-bush-HTD.pdf
- [8] https://www.powerbelt.hu/uploads/source/catalogs/ta_motor_type_catalogue.pdf
- [9] https://www.powerbelt.hu/uploads/source/catalogs/vi_gearbox_catalogue.pdf



EXAMINATION OF EMBEDDED SYSTEM ADAPTIVE CONFIGURABILITY

József VÁSÁRHELYI,¹ Roland BATÓK,² Dániel DRÓTOS³

¹ University of Miskolc, Faculty of Mechanical Engineering and Information Technology, Institute of Automation and Infocommunication. Miskolc, Hungary. jozsef.vasarhelyi@uni-miskolc.hu

² University of Miskolc, Faculty of Mechanical Engineering and Information Technology, Institute of Automation and Infocommunication. Miskolc, Hungary. roland.bartok@uni-miskolc.hu,

³ University of Miskolc, Faculty of Mechanical Engineering and Information Technology, Institute of Automation and Infocommunication. Miskolc, Hungary. daniel.drotos@uni-miskolc.hu

Abstract

Field Programmable Gate Arrays or FPGA circuits have been the focus of applied research since their appearance. Following the introduction of these circuits in 1980, their year-by-year development and the expansion of application areas have opened up new areas of research. With the appearance of system-on-chip, SOC (System on Chip) solutions and adaptive processing units, they occupy an important role in industrial applications. The question is: when, why and what hardware is to change dynamically during system operation? Whether it is necessary to expand computing resources by expanding new circuit blocks or by inserting soft-core processor(s), this can be determined by examining the computing load of the embedded system during operation. This article presents the tests that were performed on the processors of the embedded systems, in order to determine the computational load of the processor and how the interrupt handling can be accelerated. The article also presents the examination of fuzzy interpolation.

Keywords: *embedded systems, dynamic function exchange, FPGA, robot control, fuzzy interpolation.*

1. Introduction

Field Programmable Gate Arrays or FPGA circuits have been in the focus of applied research since their appearance. The areas of application, which at that time were still limited to the implementation of two-level logical networks, are now suitable in the areas of telecommunications, real-time embedded systems, artificial intelligence, image processing and adaptive hardware using dynamic function exchange.

One of the important parameters of embedded systems is the dissipated power and computation speed rate. It is possible to reduce or increase these design parameters by several methods. For example, reducing the frequency of the microcontroller will reduce the dissipated power, but this also reduces the computation speed. The best solution is when the processor load is analysed while executing the application task and then by making the necessary modifications based on the results. One possible solution is a new approach

to the interruption mechanism or the examination and hardware implementation of the control algorithm. Both solutions raise the following questions: Is it necessary to expand computation resources by adding new hardware blocks or by inserting new soft-core processor(s)?

This article is the extended version of the FMTÚ 2024 conference plenary presentation. It presents an examination of the computational load of the processor used in embedded systems, and then by presenting two examples – interrupt management and fuzzy interpolation with state machine implementation. These two examples illustrate the possible application of adaptive operation and increasing the computation speed.

2. Literature review

2.1. Processor load analyses

The computer model formulated by John von Neumann in 1945, in his report "The First Draft of the Report on the Edvac" [1], has been reviewed

by many articles over the years, presenting all its advantages and disadvantages.

The biggest problem was caused by the fact that the processor manufacturers left out the extra status bit used in the data storage by Neumann, which would have had the task of indicating the status of the stored data (program code or data) of the stored data.

The Neumann principles are as follows [2]:

- fully electronic computer,
- use of binary number system,
- existence of arithmetic unit (universal Turing machine),
- existence of central control unit,
- existence of internal program and data storage i.e. memory [2].

The operation of the Neumann model is most effective when a processor performs a single task [3]. This approach is generally true for embedded systems. In an embedded system, the processor has a well-defined task, especially when not using an operating system for controlling its operation. Problems with the model occur when the number of tasks differs from the number of processors present in the machine, i.e. the number of tasks is higher than the number of processors. Unfortunately, software developers still adhere to the classic Neumann model, so the operating system hides the hardware layer from the user, so it appears as if the processor is available for all the tasks [4].

Since the use of FPGA technology, we are concerned with two types of processor: soft-core and hard-core. The former is described in a hardware description language (VHDL or Verilog) and inserted into the FPGA design, while the latter is integrated on the same die with the programmable logic.

For embedded systems, which are implemented using low-resource FPGAs, it is especially important to examine the processor or microcontroller load during the execution of the user software.

In FPGAs, one can insert a soft-core processor using different methods. Either using Intellectual property modules (IP), which is one of the most common methods, or using the register transfer level (RTL) method. The use of the RTL soft-core processor has the advantage that all the internal signals of the central unit (CPU) are accessible, and the processor load test can be carried out. In contrast, in the case of IP-based design, the internal signals of the processor are not available, so the processor load test can not examine the internal signals.

In the case of FPGA-based systems, it is possible to increase the computing power of the processor by using other auxiliary accelerators and co-processors. Inserting these kinds of circuits during operation is possible with the dynamic function exchange. In this way the processor computation load can be reduced.

Analysing the computation load during operation of the processor is based on the examination of the system signals. Hardware errors can be determined by monitoring all signals [5]. The method tests the hardware operations and draws conclusions regarding machine malfunctions.

Another test method was used in the design phase, to determine the necessary hardware resources required for the optimal operation of the software in an embedded system. [6] [7]

Zhao et al. used a software tool to determine the errors in the running program. A target system was designed for this method [4].

During system design and load testing, the following aspects must be considered [8]:

- the measurement method must be independent of the software, which is executed by the embedded processor;
- the implementation of the measurement method must not modify the hardware architecture of the microprocessor;
- the measurement must provide real-time data, i.e. must detect changes in the system (processor) instantaneously.

Based on the above criteria, one can conclude that the measurement of the processor's computational load must be independent of the embedded system hardware and should not influence in any sense the system under test.

2.2. The execution of the interrupt process

As mentioned, the von Neumann computer model works well when the microprocessor performs only one task. Unfortunately, in embedded systems, the processor must perform several tasks at the same time. This is possible only if the processor divides its time between the tasks. This is only possible either using interrupt management or using an operating system, which allows task scheduling [9].

Interrupt Servicing (executed by Interrupt Service Routine – ISR) appears as an additional task next to the main program. The processor must perform this task also [10].

The processor cannot immediately execute the ISR, since there is a latency in the interrupt acceptance, which elapses between the interrupt

request and the start of the interrupt service. There are several reasons for this delay:

- the processor executes critical code segment, which means the interrupt request is disabled;
- the processor executes a task, which has higher priority;
- the processor executes a long instruction that cannot be interrupted.

The time until the interrupt accept may also vary. One of the reasons for this is that the instruction pipeline must be emptied. Its duration depends on the type of instructions in the pipeline. The other reason is that after the ISR (interrupt handling program) start the interrupted program state (main or other ISR) environment (registers, return address, program status flags, etc) must be saved and at the end of the ISR service routine this information must be restored. The time needed for saving the interrupted program environment depends on how many registers the ISR uses. The time delay until the interrupt accept therefore is not constant and can fluctuate.

When a processor receives an interrupt signal, and if the interrupt is enabled, the processor suspends the running process and begins handling the exception. After the execution of the interrupt handling routine (ISR), the processor returns to the suspended task.

In the case of ARM processors, the ISR should be treated as an exception as described in the ARM documentations [11]. This process of handling the exception is briefly explained below:

- If an ISR event occurs and exception handling is enabled, the processor suspends the currently executed instruction (and/or discards the so-called long instructions and restarts their execution after returning from ISR),
- Then the context registers (8 registers each 32 bits) are saved in the stack memory specified by the stack pointer (for ARM MSP - Main Stack Pointer or PSP - Process Stack Pointer). The saved registers are as follows: xPSR (Program Status Register), PC (Program Counter - contains the return address), LR (Link Register R14) and registers R12, R3, R2, R1, R0 are also saved.
- After that, the processor switches to handler operation mode.
- Then the program counter (PC) is loaded with the ISR start address and the LR loads the return address.
- In the next step, the ISR number is loaded into the IPSR (Interrupt Program Status Register).

–Finally, the execution of the interrupt handling routine begins.

The process described above consumes processor time. It is important to consider the time elapsed between the ISR request and the start of exception handling. If the interrupt is repeated cyclically, the response time of the ISR increases with the latency of the start of the interrupt handling. Critical external events can delay the start of the interrupt service routine from the point of view of the service time of the interrupt handling.

How much time is required to save registers ("overhead") and to execute program PUSH/POP instructions in order to save other registers? In such cases, the processor deals with the save/restore address of the register (stack operations). If the address contained by stack registers point to external memory, this "overhead time" will be longer (executing external memory operations).

The maximum repetition frequency of interrupts can be calculated for a given processor considering the given clock signal frequency:

$$F_{MaxInt} = F_{CPU} / (C_{ISR} + C_{Overhead}), \quad (1)$$

where F_{MaxInt} is the maximum repetition frequency of the interrupt – i.e. ISR, F_{CPU} is the frequency of the system clock, C_{ISR} is the number of clock cycles required to execute the interrupt handling routine (ISR), and $C_{Overhead}$ is the number of clock cycles used to save and restore the registers (i.e. to save the program state and restore).

By fulfilling a frequent interrupt request, the processor executes the ISR. Therefore, it spends less time on executing the main program. The time required to complete the ISR (U_i) is:

$$U_i = (F_i (C_{ISR} + C_{Overhead})) / F_{CPU}, \quad (2)$$

where F_i is the frequency of interrupts.

From the above, it results that the main program is apparently executed with a much lower clock frequency:

$$F_{main} = (1 - U_i) * F_{CPU}, \quad (3)$$

where F_{main} is the apparent frequency of main program execution.

3. Processor computation load measurement

During processor operation one can distinguish two states: when the processor runs the programs i.e. executes instructions – this is called the loaded state; while states are possible when the pro-

cessor is not active -- this is called an unloaded state. In the unloaded state, we distinguish:

- the sleep mode -- the processor does not execute instructions and it appears as if it is switched off - the dissipated power of the processor is very small;
- the idle state -- the processor waits for some event while executing instructions.

In the active state of the processor -- depending on the software activity -- different parts of the system are more active than other parts of the processor, for example, the arithmetic unit -- when it performs mathematical computations, shows high activity, or the memory manager unit also shows high activity when performing I/O operations. Based on this, the following processor operational categories are distinguished:

- base (unloaded state),
- calculation intensive,
- input - output operations.

This kind of classification was achieved by measuring the actual load of different parts of the processor. Using the measurements, one can identify the intensively used processor parts.

3.1. Processor load measurement method

The measurement method is supported by the internal structure of the used processor (Figure 1). Generally speaking, the processor is a state machine in which the storage elements (in the figure: Registers) store the current state of the system. The current state (q) changes at the rate of the clock signal. The value of the new state is generated by the so-called excitation network (in the figure FN1, FN2, etc.) as a function of the current state and possible external signals (v). The values of v , G , q are functions of time t (in this case, the clock signal controls the state changes). The

stored values become the excitation value after a clock delay [8], therefore:

$$q(t) = G(t - 1) \tag{4}$$

External signals influence the values of the G function, so it is not necessary to test them directly. The G values are transferred to the q (next state) values after a clock delay, so the measurement can be performed either by examining the G or q signals.

The operation of individual parts of the CPU is indicated by the change in the value of their associated memory. So, the measurable characteristic of the q signals relevant to the investigation is the change in frequency of the q signals, that is, the frequency of the signal. However, the classification is not based on the instantaneous values of the signal frequencies, but on the time change of the frequency, the time function of the frequency: $f\dot{r}(t)$.

3.2. Presentation of the System under test

The application on which the processor load measurement method was performed is an embedded system implemented on FPGA that controls a device that follows the movement of the Sun.

The application is a solar panel system that always sets the optimal operation depending on the movement of the Sun, i.e. it shows the maximum surface towards the Sun, which is perpendicular to the sun's rays (Figure 2).

The control system calculates the momentary orientation of the sun's rays (horizontal and north angle) as a function of time and geographical coordinates. Based on the calculated coordinates, it adjusts the solar panel so that it is perpendicular to the sun's rays, i.e. it moves the panel by con-

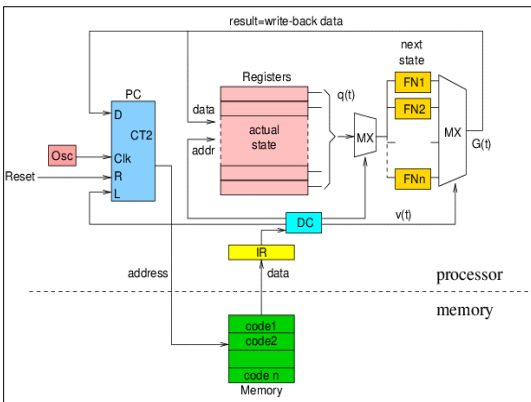


Fig. 1. Block diagram representing processor structure.



Fig. 2. The equipment controlled by the test application

trolling the activator motors. During the movement (adjustment of panels) depending on the computed result, the software performs a lot of I/O operations, similarly when the program updates the display of the user interface.

3.3. Measurement results

The measurement results are presented based on article [8].

The system was modelled with an embedded system implemented on FPGA, using RTL-based ARM M0+ processor.

During the tests, the system model was run using a hardware simulator, which saves the signal values appearing at the outputs and inputs of the system elements in a so-called "dump" file. The "dump" file containing the output results was analysed with an appropriate software.

The frequency signal $fr(t)$ variation in time is produced by a dedicated software that processes the output file of the simulation results. The algorithm built into the processing software corresponds to the operation of the digital circuit used for frequency measurement. During the hardware simulation, a large amount of data was generated. So a filter algorithm was incorporated into the processing software, which removed the data that was not relevant to the test. Due to the way the model was described, a lot of redundant information was obtained by having several signals duplicated by some other signals, so their values were identical. By removing this redundant information, the amount of data to be processed can be reduced.

With the graphic representation of the results, one can deduce which signal frequency changes show significant difference for some signals, at the time when the application software changes the processor state (load), i.e. when the compu-

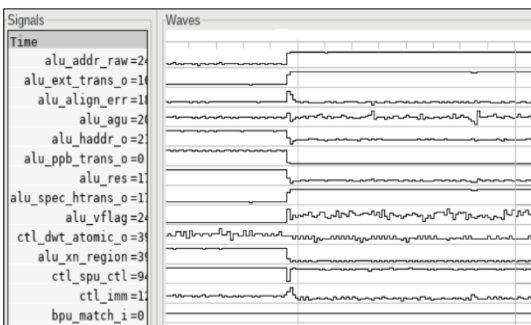


Fig. 3. Graphical representation of several measured signals.

tation algorithm starts or stops. Figure 3 shows the variation of some measured signals at the moment of starting the computation part of the application program.

Examining the signal correlation change shown in Figure 3, for example, in the case of the *alu_ext_trans_o* signal, one can notice that this signal shows a significant amplitude change, which means that the processor starts the computation, so its load increased.

Based on the modelling and simulation results, one can select the signals suitable for computation load measurement of the central unit. For the model, it is known when the application software performs a computation that will result in a load on the CPU. By examining the statistical characteristics of the $fr(t)$ functions, one can select which signals shows a higher degree of correlation with the processor behaviours to be detected. Figure 4 shows the distribution of the correlation of the examined processor signals with the computation mode variation. One can conclude that some signals correlate well with the operating mode, so they can be suitable for indicating computation load periods.

From the number of signals for the measurement, the ones whose change can be detected most easily by the measurement module should be selected.

After modifying the structure of the embedded system, the selected signals of the processor were connected to the measurement module. These signals were analysed using the measuring system. After measuring the frequency variation and amplitude change of the signals using the monitoring module one can measure the system evolution.

The computation load of the processor can be deduced from the amplitude changes of the selected signals.

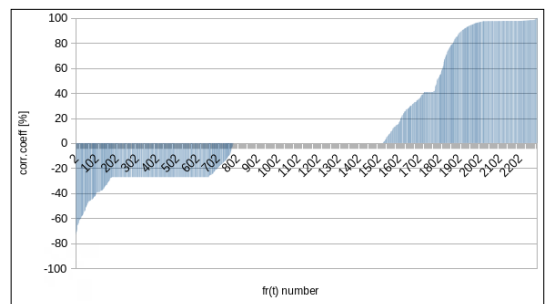


Fig. 4. Correlation values of signals to CPU load.

4. New method for interrupt process execution speed-up

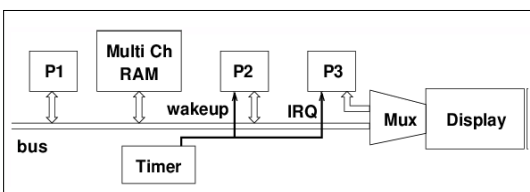
The block diagram of the experimental system is presented in **Figure 5**. In the experiment, for implementation, ARM RTL soft-core (ARM M0 processors) were used.

The experiment is as follows: a timer generated an interrupt signal at a given frequency (10 KHz). The exception handling program counted the number of interrupts, i.e. increases in the value of a counter (software clock). The main program displayed the value of the counter on a display.

The P3 processor works in a traditional way. It executes the main program and handles the interrupt, i.e. executes a timed task, and then sends the value of the counter to the display. The execution time of the interrupt and exception acceptance latency of the traditional solution running on the P3 processor are compared with a system executing the task in parallel (P1 and P2). Processor P1 runs the main program, while processor P2 performs interrupt handling. When the exception handling is done, the P2 processor goes in to a suspended state (sleep mode).

When an interrupt signal occurs, the P2 processor wakes up and executes the exception handling program. The operation of this processor has been designed in such a way as to avoid the interrupt accept latency that arises during the execution of the usual interrupt handling process. So, in this way, there is no time variation. The time required to start the service is constant.

Therefore, the timer peripheral signal was not connected to the interrupt request input of the ISR signal of P2. The processor is in suspended state (sleep mode). The peripheral signal generated by the timer is connected to the wake-up input of the processor. When the signal starts the processor, ISR is served, which this time is listed as the main program of P2. Since the wake-up occurs on the rising edge of the ISR, servicing of the "ISR" starts immediately. There is no need for an interrupt acceptance process. There is no need to save the state of the



5. ábra. Megszakításkezelés párhuzamosításának tömbvázlata

main program because the ISR is the main program of the processor P2. Therefore $C_{\text{Overhead}} = 0$ in equations (1) and (2).

At the end of the "ISR" service, the program jumps back to the beginning of the program, where an instruction suspends the processor P2. In sleep mode, it then waits for the next ISR signal. The peripheral interrupt signal is stored by the processor interrupt handling circuit until the service starts.

Figure 6 shows the result of the simulation of the parallel solution in comparison with the conventional solution. The event signal indicates the interrupt request of the peripheral; this pulse comes from the timer peripheral with a frequency of 10 kHz.

The *Wake Up* signal wakes up the P2 processor. The *No sleep* signal is generated by the processor and indicates that it continues program execution. This signal deletes the external storage. The *Service Start* signal is generated by the first "ISR service" instruction of the P2 processor, indicating that the service has started.

The *Event* signal interrupts the P3 processor program in the traditional way. The first instruction of the ISR function of the P3 processor generates the *ISR_Start* signal. This indicator signal was used to compare the starting point of the two ISRs, one executed on P2 and one executed on P3. Due to the exception handling process (saving registers, as mentioned previously, etc.), the P3 processor starts the ISR process later than the P2 processor.

5. Fuzzy Interpolation

A robot moving in a real environment must make decisions in different situations and react appropriately to each situation. In the case of behaviour-based control, the behaviours specified by the expert system are valid for given situations. The robot recognizes situations based on the data provided by its sensors and its internal states. Each defining condition has a behaviour that the robot performs [12], [13] and [14].

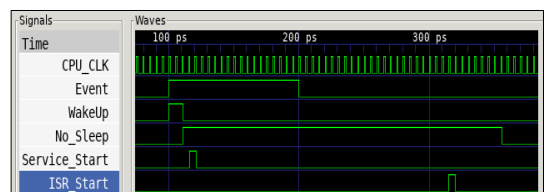


Fig. 6. Simulation results of the interrupt handling.

In the case where behaviour models are implemented with fuzzy logic, thanks to the fuzzy state machine, all possible behaviours are involved in the control system of the robot. Those behaviours that best fit the given set of observations will have the greatest impact on the robot's movements and its reactions [12–14].

Since robot movements are performed in a real environment, this can have different kinds of effects on the control decisions, it may happen that a set of observations does not relate to the robot's behaviour. In this case, the robot control system may become unable to take a decision. This can be improved by adding more fuzzy rules. But the increasing number of rules will result in the increased use of computing resources. Fuzzy rule interpolation provides a solution for this case [12–14].

Thanks to the interpolation procedure, it is enough to give to the expert system the most decisive rules, and in intermediate cases the interpolation procedure will provide the output control values [12–14].

Using the expert knowledge base, the system behaves almost correctly even when there is no rule of behaviour for the given situation. The fuzzy state machine uses the FIVE (Fuzzy Interpolation in Vague Environment) fuzzy interpolation procedure [12–14].

One application example of behaviour-based control is etorobotics, where the robot imitates the behaviour of an animal.

5.1. Fuzzy Interpolation in Vague Environment

The control system decision-making process of autonomous robots is carried out based on information from multiple sensors and the internal states. These input data form the observations of the fuzzy rules, and are also known as antecedents, while the outputs of the fuzzy rules are called *consequents*. A fuzzy rule can be written in the form of an implication of the form "IF ... THEN ... (ELSE)...". The set of fuzzy rules affecting the same output is called a *fuzzy rule base* [13][15] and [16].

In classic fuzzy systems, for the sake of stability, the rules must be designed in such a way that there exists a rule for every possible input combination. This ensures that the rules completely cover the state space. However, as the size of the task to be solved increases, the number of rules can grow exponentially, which results in a significant computational demand. Furthermore, gen-

erating a large number of rules is often problematic, as expert systems cannot always fully cover the problem due to mathematical complexity or lack of information. As a result, instead of a fully covering rule system, the control often works with a sparse rule base, in which some observations may not have a rule, so the output of the system will be uncertain [13], [15] and [16].

Sparse rule sets are more common than full coverage rule sets. Fuzzy interpolation methods offer a solution to the problem of sparse rule systems. These methods calculate the decisions belonging to the missing rules based on the existing rules. As a result of this method, it is sufficient for the expert system to enter only the most important rules. Thus, reducing the number of rules and the complexity of the system, as well as the interpolation depending on the method, will result also in the reduction of the computation requirement need [13], [15] and [16].

The Fuzzy Interpolation in a Vague Environment (FIVE) method places the rules in a vague space, where the Euclidean distance between the rules can be interpreted. They can be distinguished from each other based on the distance between the rules: a larger distance means a greater difference, while a smaller distance means more similar rules [13], [15] and [16].

Using the consequents weighted by the rule distance, Shepard interpolation calculates using inverse distances to create the decision of the rule base. The calculation steps of the FIVE methods are described below (see Figure 7):

- *Observation* is the information from the environment or internal state.
- With the help of *Linear Interpolation*, it assigns to the observation the value that specifies the extent to which the observation's value (μ) is a member of the given fuzzy set.
- The difference between the antecedent belonging to the rule and the μ value of the observation give the *Antecedent Distance*.
- The *Rule Distance* is the Euclidean distance of the antecedent distances.
- The *Shepard Interpolation* uses the distances of the rule to produce the Decision, i.e. is the consequent.

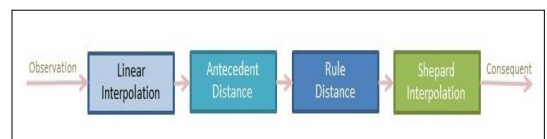


Fig. 7. Computation steps of FIVE accelerator.

5.2. FIVE hardware implementation

The most important requirement for the hardware implementation is tunability and parameterization during on-line operation. This means that one can modify the parameters of the FIVE controllers, including the antecedent and consequent values, while the system is operating.

To this end, parameters are stored in registers, for which an interface has been designed to allow the internal data of each module to be changed during a clock cycle.

The controller can be easily connected and adapted via variable bit width interface (output and input buses). This bus system also enables compatibility with the AXI interface, which is particularly useful for integrating FIVE hardware into a processor system.

The scalable resolution was realized with a modular structure and parameterizable bit width. The number of individual modules can be changed according to the amount required by the rules, so it flexibly adapts to the requirements of the system.

An important aspect is the portability of the code between FPGA platforms, so no manufacturer-specific elements were used in the code written in Verilog. This ensures that the code can be used on different platforms.

The circuit can be generated from FBDL (Fuzzy Behaviour Description Language) [17]. The connection and parameters of the modules can be obtained from the rule bases described in the FBDL language, which simplifies the planning and implementation of the system.

The FIVE method can produce results through four computation steps, which consist of two interpolation calculations and two distance calculations.

The processing of the data stream is illustrated in Figure 7 which contains the calculation steps of a rule base. The figure shows that, except for the Shepard interpolation module, the number of individual modules depends on the number of rules, antecedents and observations found in the rule base.

The number of linear interpolations is determined by the number of observations, while the number of antecedent distance calculations depends on the number of antecedents of each rule. Each rule has a rule distance calculation module, and the Shepard interpolation is calculated with a single module per rule base.

The calculation of linear interpolation is called "Universe" in the final implementation. In addition,

also the hardware implementation was prepared with the Vivado High Level Synthesis tool, using unmodified and optimized versions of the basic μ FRI library [18].

The FIVE FPGA implementation forms a synchronous computing chain. Each unit of the circuit produces the output value in response to changes in the input data. The implemented hardware works with variable bit width, by default the implementation was done with 8-bit unsigned integers for the input/output interfaces. The amount of data required for the computation can also be specified as a parameter.

The individual computation units and the inclusion unit also have constant and variable parts. The parts whose number varies based on the properties of the rules and rule bases (number of rules, number of observations, number of antecedents, etc.) were highlighted in the code and entered the Verilog code in a form that can be produced from the FBDL. The computing units ensure the pipeline operation for division and other operations. Each unit contains an internal input/output storage register, where the incoming data and the result are stored. According to the current design, all units produce results within one clock period, except for the Universe unit, which produces results in two steps.

5.3. Results

The implementation and simulation results of the system were produced with AMD Vivado version 2018.1.

The latency of the entire computation chain is 4 clock periods, as shown in Figure 8. The system can work with unsigned integers, and its maximum operating frequency is 4 MHz.

Figure 9 illustrates the operational linearity error of the FIVE pipeline accelerator. Based on the simulation, the largest absolute deviation from the expected value is 6, which corresponds to 2.34 % in the 8-bit range.

For the FIVE method implementation on FPGA, a frame made in Verilog hardware description language has been prepared, which is suitable for speeding up the computation of the FIVE method.



Fig. 8. FIVE accelerator delay.

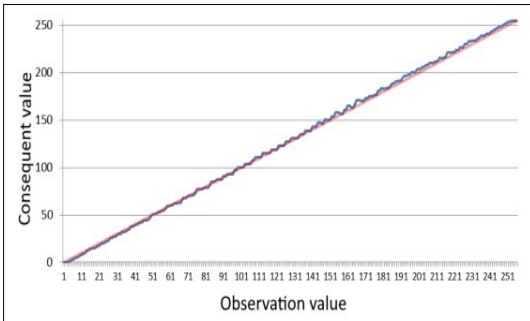


Fig. 9. FIVE accelerator error.

od as a hardware element that can be generated based on FBDL (Fuzzy Behavior Description Language). This module can be used independently or in association with an embedded processor system as an acceleration co-processing element. Complex behaviour of FIVE can be implemented by connecting several FRI_FIVE modules.

The FIVE IP structure also enables its implementation on Xilinx Adaptive Platform as a hardware acceleration unit operating in a software environment. In this case, the computing units are either connected to the processor system via the entire FIVE IP AXI interface. In this case the software component of the controller implementation module manages data collection and control tasks. A detailed description of the system is contained in article [19].

References

- [1] J. Neumann., *First Draft of a Report on the EDVAC*. Moore School of Electrical Engineering, University of Pennsylvania, 1945.
- [2] W Aspray: *John von Neumann and the Origins of Modern Computing*. MIT Press, Cambridge, 1990, p. 34-48.
- [3] Drótos D., Vásárhelyi J.: *Interrupt Driven Parallel Processing*. In: 20th International Carpathian Control Conference (ICCC), Krakow-Wieliczka, Poland, 2019, 1–4.
<https://doi.org/10.1109/CarpathianCC.2019.8765909>
- [4] G. Zhao, S. Hassan, Y. Zou, D. Truong, T. Corbin: *Predicting Performance Anomalies in Software Systems at Run-Time*. ACM Transactions. Software Engineering. Methodology. 30/3. Article 33 (July 2021).
<https://doi.org/10.1145/3440757>
- [5] H. Sayadi, N. Patel, S. Manoj P.D., A. Sasan, S. Rafatirad, H. Homayoun: *Ensemble Learning for Effective Run-Time Hardware-Based Mal Ware Detection: A Comprehensive Analysis and Classification*, 55th ACM/ESDA/IEEE Design Automation Conference (DAC), 2018, pp. 1-6,
<https://doi.org/10.1109/DAC.2018.8465828>
- [6] J. Muskens, M. Chaudron: *Prediction of Run-Time Resource Consumption in Multi-Task Component-Based Software Systems*. In: Crnkovic I., Stafford J.A., Schmidt H.W., Wallnau K. (eds) *Component-Based Software Engineering*. CBSE 2004. Lecture Notes in Computer Science, vol. 3054. Springer, Berlin, Heidelberg 2004.
https://doi.org/10.1007/978-3-540-24774-6_16
- [7] B. H. Fletcher: *FPGA Embedded Processors*. In: *Embedded Training Program Embedded Systems Conference San Francisco 2005 ETP-367*, 2005, 37.
- [8] D. Drótos, J. Vásárhelyi: *Microprocessor Load Measurement in an Embedded System*. 24th International Carpathian Control Conference (ICCC), Miskolc–Szilvásvárad, Hungary, 2023. 110–113.
<https://doi.org/10.1109/ICCC57093.2023.10178929>
- [9] G. M. Amdahl, *Validity of the Single Processor Approach to Achieving Large-Scale Computing Capabilities*. In: AFIPS Conference, Proceedings, Vol. 30. 483–485.
<https://doi.org/10.1145/1465482.1465560>
- [10] U. Vishkin: *Is Multicore Hardware for General-Purpose Parallel Processing Broken?* Comm. ACM, 57, p. 35 (2014) *The Future of Computing Performance: Game Over or Next Level?*, <https://www.nap.edu/read/12980/chapter/1>, 31/08/2017. utoljára látogatott: 2024. 06. 06.
- [11] A. N. Sloss, D. Symess, C. Wright: *ARM System Developer's Guide Designing and Optimizing System Software*. Elsevier, Morgan Kaufmann Publishers, ISBN: 1-55860-874-5, 2004, 702.
- [12] Kovács S., Kóczy L.: *Application of the Approximate Fuzzy Reasoning Based on Interpolation in the Vague Environment of the Fuzzy Rulebase in the Fuzzy Logic Controlled Path Tracking Strategy of Differential Steered AGVs*. In: International Conference on Computational Intelligence, 1997. 456–467.
- [13] Kovács S.: *Extending the Fuzzy Rule Interpolation FIVE by Fuzzy Observation*. In: *Computational Intelligence, Theory and Applications*, Springer, 2006. 485–497.
- [14] S. Kovács, M. Gácsi, D. Vincze, P. Korondi, Á. Miklósi: *A Novel, Ethologically Inspired HRI Model Implementation: Simulating Dog-Human Attachment*. In: 2nd International Conference on Cognitive Infocommunications, 2011. 1–4.
- [15] T. Tompa, S. Kovács: *Applying Expert Heuristic as an A Priori Knowledge for FRIQ-Learning*. Acta Polytechnica Hungarica, 17. (2020) 27–45.
- [16] T. Tompa, S. Kovács, D. Vincze, Mihoko Niitsuma: *Demonstration of Expert Knowledge Injection in Fuzzy Rule Interpolation Based Q-Learning*. In: IEEE/SICE International Symposium on System Integration (SII), 2021. 843–844.
- [17] I. Piller, D. Vincze, S. Kovács: *Declarative Language for Behaviour Description*. In: *Emergent Trends in Robotics and Intelligent Systems*. Springer, 2015. 103–112.

- [18] R. Bartók, J. Vásárhelyi: *Two Methods for Autonomous Robot Obstacle Sensing and Application Programming Interface for Fuzzy Rule Interpolation*. 18th International Carpathian Control Conference (ICCC). IEEE, 2017.
- [19] R. Bartók, J. Vásárhelyi: *Design of a FPGA Accelerator for the FIVE Fuzzy Interpolation Method*. International Journal of Computer Applications in Technology, 68/4. (2022) 321–331.

SZERZŐK JEGYZÉKE
LIST OF AUTHORS

A

AHMAD BUHAI RI MINH ALINA BINTI 56
AICHA OUI NADA EL YASMINE 1

B

BALAJTI ISTVÁN 21
BATÓK ROLAND 97
BITAY ENIKŐ 7
BOGYOR ANDREA 7

C–D

CSAVDÁRI ALEXANDRA ANA 7
DEZSŐ GERGELY 16, 89
DIÓS SZABOLCS SÁNDOR 21
DINYA TAMÁS 21
DRÓTOS DÁNIEL 97

E–F

EGYED-FALUVÉGI ERZSÉBET 84
FERENCZ JÁNOS 36

G–I

GÁTI JÓZSEF 31, 61
GERGELY ATTILA 80
GOBESZ F.-ZSONGOR 67
IMECS MÁRIA 36

K

KELEMEN ANDRÁS 36
KOVÁCS TÜNDE ANNA 1, 56, 61
KUTI JÁNOS 31

M

MASUK ABDULLAH 21
MÁTÉ MÁRTON 48

N

NAGY BALÁZS ÁKOS 61
NAGY ÖRS 67
NÉMETH BÍBORKA 73
NÉMETHY KRISZTINA 31

P

PETTENDI DÁVID 21
PINKE PÉTER 56
PORTIK SZILVESZTER 80

R

RAPPERT BALÁZS 84
REZES GÁBOR 89
RUBINT PÉTER 97

S–SZ

SÁNDULY ANNABELLA 67
SZÁNTÓ ATTILA 21
SZIGETI FERENC 89
SZŐCS KRISZTINA 48

T–V

TÓTH LÁSZLÓ 56
VÁSÁRHELYI JÓZSEF 97

